Study of the dynamics of biomolecules by high speed atomic force microscopy and surface enhanced Raman spectroscopy

Ece Neslihan Aybeke

Université de Bourgogne Franche – Comté
Faculté des Sciences

Laboratoire Interdisciplinaire Carnot de Bourgogne UMR CNRS 6303
Département Nanosciences

Study of the Dynamics of Biomolecules by High Speed Atomic Force Microscopy and Surface Enhanced Raman Spectroscopy

Thèse présentée à l'Université de Bourgogne Franche – Comté
pour obtenir le grade de Docteur (Mention Physique)

par

Ece Neslihan AYBEKE

Soutenue le 8 Juillet 2015 devant la commission d'examen composée de:

BIJEON J.-L.	Professeur, Univ. Technologique de Troyes	Rapporteur
MILHIET P.-E.	Directeur de Recherche, Univ. de Montpellier I	Rapporteur
BOIREAU W.	Chargé de Recherche, Univ. de Franche-Comté	Examinateur
DAZZI A.	Professeur, Univ. Paris Sud	Examinateur
BOURILLOT E.	Maitre de conférences, Univ. de Bourgogne	Codirecteur
LESNIEWSKA E.	Professeur, Univ. de Bourgogne	Directeur de thèse

Abstract

This thesis focuses on the coupling of High–Speed Atomic Force Microscopy (HS-AFM) and Surface Enhanced Raman Spectroscopy (SERS) for biomolecule analysis. We have designed a fabrication protocol to manufacture "SERS-active" substrates. The efficacy of gold, silver and gold-silver bimetallic crystalline nanoparticle substrates were evaluated. We have investigated the impact of optical and morphological features of the substrates on Raman signal intensity by analyzing well-known samples such as bipyridine ethylene and methylene blue molecules. We took an interest in three distinct biological problematics with HS-AFM and SERS analyses. First, we have detected the chemical signature of cytochrome b5 protein. This study was followed by the investigation of conformational changes of small heat shock leuconostoc oenos Lo 18 protein in function of pH level and concentrations. The last application consists to the analyse a membrane and a virus interaction. In order to realize simultaneous Raman/AFM analysis, we have adapted our fabrication protocol to cover the surface of commercial AFM probes by crystalline gold nanoparticles. Tip – Enhanced Raman Spectroscopy (TERS) studies were performed on molybdenum disulfide to evaluate the quality of TERS probes. In the last part of this work, we have designed a new setup to combine Ando's HS-AFM setup with Raman spectroscopy. We present the modifications that have been carried out and the challenges that we have encountered.

Key words: High–Speed Atomic Force Microscopy (HS-AFM), Surface Enhanced Raman Spectroscopy (SERS), Tip–Enhanced Raman Spectroscopy (TERS), Nanoparticle substrates, Localized Surface Plasmons (LSP), cells, proteins, Detergent resistant membrane domains (DRMs), Noroviruses (NoVs).

Resumé

Ce travail de thèse se focalise sur le couplage du microscope à force atomique haute–vitesse (HS-AFM) et de la spectroscopie Raman exaltée de surface (SERS) pour la détection des biomolécules. Nous avons élaboré un protocole de fabrication pour produire les substrats "SERS-actifs". L'efficacité des substrats de nanoparticules cristalline d'or, d'argent ou bimétallique argent–or a été évaluée. Nous avons étudié l'impact des propriétés optiques et morphologiques des substrats sur l'intensité Raman en analysant des échantillons tests tels que la bipyridine éthylène et le bleu de méthylène. Nous nous sommes interessés à trois problematiques biologiques distinctes par analyses HS-AFM et SERS. Dans un premier cas, nous avons détecté la signature chimique de protéine cytochrome b5. Ce travail a été suivi par des études sur le changement de conformation de la protéine de choc thermique leuconostoc oenos Lo 18 en fonction de la concentration et du pH. La dernière application consiste en l'analyse des interactions membrane – virus. Afin de réaliser les analyses simultanées Raman/AFM, nous avons adapté notre protocole de fabrication pour couvrir la surface des pointes AFM commerciales par des nanoparticules d'or cristallines. Les études de diffusion Raman exaltée par effet de pointe (TERS) ont été effectuées sur les échantillons de disulfure de molybdène pour évaluer la qualité des pointes TERS. Pour finir, nous présentons une nouvelle configuration de couplage HS-AFM et spectroscopie Raman. Nous discutons des modifications et des défis rencontrés.

Mots clés: Microscopie à force atomique haute-vitesse (HS-AFM), spectroscopie Raman exaltée de surface (SERS), diffusion Raman exaltée par effet de pointe (TERS), Substrats de nanoparticules, Plasmons de Surface Localisé (LSP), cellules, protéines, détergent résistant membrane domaines (DRMs), Noroviruses (NoVs).

Remerciements

Le travail de thèse exposé dans ce manuscrit a été réalisé au sein de l'équipe Optique Submicronique – OSNC de l'Institut Carnot de Bourgogne - ICB (UMR CNRS 6303). Je remercie ainsi le Professeur Alain Dereux pour m'avoir accueilli au sein de l'équipe et du laboratoire il y a trois ans.

Par la présente, je tiens à remercier sincèrement mes directeurs de thèse, Monsieur Eric Lesniewska, Professeur à l'Université de Bourgogne Franche – Comté et Monsieur Eric Bourillot, Maître de Conférence à l'Université de Bourgogne Franche – Comté. Je tiens donc à exprimer ma reconnaissance à mes directeurs de thèse car ils n'ont jamais hésité à se rendre disponible tout au long de ces trois ans. La liberté qu'ils m'ont accordé ainsi que leur confiance en mes capacités et leur enseignement très précieux, m'ont permis de consolider mes connaissances et d'atteindre mes objectifs. Durant cette thèse, j'ai apprécié toutes nos discussions scientifiques et personnelles. Je suis très reconnaissante de leurs qualités humaines.

J'exprime ma gratitude à Monsieur Jean-Louis Bijeon, Professeur à l'Institut Charles Delaunay (UMR CNRS 6281) de l'université de Technologie de Troyes et Monsieur Pierre-Emmanuel Milhiet, Directeur de Recherche au Centre de Biochimie Structurale (UMR CNRS 5048, Inserm U 1054) à l'Université de Montpellier, d'avoir accepté de rapporter mon travail de thèse.

Je remercie Monsieur Alexandre Dazzi, Professeur au Laboratoire de Chimie Physique (UMR CNRS 8000) à l'Université Paris-Sud et Monsieur Wilfrid Boireau, Chargé de Recherche à l'Institut Femto-ST (UMR CNRS 6174) de l'université de Besançon pour avoir accepté d'être membres du jury et examinateurs de ce travail.

J'aimerais remercier les différents chercheurs que nous avons collaboré durant ce travail de thèse en particulière Dr. Gaël Belliot du Centre National de Référence des virus entériques (INSERM U866), CHU de Dijon, Dr. Celine Ellie-Caille du l'Institut Femto-ST (UMR CNRS 6174) de l'université de Besançon, Pr. Jean Guzzo de l'Institut Jules Guyot (UMR PAM, AgroSup Dijon) et Dr. L. Tetard de NanoScience Technology Center (Université de Colorado) qui

nous ont fourni les échantillons étudié dans le cadre de cette thèse ainsi pour leur partage d'informations précieuses.

Mes sincères remerciements vont également à Yvon Lacroute pour la fabrication des substrats de nanoparticules, tous ses partages de son savoir-faire sur la fabrication des nanostructures fabuleuses, ses supports pour le MEB et bien sûr pour nos tours de vélo. Je n'oublie pas Alexandre Bouhelier, mes sincères remerciements pour la maîtrise du Raman ainsi que pour les questions et remarques qui m'ont stressée pour l'instant mais elles ont été pertinente pour avancer dans mes recherches.

Je tiens également à remercier chaleureusement à Elly Lacroute pour sa gentillesse, sa disponibilité tant sur le plan personnel que professionnel et aussi ses aides administratives.

Mes remerciements s'adressent aussi à David Carriou, Maxime Ewald et Maggie Baranowska, pour les aides que vous m'avez fourni au début de ma thèse. Je souhaite à vous tous une bonne continuation.

Je remercie également mes collègues de bureau : Delphine Sicard, Cédric Thomas et Svetlana Pleskova. J'ai partagé des bons moments et des conversations intéressantes avec vous. Cédric, je te souhaite bonne continuation pour ta thèse. Et, Svetlana mes remerciements spéciaux pour toi, pour la réponse à toutes mes questions concernant la biologie ainsi que pour ton amitié.

Pauline Vitry, je ne t'oublie pas. Je te remercie pour tes attentions quotidiennes et les sorties que tu nous as organisées. Je te souhaite bon courage pour la dernière année de ta thèse. Des remerciements pour Filimon et Simon, ainsi pour leur présence à la vie quotidienne du labo et pour leur amitié.

Également, je remercie toutes les autres personnes présentes au laboratoire. Grâce à leur collaboration et aussi à leur gentillesse, j'ai découvert la diversité des responsabilités requises pour ce métier. Merci à Thomas, Serkan, Karim, Stéphane, Rémi, Hélène, Jean, Thibault, Nicolas, Raphael, Marie, Brice, Christophe, Kamal, Michael, Mingxia, Jean-Emmanuel, Mickaël, Antonin, Floriane, Christian.

Mes sincères remerciements s'adressent aussi à Bertrand Glosset, merci encore pour toutes tes aides pour la Français aussi que tout le courage que tu m'apporté

depuis le début de mon séjour en France.

Je remercie sincèrement aussi à mes amis pour ceux que j'ai rencontrés en dehors du laboratoire durant ces trois années dijonnaises. Merci à Yianna, Nina, Pierre-Antoine, Maria et George, pour votre présence, amitié et soutiens. Un merci spécial à George pour nos pauses de déjeuner gastronomique (!) et ses supports informatiques y compris LaTeX!

Pour finir, je remercie de tout mon cœur à mon famille pour leur présence et leurs soutiens! Vous avez toujours cru en moi, m'avez fait confiance et m'avez donné du courage pour suivre mes projets loin de la maison familiale...

A tous, Merci.

Abbreviations

AFM	Atomic Force Microscopy
HS-AFM	High Speed Atomic Force Microscopy
SERS	Surface Enhanced Raman Spectroscopy
TERS	Tip Enhanced Raman Spectroscopy
SP	Surface Plasmons
LSP	Localized Surface Plasmons
LSPR	Localized Surface Plasmon Resonance
SEM	Scanning Electron Microscopy
XRD	X-Ray Diffraction
RT-PCR	Real Time Polymerase Chain Reaction
CCD	Charge Coupled Detector
NPs	Nanoparticles
EBL	Electron Beam Lithography
EBD tips	Electron Beam Deposited tips
NSL	Real Nanosphere Lithography
MB	Methylene Blue
BPE	Bioyridine Ethylene
Cyt b5	Cytochrome b5
DTT	Dithiothreitol
sHsp Lo 18	Small Heat Shock Protein Leuconostoc oenos
DRM	Detergent Resistant Membrane domain
ATP	Adenosibe Triphosphate
NoV	Human Norovirus
MNV	Murine Norovirus
RAW	Mouse leukaemic monocyte macrophage cells
MβCD	Methyl-beta-cyclodextrin
Caco–2	Human colon carcinoma cells
$NaIO_4$	Sodium periodate
$CuSO_4$	Cholera toxin
VLP	Virus Like Particle
MoS_2	Molybdenum disulfide

Contents

General Introduction

The material characterization is a fast-growing field that helps to material syntheses in industry, diagnosis of diseases in medicine, production of devices in electronics & technology and researches in biology and physics. Today under favor of recent developments in nanotechnology, we can find a large number of devices that provide the surface or deep-profiling analysis by detecting mechanical, electrical, chemical or optical properties of samples. These devices are mainly based on detecting single type of data: chemical, electrical, optic and mechanic. Thus combining different techniques aids to reach deeper knowledge about the sample.

This thesis focus on the analysis of biomolecules by High-Speed Atomic Force Microscopy and Surface Enhanced Raman Spectroscopy. High-Speed Atomic Force Microscopy provides to analyze conductive or dielectric samples with a high temporal and lateral resolution in liquid medium. The dynamics of biomolecules including that their trajectory and velocity can be achieved. This microscope is a prototype based on the developments performed by Prof. Ando's team at Kanazawa Biophysics Lab. (University of Kanazawa, Japon). In 2008, an international consortium program was constituted in order to promote the use and development of HS-AFM as well as to spread the related information. This international science community is participated by Pr. T. Ando (Kanazawa Biophysics Lab., University of Kanazawa), Dr. P. E. Milhiet (UMR5048 CNRS-U1054 INSERM, University of Montpellier), Dr. S. Scheuring (U1006 INSERM, University of Aix-Marseille), Prof. E. Lesniewska (UMR 6303, University of Burgundy Franche-Comte), Prof. P. Hinterdorfer (University of

Linz), Prof. Y. Lyubchenko (University of Nebraska Medical Center) and Bruker Corporation.

Our project in this thesis involves the design of a new version of High-Speed Atomic Force Microscopy (HS-AFM) which contains Surface Enhanced Raman Spectroscopy (SERS) technique and both analyses that can be operated simultaneously. SERS is a highly sensitive spectral analysis technique that allows the identification of materials components. The combining HS-AFM with SERS provides to study topographical and chemical properties of analytes. We have chosen these techniques by considering their compatibleness and complementariness as well as the experimental adaptability. More precisely, the acquisition times, the data types and the required experimental conditions of techniques are evaluated.

The very first chapter reviews the working mechanism of the related characterization techniques including their physical phenomena. We start from atomic force microscopy and move toward HS-AFM by discussing the motivations of the development and the improvements applied. At the second part of this chapter, we introduce firstly Raman spectroscopy and the signal enhancement via plasmons before address the general features of SERS.

The second chapter of the manuscript is dedicated to plasmonic active crystalline nanoparticle substrates. Fabrication of plasmonic substrates and the impact of their morphological features on the Raman signal exaltation are discussed. Following presentation of our protocol, we investigate the topographic features and homogeneity of the substrates, the mechanical stability and crystallinity of the constituted nanoparticles. Lastly, the performance of substrates on SERS experiments is evaluated by using two reference samples : bipyridine ethylene and methylene blue molecules.

In the third chapter, we focus on the applications of HS-AFM and SERS. Although, SERS is a very fruitful technique for analyzing reference samples and simple molecules, it remains difficulties for studying complex samples. Therefore, we have investigated firstly a human microsomal cytochrome b5 protein at non-resonant condition to test sensitivity of our substrates. Small heat shock

protein are well-known with its conformational changes under the stress conditions.

We analyzed small heat shock leuconostoc oenos protein in function of pH level and concentration by HS-AFM and SERS to observe the chemical and topographic variations arised from conformational changes. Lastly, we have investigated the interactions between a cell membrane and a virus to approach gastroenteritis disease by studying a model system constituted by mouse leukaemic monocyte machropage cells and murine noroviruses. This work is followed by the analysis on human intestinal cells.

In the last chapter, we present our results related to the coupling of atomic force microscopy with Raman spectroscopy. We have developed a specific protocol for producing crystalline nanoparticles on AFM probes. These probes are implemented to tip-enhanced Raman spectroscopy (TERS) experiments. This chapter also details the developments carried out on HS-AFM to combine it with Raman and Fluorencesce spectroscopies. The challenges that we have encountered and the limitations of the combined microscope have been discussed.

1

State of art

Cells are building blocks of living mechanisms that contain several complex structures. These living entities are highly dynamics and in interaction between each other. Cell membrane is the first border with its neighborhood and the gate between inside and outside of cell. Thus all interactions including injections, ejections and signalization take place in membrane. These biological events are on millisecond time scale that's why it is complicated to observe them in real-time. However, such analyses can help to understand different phenomena such as a virus infection, lipochaperon activity, cell protection, energy production, transportation and transformation, and so on. To preserve their natural mimics, morphology and dynamic, it is necessary to analyze them in their own physiological environment.

Today under favor of many developments in nanotechnology, it is possible to observe any sample at nanoscale size and follow its dynamics. High-speed atomic force microscopy (HS-AFM) enables to observe the dynamic behaviors of biomolecules. The successive images provide to investigate the instant topography of sample, the velocity and trajectory of entities. Surface enhanced Raman spectroscopy (SERS) is a complementary characterization tool to atomic force microscopy (AFM) by providing chemical information of sample. This chapter introduces the working mechanism of both techniques and involved physical phenomena.

1.1 From Atomic Force Microscopy to High-Speed Atomic Force Microscopy

Atomic force microscopy (AFM) is a powerful tool to characterize the topography of materials at atomic resolution. The precursor of atomic force microscopy was the scanning tunneling microscope (STM) [1]. This pioneering work led to the development of AFM [2] just four years after the invention of STM. STM and AFM are classified under scanning probe microscopy category as scanning near-field optical microscopy (SNOM), photon scanning tunneling microscopy (PSTM) and scanning capacitance microscopy (SCM). The common point of these microscopes is the scanning process of a surface by a probe and the detection of forces, tension, evanescence field, capacitance etc. depending on the type of microscope.

One of the important advantage of atomic force microscopy being able to analyze conductive and insulate samples. The analysis can be carry out in air, liquid medium, controlled atmosphere, vacuum and under high pressure. The first AFM study performed in liquid medium was using of paraffin oil to analyze the surface of sodium chloride crystal in 1987 [3]. This step at AFM history opened the gates to explore the morphology of different materials in their physiological environment. This work has opened large opportunities for AFM by making it possible to investigate an infinite number of samples in various liquid mediums for applications in the field of experimental physics, chemistry, materials science, biology and medicine. Accordingly, amino acid crystals [4], lipid membranes [5], biominerals and commercial materials [6] were studied in liquid medium by contact mode (the first invented mode). The invention of oscillating contact [7] provided an opportunity for scanning soft surfaces without causing tip induced damages. This improvement was applied quickly to analyze the DNA [8] and the membrane proteins [9].

In this section, we first introduce the principle of atomic force microscopy including the associated physical phenomena and the imaging modes. The basics of AFM will be followed by high speed atomic force microscopy by pointing out the motivations and the technical requirements.

1.1.1 Atomic Force Microscopy

1.1.1.1 Basic principles of AFM

Atomic force microscopy allows to visualize the topographic features of surfaces of nanometric to micrometric scale. A schematic presentation of AFM is given in Fig.1.1.

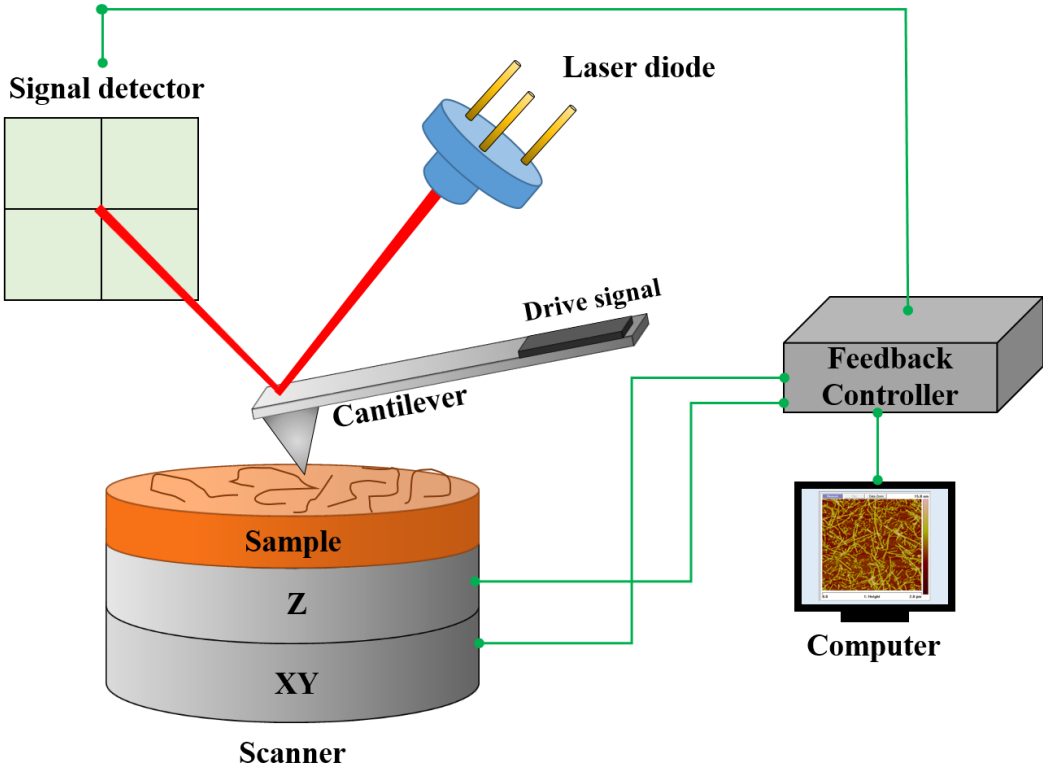

Fig. 1.1: Schematic drawing of atomic force microscope.

The working mechanism of an atomic force microscopy is based on detection of the inter-atomic forces between a sample and a probe. AFM probes consist of a flexible cantilever and a sharp tip at its extremity which scans the surface of analyte line by line (e.g. 512 for all results shown in the present document) to constitute the cartography of the sample. During the scanning, the cantilever deflects in function of the tip-sample interaction forces. The variation of the deflection is measured via an optical detection system which involves a laser diode and a photodetector.

A laser beam is focused at the extremity of cantilever and reflected through to the photodetector. The differences in lateral and vertical forces can be obtained by monitoring the displacement of laser spot on the 4-segmented photodetector. The forces between the sample and the tip is maintained constant during the whole operation via closed-loop feedback system. The magnitude of sample-tip interactions can be adjusted by the operator during the imaging process. The actual magnitude of the sample-tip interactions are corrected by Proportional-Integral-Differential (PID) feedback in order to minimize error signal and maintain to constant the sample-tip interactions. The sample is placed onto a piezo-electric ceramic called *scanner* that can provide to follow the movement of AFM tip at X, Y and Z directions. The deviation at laser spot is maintained constant for each scanning point in order to constitute 3D topographic image of the sample.

1.1.1.2 Forces

The tip-sample interactions during the AFM operation reveals different nature of forces. Here, we introduce the essential interactions in order of short to long range.

Van der Waals Forces

Van der Waals forces are raised from interactions between atoms, molecules and surfaces. Regardless the environment, they can be produced in ambient conditions, liquid or vacuum. Van der Waals forces are attractive and short-ranged ($1/r^6$, i.e. 2-3 nm), originated from the dipole - dipole interactions. Van der Waals energy is expressed by

$$E_{VdW} = -\frac{1}{r^6}\cdot[\underbrace{\frac{\mu_1^2\cdot\mu_2^2}{3\cdot(4\cdot\pi\cdot\varepsilon_0\cdot\varepsilon\cdot k_B\cdot T)}}_{\textbf{Keesom}}+\underbrace{\frac{\mu_1^2\cdot\alpha_2+\mu_2^2\cdot\alpha_1}{(4\cdot\pi\cdot\varepsilon_0\cdot\varepsilon)^2}}_{\textbf{Debye}}+\underbrace{\frac{3\cdot h\cdot\alpha_1\cdot\alpha_1}{4\cdot(4\cdot\pi\cdot\varepsilon_0\cdot\varepsilon)^2}}_{\textbf{London}}] \quad (1.1)$$

Where;

r is the average distance between two molecules of interest,

μ_1 and μ_2 are the dipole moment of molecules,

ε_0 is the vacuum permittivity,

ε is the relative permittivity,

K_B is the Boltzmann constant,

T is the temperature,

α_1 and α_2 are the polarizability of molecules.

As we can see from Eq. 1.1, Van der Waals forces consist of three terms :

- **Keesom forces**: Interactions between permanent dipole and permanent dipole,
- **Debye forces**: Interactions between permanent dipole and induced dipole,
- **London disperdion forces**: Interactions between induced dipole and induced dipole.

Double Layer Forces

Immersing a solid material into liquid induces charges to the surface of material which is originated from hydroxide and/or oxonium ions. In the case of AFM imaging, the cantilever immerses into buffer solution for analyzing the sample surface. The charge interactions at the solid-liquid interface yield the double layer electrostatic force. These forces are repulsive and on the order of one to a few tens of nanometer. The range of the double layer electrostatic force is approximate to Debye length, λ_D.

$$\lambda_D = \sqrt{\frac{\varepsilon_0 \varepsilon_r k_B T}{\Sigma_{i=1}^{N} q_i^2 n_i}} \tag{1.2}$$

Where ε_0 is the electric constant, ε_r is the relative dielectric constant, k_B is Boltzmann's constant and T is temperature. If we consider the system constituted of N number different species of charges, the i-th species carries charge q_i and have mean concentration of n_i.

Derjaguin - Landau - Verwey - Overbeck (DLVO) Theory

The stability of colloidal dispersions has been studied by Derjaguin and Landau in 1941. They introduced a theory that concerns the stabilization of strong short-ranged van der Waals attractions by electrostatic repulsions [10]. Seven years later, Verwey and Overbeek obtained independently the same results [11]. Afterwards, this called as Derjaguin - Landau - Verwey - Overbeck (DLVO) theory by Russel et al. [12].

DLVO theory refers the generated forces when two charged surfaces interact through a liquid medium. DLVO interaction is limited by low surface potentials since it is computed in the mean field approximations. Thereby, DLVO theory neglects all fluctuations in the center of the contact area. All strong and short-ranged interactions between the ions and molecules of the medium thus described under the category of *non - DLVO forces*.

Capillary Forces

Capillary forces occurs when the relative humidity of the environment rises over 30 % since this results a monolayer of water on the surface of analyte. The contact of the tip with the water monolayer produces a meniscus that pulls the tip towards the sample surface. This interaction can be expressed by Laplace pressure, P_L.

$$P_L = \gamma \cdot (\frac{1}{r_1} + \frac{1}{r_2}) = \gamma \cdot r_K \tag{1.3}$$

Where γ is the surface tension, r_1 and r_2 are radii of the meniscus and r_K is Kelvin radius.

The relation between the pressure (P) and force (F) is given by Eq.1.4.

$$P = \frac{F}{S} \tag{1.4}$$

Where S is the contact area of meniscus to the sample surface.

By using both Eq.1.3 and 1.4, the Laplace (capillary) force can be obtained.

$$F = \frac{\gamma \cdot S}{r_K} = \frac{\gamma \cdot 2 \cdot \pi \cdot R \cdot d}{r_K} \tag{1.5}$$

Where R is the tip radius and d is the penetration depth of the tip into liquid.

The amount of capillary forces is in order of a few nano Newton.

Hydrophobic Forces

Hydrophobic effects are raised from the long-ranged attractive forces that appears between hydrophobic surfaces and aqueous solutions. The hydrophobic materials are nonpolar substances that have molecules poor in charge or atoms capable of creating hydrogen binding. These substances have tendency to aggregate in aqueous solutions and exclude water molecules.

Hydrophobic effect is crucial for insertion of membrane proteins into the nonpolar lipid environment, formation of lipid membrane bilayers and micelles. Hydrophobic forces are stronger than van der Waals forces and their range is around tens of nm.

1.1.1.3 Operating modes of atomic force microscopy

Contact mode is the first imaging mode followed by oscillating contact mode. In this part, we will explain these main operating modes of atomic force microscopy with a recent developed mode, called Peak Force mode.

1.1.1.4 Contact mode

The contact mode is the first and the most basic imaging mode of atomic force microscopy. It consists of scanning the sample surface line by line by maintaining constant the interaction force between the tip and sample. AFM tip is always in contact with the surface resulting relatively large lateral forces. However, very high resolutions can be attained without harming the sample by moderating the applied forces from tip to the surface.

Recording the displacement of Z-piezo for each X and Y points provides to obtain the topography of the sample, called as *Height image*.

During the scanning of the surface an error signal occurs. This is partly due to the reaction time of electronics or/and piezoelectric ceramics. This error signal can be used to obtain *Deflection image* that gives a distinct topography of the surface.

To complementary to the topography of sample, the contact mode can also detail the chemistry of the surface by measuring the torsion of lever via the photodetector. Since the friction depends on the constituent material, *Friction image* provides the distribution of chemical components.

1.1.1.5 Oscillating contact mode

In oscillating contact mode, the AFM tip scans the surface of the sample with an impulsive contact.

The fact that keeping the tip-surface contact for a short time, the high lateral forces can be avoided, accordingly weakly attached samples on the surface can be analyzed without harming or moving.

The AFM tip oscillates at/or near its resonance frequency (first harmonic are often used but other harmonics can be used) with amplitude of tens nanometer. The oscillation of cantilever is governed by a bimorph piezoelectric that leads the sinusoidal movement of cantilever ($A_e = \cos \omega t$). The motion of cantilever can be described by harmonic oscillator model.

$$F_d = m \cdot \frac{\partial^2 z}{\partial t^2} + \gamma \cdot \frac{\partial z}{\partial t} + k_c \cdot z \tag{1.6}$$

with F_d the driving force, m the effective mass of the cantilever, z the displacement of the lever, γ the damping factor and k_c the spring constant of the cantilever.

At the resonance condition, the amplitude takes the maximum value and given by $A_R = A_0 \cdot Q$, where A_0 and Q are the free amplitude of the lever and the quality factor, respectively. Q is defined by the ratio of the stored energy in the system to the energy dissipated per cycle.

A typical oscillating contact mode operation includes the use of the amplitude modulation detection and the lock-in amplifier which provide to keep constant the amplitude of cantilever for a chosen drive frequency. For that, the tip-sample distance is adjusted by system during whole operation.

The amplitude is the one of the most important value to consider at oscillating contact mode operation because the direct control of the forces between the tip and sample is absent. However, the average response to the tip-sample interactions can be obtained from the amplitude versus the tip-sample distance curve.

Topography image is constructed, similar to contact mode, by detection of the movement of the Z-piezo in function of XY scanning. Oscillating contact mode offers two types of image apart from topography (*Height image*). One can be obtained by mean squared error of detected amplitude signal. *Amplitude image* provides information about the elasticity of the sample. During the oscillation of cantilever, a phase shift occurs due to the tip-sample interactions.

Thereby, the detected amplitude is expressed by $A_d = \cos(\omega t + \varphi)$. *Phase image* is based on the variation of φ and it presents the local changes of viscoelasticity.

1.1.1.6 PeakForce mode

Peak Force mode is a relatively recent AFM mode which combines both oscillating contact and contact mode. However, the recording of force curves for each contact point distinguishes Peak Force mode from the oscillating contact mode. The cantilever oscillates at far below from its own resonance frequency over the surface. The force curve oscillation was set at 2 kHz (for all images presented in the manuscript). The feedback loop maintains the oscillating amplitude during whole Peak Force operation, although the peak force on the probe is also controlled. Peak Force enables a soft contact between the tip and sample since the applied force is in the order of a few pN that is much lower than the applied force in oscillating contact or contact mode. Therefore, this mode is well adapted for soft and delicate samples such as polymers or biomolecules.

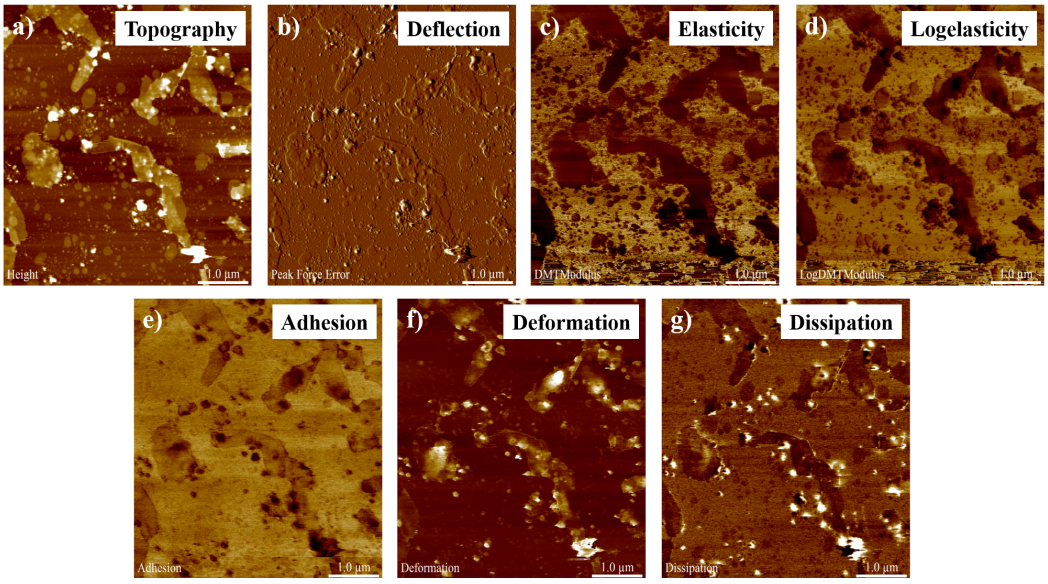

Fig. 1.2: AFM image of human monocyte rafts obtained by Peak Force mode. (a) Topography, (b) signal error, (c) modulus (elasticity), (d) LogModulus, (e) adhesion, (f) deformation and (g) dissipation image.

We have used Peak Force mode for imaging our soft samples (proteins, cells, lipid bilayers) and our corrugated substrates. By consistently controlling the short range interaction forces, PeakForce Tapping enables to control image quality with fewer artifacts linked to complication of the tip surface interactions and cantilever dynamics, particularly in liquid environment. Previously to each HS-AFM experiments, the deposition procedure has been checked on 1.5 mm disk using the Peak Force mode in liquid.

The most advantageous part of Peak Force mode is the mapping of the nanomechanical properties of a surface. Figure 1.2 presents an example of the different images can be obtained by Peak Force mode.

The information about the elasticity, adhesion, deformation and dissipation can be extracted from the approach-retract curves. Figure 1.3 illustrates the approach-retract curves highlighting different force fields.

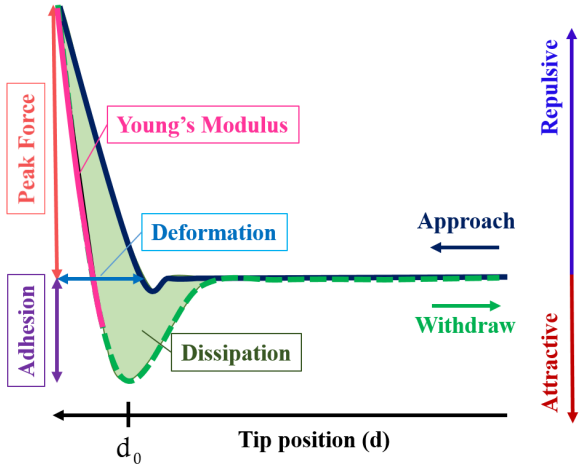

Fig. 1.3: Force curve highlighting different images modes of Peak Force oscillating contact.

A specific type of data can be acquired from each contact point in order to generate corresponding images.

Adhesion Image

The adhesion between the tip and the sample can be measured from the force curve. The difference between the base line and the pull-of point corresponds to the maximum adhesion force.

Elasticity Image

The reduced Young's modulus can be deduced from the force curve by fitting the retract curve. The fitting area is at the contact point and shown by the pink line in Fig.1.3.

Young's modulus can be calculated using different contact geometries. The simplest model uses Hertzian geometry which considers the tip as a classic rigid sphere on a flat surface. The Hertz model is valided for indentations significantly smaller than the sphere radius. Another contact geometry called Sneddon model where the tip-sample contact is defined as a contact between a rigid conical indenter and a soft flat sample. This model assumes that the surface is half-space deformed because of the indenter and it includes the penetration depth into calculation of Young's modulus. For the Sneddon model, the indentation has to be so large that the cone apex can be considered infinitely sharp. On very soft samples (e.g. cells, tissues, biomolecules), the tip often indents well past the very tip, even with the best force control, so the Sneddon model is often a better model for biological samples. Both models do not include adhesion or visco-elasticity. Figure 1.4 presents Hertzian and Sneddon geometries. Softer samples often require larger force curve ramp size.

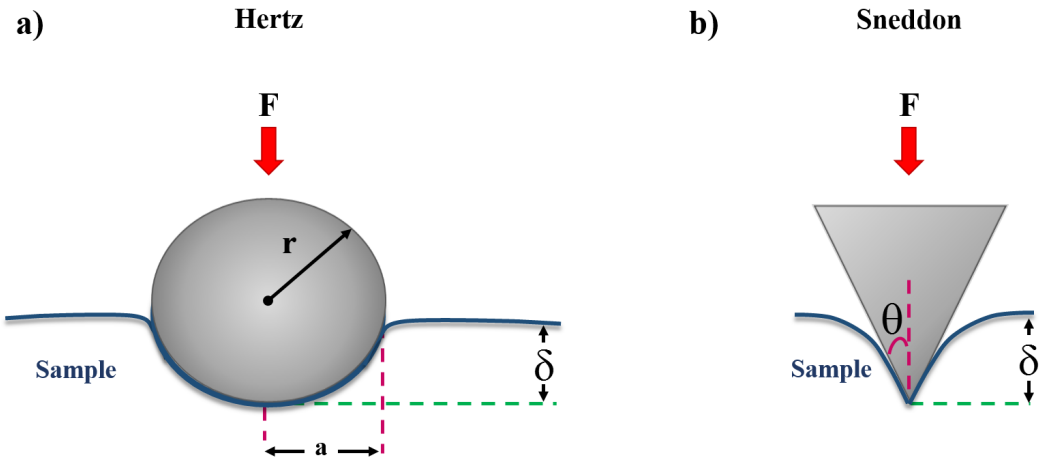

Fig. 1.4: Contact geometries for Young's modulus calculations. (a) Hertzian and (b) Sneddon geometry. r and a the radius of sphere and the contact area, respectively. δ is the deformation of the sample due to applied force F. θ is semi-opening angle of indenter.

Derjaguin - Muller - Toropov (DMT) and Johnson - Kendall - Roberts (JKR) models are based on spherical geometry. JKR approximation considers that the adhesion forces are at the outside of the contact area and neglected whereas the elastic stresses at the edge of the contact are infinite as in linear elastic fracture mechanics. On the other hand, DMT approximation involves the adhesion forces but the geometry is assumed as Hertzian where the adhesion forces could not deform the surfaces.

DMT model comprises only attractive long-ranged forces by considering the interaction between the tip and sample is the out of the contact area. This model assumes that only the sphere is deformable. DMT model superposes adhesion outside of the area of contact as predicted by the Hertz model. DMT model is practical for poorly flexible samples, having low adhesive properties and low contact radius a.

JKR model involves attractive short-ranged forces generated from the tip-sample interaction in the contact area. This assumption is mainly applicable for the samples with high adhesive properties and large contact radius a.

Different JKR-DMT transition solutions for adhesive rough surface contact have been developed utilizing Maugis-Dugdale (MD) transition theory with different forms of the contact area, the use of contact and non-contact mode. The non-slipping Maugis – Dugdale model is expected to have a broader range of validity in comparison with the non-slipping JKR model. On our commercial AFM, Maugis - Dugdale model was not implemented.

Model	Assumptions	Restrictions
Hertz	No surface forces.	Not applied to small loads in the presence of surface forces.
DMT	Long-ranged surface forces act only at the outside of the contact area. Model geometry is Hertz model.	Contact area can be decreased due to the limited geometry. Applied only to small adhesion parameter.
JKR	Short-ranged surface forces act only at the contact area.	Force magnitude can be decreased due to surface forces. Applied only to large adhesion.
Maugis-Dugdale	Tip-sample interface is modeled as a ring.	The solution is analytical but equations are parametric. Applied to all adhesion values.

Fig. 1.5: The mechanical parameters of elasticity assumptions.

Here, we summarize the mechanical parameters of elasticity assumptions based on Hertzian geometry (see Fig.1.4.(a)). A sphere with radius r contacts with the surface due to applied forces F. The adhesion force F_{Adh}, the contact radius with (a) and without (a_0) applied forces, and the deformation δ are given for Hertz, DMT and JKR models in Tab.1.1.

Tab. 1.1: The mechanical parameters of elasticity assumptions based on Hertzian geometry.

	Hertz	**DMT**	**JKR**
$\mathbf{F}_{Adh}$	0	$2\pi rW$	$3/2\pi rW$
$\mathbf{a}$	$(\frac{rF}{K})^{1/3}$	$((F+2\pi rW)\frac{r}{K})^{1/3}$	$(\frac{r}{K}(F+3\pi rW+\sqrt{6\pi rWF+(3\pi rW)^2}))^{1/3}$
$\mathbf{a}_0$	0	$(\frac{2\pi r^2W}{K})^{1/3}$	$(\frac{6\pi r^2W}{K})^{1/3}$
δ	$\frac{a^2}{r}=\frac{F}{Ka}$	$\frac{a^2}{r}$	$\frac{a^2}{r}-\frac{3}{2}\sqrt{\frac{6\pi Wa}{K}}$

The Peak Force QNM mode calculates the mechanical properties of the sample directly from the force curve of every interaction between tip and sample analyzed in real-time. We can choose between Hertz/DMT (spherical) or Sneddon (conical) models. Hertz/DMT model is convenient for the samples which have low adhesive properties. We have used Sneddon model for very deformable sample (cells). In the case of bacteria analysis, most of the samples are too stiff to accurately measure in the same conditions and apply the Sneddon model. Equation 1.7 presents Young's modulus, $E^{\ddagger}$, calculated from DMT model.

$$E^{\ddagger} = \frac{3}{4} \cdot \frac{F - F_{adh}}{\sqrt{r \cdot d^3}} \tag{1.7}$$

Where d is the tip-sample spacing.

Peak Force operation requires an estimation of the tip radius and the spring constant of the cantilever as well as the Poisson's ratio of the sample prior to Young's modulus calculations. However, the radius and the spring constant of the tip can be calculated experimentally during the calibration process of Peak force mode. Poisson's ratio ν, is related to the stiffness of the sample k_s, and this relationship is given by Eq.1.8.

$$k_s = 2a\frac{E^{\ddagger}}{1 - \nu^2} \tag{1.8}$$

Poisson's ratio is a coefficient which depends on Young's modulus of the material. Table 1.2 presents Poisson's ratio of diverse materials.

Tab. 1.2: Poisson's ratio of diverse materials for Peak Force elasticity image.

Material	**Young's modulus $E^{\ddagger}$**	**Poisson's ratio**
Cells		
PDMS	$E^{\ddagger} < 100$ MPa	**0.5**
PVA gels		
Protein		
Teflon	$0.1 < E^{\ddagger} < 1$ GPa	**0.4**
Crystals		
Collagen		
Polystyrene	$1 < E^{\ddagger} < 10$ GPa	**0.3**
Bacteriophage capsids		

Additionally, Peak Force QNM mode also provides *LogModulus Image* that is the logarithm of the elasticity of the sample. The complete force curve is analyzed in real-time allowing adhesion, deformation, dissipation mapping simultaneously with topography.

Deformation Image

The deformation caused by tip can be measured directly from force curves. It corresponds to the distance between the contact point (d_0) and the point where the cantilever changes its movement direction.

Dissipation Image

Energy dissipation is described by the applied force times the vertical velocity of tip integrated over one period of vibration. Energy dissipation (W_D) is expressed by

$$W_D = \int_0^T \overrightarrow{F} \bullet \overrightarrow{\nu} dt = \int \overrightarrow{F} \bullet \overrightarrow{dZ} \tag{1.9}$$

Where $\overrightarrow{F}$ is the interaction force vector, $\overrightarrow{\nu}$ is the velocity vector of the tip, T is the period of the cantilever vibration and $\overrightarrow{dZ}$ is the displacement vector of the tip.

The dissipated energy for each cycle corresponds the hysteresis between the approach and retract curves (see Fig.1.3). This mechanical energy loss is stated by eV scale on the dissipation image. However, when the deformation is purely elastic the dissipation energy will be very low and the approach and retract curves coincide.

1.1.2 Basics of High-Speed Atomic Force Microscopy

Atomic force microscopy has been developed very quickly and remarkably since its invention. Many scientist of the field worked to attain a high scan rates without sacrificing the quality of image.

Hansma's group started in early stage of AFM history to looking for the dynamic analyses. In 1989, they observed the dynamics of the fibrin clotting process by achieving $\sim$ 1 image/min with contact mode [13]. This study was followed by observing the viral infections of isolated cells [14] and antibody binding process [15].

Just one year after these initial results, in 1993, Engel's group investigated the scan speed limit of contact mode by theoretical calculations [16].

For the first time, Quate's group worked on the increasing of the scan speed. For this aim, they developed a cantilever with integrated piezoresistive sensors and integrated piezoelectric actuators in 1995 [17]. One year later, they implemented their device to analyze a gold patterned Nb-doped $SrTiO_3$ substrate. They archived an image of 100 μm $\times$ 100 μm less than 15 s [18]. The same year, Hansma's group fabricated short cantilevers [19] and a new optical deflection detector [20] in order to reach high scan rates. In 1997, they investigated Escherichia coli RNA polymerase activity by AFM with $\sim$ 30 s scan rate [21]. Following year, an image of DNA is procured in 1.7 s [22].

Ando's group started to develop the high-speed scanners in 1994 and the miniaturized cantilevers in 1997. However, a more extensive high-speed AFM including the short cantilevers, the high-speed scanner, the fast electronics and the optical beam detector is reported in 2001 and 2002 [23, 24].

Using this system, Ando's group observed the motion on myosin V with an imaging rate of 12.5 images /s.

The recent improvement of high-speed atomic force microscopy involves coupling with total internal reflection fluorescence microscopy (TIRFM). In 2013, Ando's group presented chitinase moving on a chitin crystalline fiber and myosin V walking on an actin filament by simultaneous HS-AFM/TIRFM imaging [25].

1.1.3 Requirements of high speed scanning

The development of high–speed atomic force microscopy arises from the aim of observing biomolecular interactions that occur in millisecond time range. Dynamic investigations, thereby, requires such a device whose scan rate fast enough to capture biological events. In order to archive high temporal resolution with AFM, various devices and techniques have been developed by Pr. Ando and his research team. Here, we will discuss the conditions to fill to reach high speed AFM imaging.

The dynamic of biomolecules can be observed when an analyte is softly attached on the surface. The strong interactions between the surface and analyte may result immobilization of the sample since the dynamic process occurs on the surface due to weak interactions between biomolecules. For following dynamic events, the tip of cantilever should be in soft contact with the sample. There are several ways to reduce the tapping force, thereby archive a soft contact. It can be listed by decreasing of the spring constant of the cantilever, k_c, increasing of the quality factor of cantilever, Q_c and reducing the cantilever's oscillation amplitude. However, all these conditions can provide a soft contact but they are not convenient for high speed scanning. For this reason, Pr. Ando and his research team developed novel electronic components to overcome time delay related to the soft contact. Before to detail these electronics and the working mechanism of HS-AFM, we will mention all the time delays that need to be decreased.

1.1.3.1 A rough approximate of feedback bandwidth for high speed scanning

The feedback bandwidth determines the fastness of the response. We can approximately calculate the feedback bandwidth for high speed AFM imaging.

If we consider to capture an AFM image of $R \times R$ size with N number of scan lines in t acquisition time, the scan velocity of the tip in X-direction can be expressed by $V_S = 2 \cdot R \cdot N/t$. This approach addresses to flat surfaces. If the surface roughness is taken into account and assumed as a sinusoidal with periodicity λ_s, the scanning operation requires a feedback bandwidth at frequency $f = V_S/\lambda_s \cdot t$. In order to maintain the sample - tip spacing, the feedback bandwidth, f_B, need to be equal or greater than f.

$$f_B \geq \frac{2 \cdot R \cdot N}{\lambda_s \cdot t} \tag{1.10}$$

For example, if we would like to obtain an AFM image of lipid rafts, which has maximum sample height $h_0 \approx 10$ nm, at 300×300 nm^2 size with 150 scan lines in 600 ms acquisition time, the feedback bandwidth should be $f_B = 15$ kHz.

1.1.3.2 Time delay between open-loop and closed-loop

Closed-loop AFM systems provide to maintain the position of setpoint and it removes the image distortion caused by the hysteresis and nonlinearity of piezoscanners. Accordingly, the closed-loop systems enable to nanopositioning on the sample. Here, we use the relationship between the closed-loop and open-loop in order to investigate the origin of the time delay in closed-loop AFM systems.

If we assume the sample height variations as the input signal to the system and define it as $U_{in}(t)$, the observed variations at the Z-scanner can be considered as the output signal, $U_{out}(t)$. The time dependence of the closed-loop is related to the open-loop and this relationship can be given by a transfer function K(S).

$$K(S) = \frac{-T(S)}{1 + T(S)} \tag{1.11}$$

Where T(S) represents the open-loop transfer function and it depends each component of the system including the cantilever, sensor, proportional-integral-differential (PID) feedback controller and scanner.

$$T(S) = \underbrace{C(S)}_{\textbf{cantilever}} \cdot \underbrace{A(S)}_{\textbf{sensor}} \cdot \underbrace{H(S)}_{\textbf{PID}} \cdot \underbrace{G(S)}_{\textbf{scanner}} \tag{1.12}$$

The time dependence of the open-loop transfer function can be expressed by

$$T(S) = T_0(\omega) \cdot e^{-i\varphi(\omega)} \tag{1.13}$$

Where T_0 is the gain and $\varphi(\omega)$ is the phase delay. By substituting this relationship into the Eq.1.11, we can obtain the time dependence of $K(\omega)$.

$$K(\omega) = \frac{-(T_0 \cdot \cos\varphi(\omega) + T_0^2) + i \cdot \sin\varphi(\omega)}{1 + 2 \cdot T_0 \cdot \cos\varphi(\omega) + T_0^2} \tag{1.14}$$

From this equation, we can define the amplitude, $K_0(\omega)$, and the phase delay, $\Phi(\omega)$, of the closed-loop.

$$K_0(\omega) = \frac{T_0}{\sqrt{1 + 2 \cdot T_0 \cdot \cos\varphi(\omega) + T_0^2}} \tag{1.15}$$

$$\Phi(\omega) = \arctan[\frac{-\sin\varphi(\omega)}{T_0 + \cos\varphi(\omega)}] \tag{1.16}$$

If we consider that the feedback gain is $K_0(\omega) \approx 1$, the gain of the open-loop can be estimated as $T_0(\omega) = -1/2 \cdot \cos\varphi(\omega)$. By substituting this result into Eq. 1.16, we can find the relationship between phase delay of both closed-loop and open-loop.

$$\Phi(\omega) = \pi - \varphi(\omega) = 2 \cdot \varphi(\omega) \tag{1.17}$$

This result indicates that the phase delay of the closed-loop is approximately two times larger than the open-loop phase delay.

The time delay in the closed-loop can be estimated by considering each time delay originated from including devices in the system. Following this approach, the open-loop phase delay given by $\varphi(\omega) \approx 2\pi f \Delta\tau$. f corresponds to the feedback frequency and $\Delta\tau$ is the total time delay in open-loop which obtained by summing

the time delay of each component. Consequently, the time delay of closed-loop given by $\Phi(\omega) = 4\pi f \Delta\tau$ (see Eq.1.17). From this result, the feedback bandwidth can be obtained since it is generally defined as feedback frequency that results in a phase delay of $\pi/4$. Accordingly, the feedback bandwidth f_B is expressed by

$$f_B = \alpha \cdot \frac{f_c}{8} / [1 + \frac{2 \cdot Q_c}{\pi} + \frac{2 \cdot Q_s \cdot f_c}{\pi \cdot f_s} + 2 \cdot f_c \cdot (\tau_p + \tau_I + \delta)] \tag{1.18}$$

Where ;

α is a coefficient related to the phase compensation effect results from D component of PID feedback controller or from an additional phase compensator,

$\tau_c = \dfrac{Q_c}{\pi \cdot f_c}$ is the cantilever response time,

$\tau_s = \dfrac{Q_s}{\pi \cdot f_s}$ is the z-scanner response time,

$\tau_r = \dfrac{1}{2 \cdot f_c}$ is the reading time of the cantilever oscillation amplitude,

τ_p is the parachuting time,

τ_I is the integral time of error signals in the PID feedback controller,

δ is the sum of other time delays.

Equation 1.18 aid to understand the origin of the closed-loop time delay. Therefore, we will focus each term of the equation.

The integral time delay, τ_I, and the parachuting time, τ_p, are two parameters difficult to estimate theoretically. However, τ_I depends on the entire operation in the PID feedback and it arises when the closed-loop time delay increases. The detailed information about the integral time delay τ_I is given in literature [26, 27]. The parachuting time can be defined as the landing time of the cantilever when it is totally detached from the surface during the scanning. It depends on the resonance frequency of cantilever f_c, the periodicity of sample roughness λ and the scanning velocity in X-direction V_S. Regarding the cantilever response time τ_c and the reading time of cantilever oscillation amplitude τ_r, we can see that also these two parameters depend on the cantilever resonance frequency. As a result it is important to highlight here that the cantilever resonance frequency has a large impact on the time delay of the closed-loop feedback. Besides, the resonance frequency of piezoelectric scanners has an influence on the feedback bandwidth.

Tab. 1.3: List of developments for HS-AFM.

Equipment	**Improvement**
Cantilever	Miniaturization
	High resonance frequency
	Small spring constant
OBD Detector	Adaptation to small cantilevers
Scanner	Decoupled X-Y-Z scanner with low resonance frequency
PID Feedback Controller	Fast response due to large feedback width f_B
Drift Compensator	Regulation of the drift in the cantilever - excitation efficiency

According to these results, a series of development has been implemented by Pr. Ando and his research team in order to achieve high-speed scanning. Therefore, several electronics and cantilevers have been designed. Here, we list these improvements in Tab.1.3 and we will detail them in next section.

1.1.4 High–speed atomic force microscope base

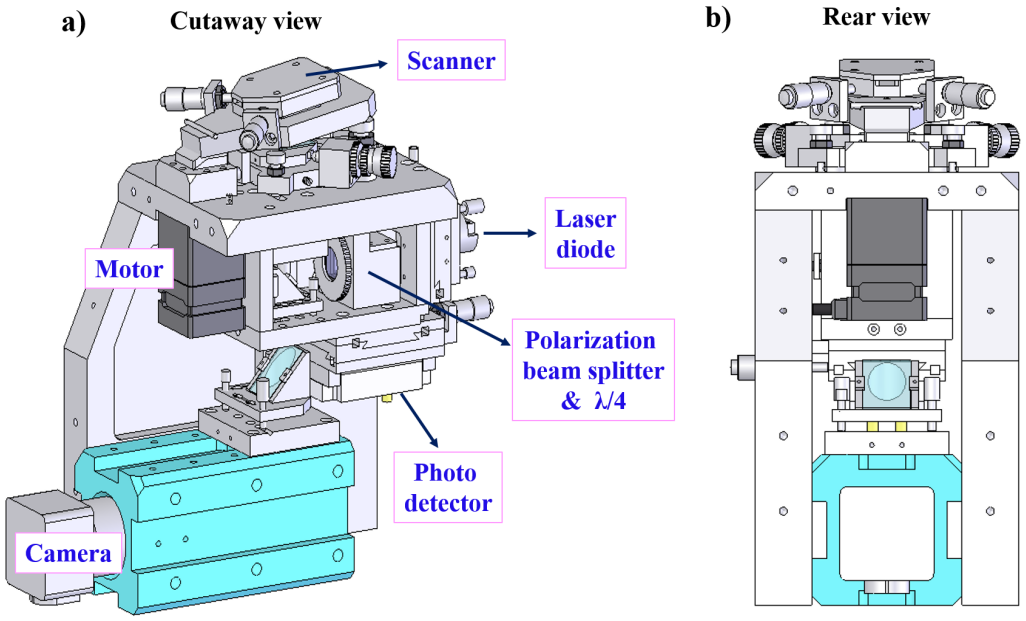

Fig. 1.6: 3D Schematic representation of HS-AFM. (a) Cutaway view and (b) rear view are presented.

High-speed atomic force microscope setup is presented in Fig.1.6. This sophisticate system involves the high-speed scanner, sample stage, liquid cell, laser diode, motor, photodetector, camera and optical elements.

The working principle of HS-AFM is quite similar to conventional AFM system apart from the inverted cantilever - sample position. The laser spot focuses on the cantilever by passing though optical elements. The sample is deposited on a glass rod which is fixed onto Z-scanner. The cantilever oscillation and amplitude is controlled by Fourier analyzer. The deflected laser light is detected by the photodetector. Proportional – Integrated – Differential controller process both the scanner and cantilever signal in order to construct the topography of signal. The optical path is presented in Fig.1.7.

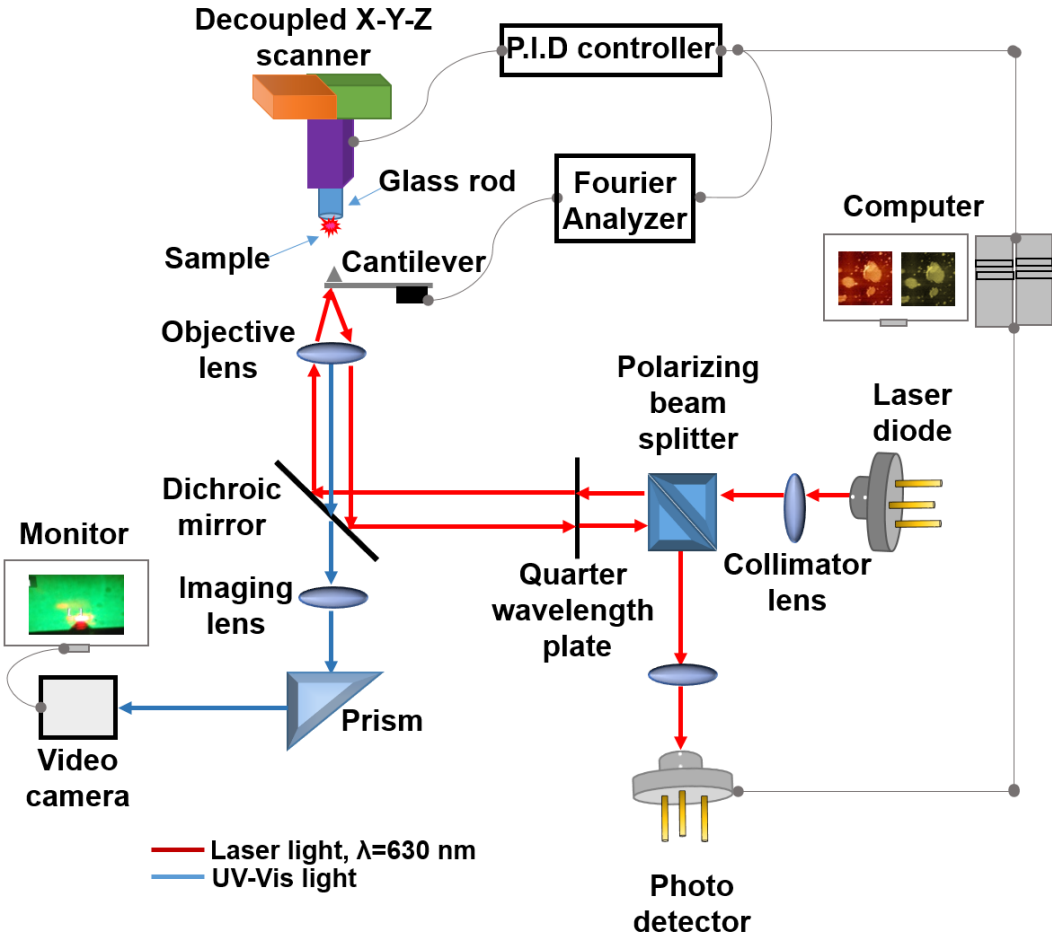

Fig. 1.7: Schematic drawing of HS-AFM.

After this overview of HS-AFM, we will introduce each component of the microscope.

1.1.5 High speed scanners

The development of scanner is crucial for achieving a successful high speed imaging. However, such mechanical devices can produce unwanted vibrations therefore it is necessary to effectuate an optimum design to damp these unwanted vibrations. There are some conditions need to implement in order to realize high speed scanners.

1. High resonant frequencies of scanners f_s,
2. Low quality factors of scanners Q_s (see Eq.1.18 for 1 and 2),
3. Small number of resonance peak with narrow frequency region,
4. Large displacement of scanners.

The fast displacement of the piezoelectric actuators also induce unwanted impulsive forces onto sample stage. These forces influence the piezoelectric actuators as well as the sample stage. Therefore, the high-speed scanners include a counterbalance in order to compensate the impulsive forces [23]. The system consist of two Z-scanners at the same length in opposite expanding directions (Fig.1.8.(a)). The sample stage is attached on each Z-scanner that balances the weight. However, the counterbalance is effective except at the vicinity of the resonance frequency of the scanners.

There are several designs can optimize the performance of counterbalance. The piezoelectric actuator can be sandwiched by two flexures in the displacement directions as seen from Fig.1.8.(b). In this arrangement, the center of mass is unable to realize a large displacement when the mechanical properties of two flexures are identical. This arrangement could implement to X- and Y-piezoelectric actuators. In order to adapt to Z-piezoelectric actuator, the resonance frequency of the flexure should be so high that it requires a high spring constant of the flexure and thereby the amount of scanner displacement drops.

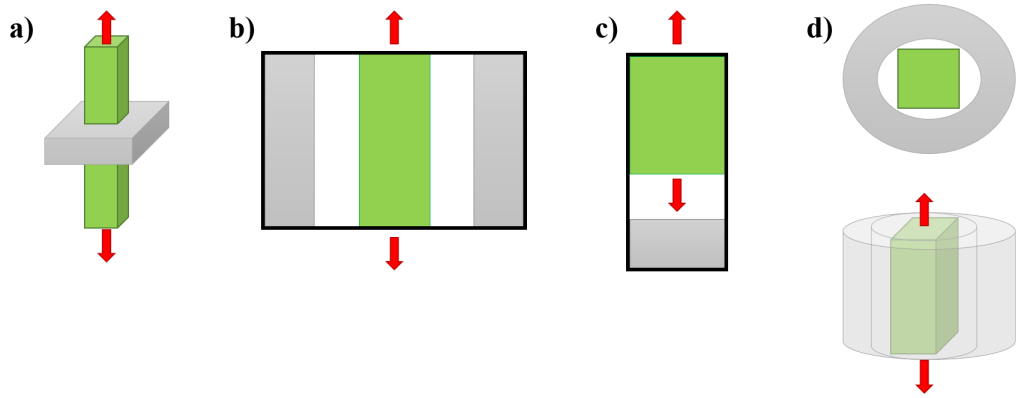

Fig. 1.8: Configurations of holding the piezoelectric actuators in order to damp unwanted vibrations. The piezoelectric actuators are shown in green, where the holders are presented in gray. (d) includes the top (top) and side (bottom) views of the configuration.

Another configuration is based on to held the piezoelectric actuator only at the rims of the plane perpendicular direction to the displacement (Fig.1.8.(c)). Thereby, two scanners can be displaced freely but the center of mass is almost motionless.

The last arrangement is presented in Fig.1.8.(d) where the piezoelectric actuator is fixed into a circular hole of the flexure. The piezoelectric actuator is held from the side rims parallel to the displacement directions therefore it can attain almost the maximum displacement. Ando et al. are used this configuration for the Z-scanner of HS-AFM.

The commercial AFM systems generally govern a tube scanner in which the resonance frequency is low for each X-, Y- and Z- directions. HS-AFM consist of decoupled X-, Y- and Z-piezoelectric scanners to attain high resonance frequencies. The design of scanner involves a compact asymmetric structure and materials with high Young's modulus to density ratio. However, in such design an interference between axes occurs and this can be avoided by including the flexures [28, 29]. The design of the HS-AFM scanner is presented in Fig.1.9.

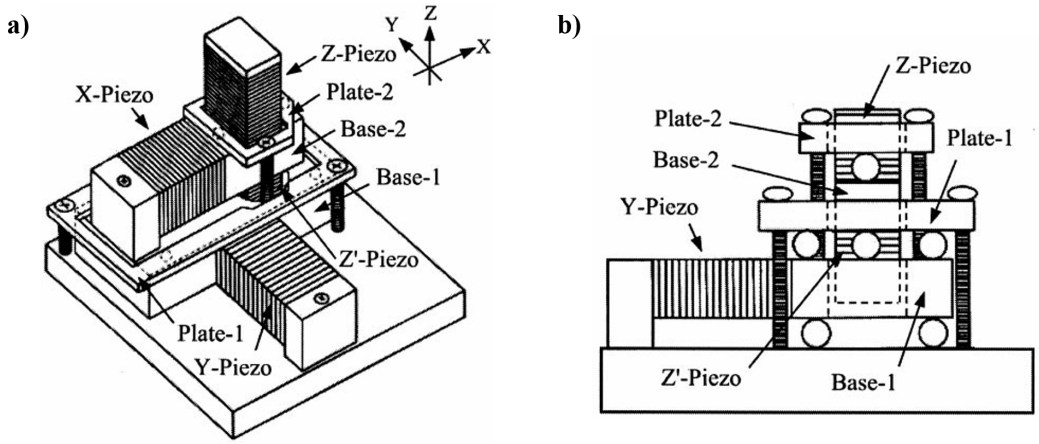

Fig. 1.9: Scanner assembly [23]. (a) Cutaway view and (b) rear view.

The HS-AFM scanner contains four piezoelectric actuators (X, Y, Z and Z') and two bases (Base-1 and Base-2). Base-1 supports the X-scanner while Base-2 holds the Z-scanner. Due to this geometry, the Y-scanner displace the X-scanner and the X-scanner displaces the Z-scanner. The gap between the scanners are filled by an elastomer to damp the unwanted vibrations. The sample stage is placed onto Z-scanner. To avoid the hydrodynamic effects, a glass rod with 1 mm diameter is used. It has been shown that a large sample stage induces a vibration onto the cantilever ($\sim$ 20 kHz) due to the hydrodynamic forces [24].

In our laboratory, we own three HS-AFM scanners with different scan ranges.

Tab. 1.4: List of HS-AFM scanners.

Scanner	**X-Y scan range**	**Z scan range**
Small	0.8 μm	0.2 μm
Wide	4.6 μm	2.5 μm
Ultra-Wide	35 μm	3 μm

1.1.6 Dynamic proportional – integral – differential controller and drift compensator

The high-speed scanning requires the minimal amount of force applied by the cantilever tip onto the sample surface. In order to obtain this soft contact condition, the amplitude setpoint, A_S, should be very close to the free oscillation peak-to-peak amplitude, $2A_0$. But in such condition, the cantilever tip has tendency to be detached from the surface. When it detaches, the cantilever tip is not enable to contact with the surface quickly. The main reason is the feedback operation is saturated due to poor error signal. In order to achieve the high-speed scanning and overcome these mentioned problems, Ando et al. have developed the dynamic PID (proportional–integral–differential) controller and the drift compensator [26, 27]. The dynamic PID controller prevents the feedback saturation while the drift compensator stabilizes the free oscillation amplitude of cantilever.

The conventional PID controllers able to compensate the time delay related to the parachuting via the gain parameters. However, the system still be remained unstable, especially for highly rough samples. Thus, Ando et al. used the peak-to-peak oscillation amplitude of the cantilever, A_{p-p}, instead of A_S to regulate the PID gain parameters. To do that, a circuit (dynamic operator) was inserted between the error signal output and the input of a conventional PID circuit. The dynamic operator has three horizontal branches including the upper and lower limit of the error signal while the true error signal passes through the middle branch. When the peak-to-peak oscillation amplitude is too high or low, the error signal is poor for conventional PID system and that slow down the response time of the feedback operation. The dynamic operator produces a false error signal when the peak-to-peak oscillation amplitude is too high or low. The false error signal is amplified and added to the true error signal (middle branch). Consequently, the increase of the final error signal provides a quicker feedback response and accordingly the systems turns back to the normal mode.

1.1.7 Fourier analyzer

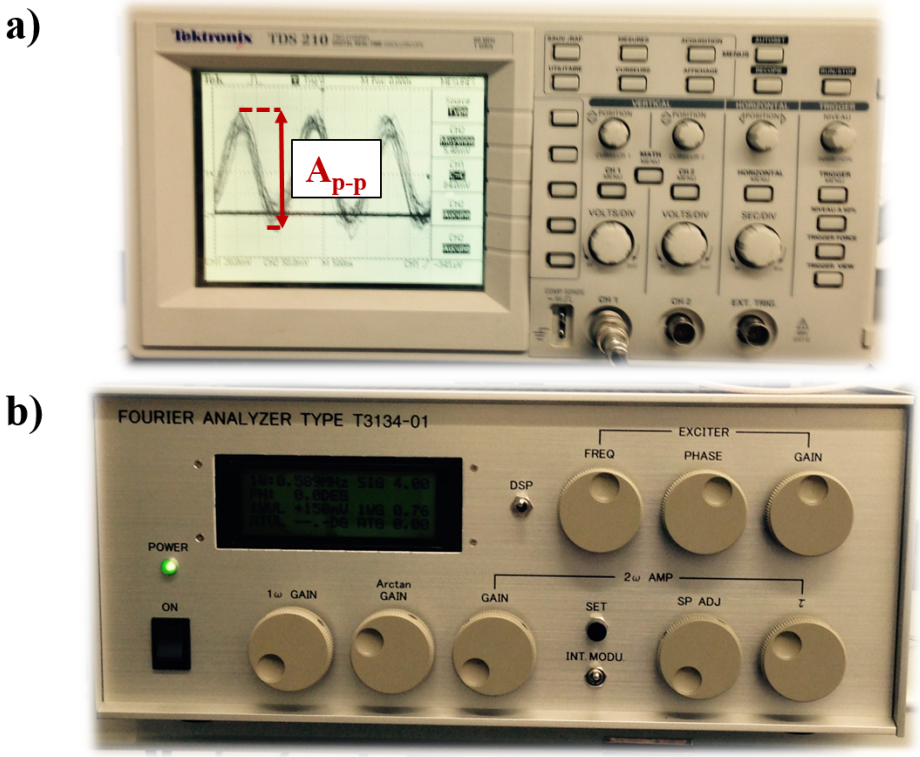

Fig. 1.10: (a) Oscilloscope. The peak-to-peak oscillation amplitude of the cantilever, A_{p-p}, is presented on the oscilloscope. (b) Fourier analyzer.

Fourier analyzer accomplishes several important tasks including excitation of the cantilever and the signal processing. Fourier analyzer provides to measure the resonance frequency of cantilever and to apply a stable excitation during the imaging process. The peak-to-peak oscillation amplitude and the phase variation of the cantilever can be measured via an oscilloscope, as shown in Fig.1.10.(a). The stabilization of the cantilever excitation is based on the amplitude of second harmonics of the cantilever oscillation which is memorized as an initial set point for each cycle of the excitation. Fourier analyzer is able to detect in real-time the amplitude and phase signal, and perform the signal processing for each cycle. Fourier analyzer can supply a frequency generation 10 to 1500 kHz which is accordant with the miniaturized cantilevers.

1.1.8 HS-AFM probes

The cantilevers play an important role for achieving high scan rates since they influence the amplitude detection time and the cantilever's response time [27, 24, 30]. To attain to the highest resonance frequency decreases the feedback delays. Thus, high speed imaging requires miniaturized cantilevers that can offer a high resonance frequency with a low spring constant. Decreasing the spring constant also enables to reduce the tapping force. The resonance frequency, f_c, of a rectangular cantilever with thickness d, width w, length L and the spring constant k_c is given by

$$f_c = 0.56 \cdot \frac{d}{L^2} \cdot \sqrt{\frac{E^{\ddagger}}{12 \cdot \rho}} \tag{1.19}$$

Where $E^{\ddagger}$ and ρ are Young's modulus and the density of the cantilever material, respectively. Young's modulus, $E^{\ddagger}$, is expressed as

$$E^{\ddagger} = k_c \cdot \frac{4 \cdot L^3}{w \cdot d^3}. \tag{1.20}$$

If we place the $E^{\ddagger}$ value in Eq.1.19, we obtain following equation:

$$f_c = 0.56 \cdot \frac{d}{L^2} \cdot \sqrt{\frac{k_c \cdot L^3}{3 \cdot w \cdot d^3 \cdot \rho}}. \tag{1.21}$$

Equation 1.21 indicates that for a given k_c, the dimensions and the mass of cantilever must be decreased in order to attain a higher resonance frequency value. Besides, the small cantilevers have a lower thermal noise. The total thermal noise of cantilever is given by

$$\sqrt{\frac{k_B \cdot T}{k_c}} \tag{1.22}$$

Where k_B is Boltzmann's constant and T is the temperature in Kelvin. This equation demonstrates that thermal noise decreases when the resonance frequency arises.

Figure 1.11 presents schematic presentation of a commercial HS-AFM probe (Olympus BL-AC10DS-A2). The ultra-small cantilever is sized in 9 $\times$ 2 μm, made from silicon nitride and coated with $\sim$ 20 nm of gold.

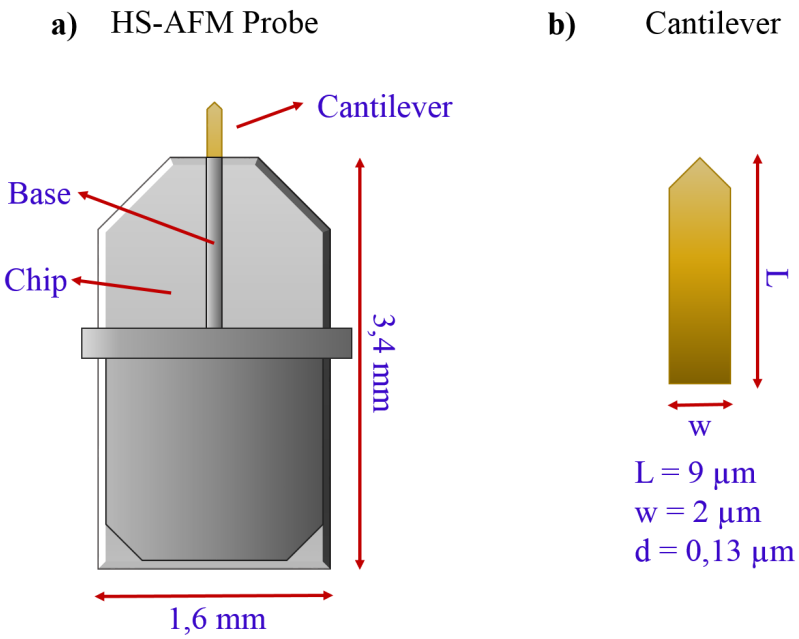

Fig. 1.11: Schematic presentation of HS-AFM (a) probe and (b) cantilever (Olympus BL-AC10DS-A2). L= length, w=width and d=thickness of cantilever.

This miniaturized cantilevers shows a high resonance frequency around 1.5 MHz in air and approximately 560 kHz in liquid while its spring constant is small and remains around 0.1 N/m. The resonance frequency of the cantilever in liquids is 10 times higher than conventional AFM cantilever, so that contributes to achieve scan rate of 10 frame per second or faster for 400 x 400 pixels. This HS-AFM probes are available with a carbon nanofiber (CNF) probe (Olympus BL-AC10FS-A2, tip radius 10 nm) for high resolution imaging and without CNF probe (Olympus BL-AC10DS-A2). This last reference has been preferably used for this project. We have used this basic cantilever without probe for modifying, e.g. depositing electron beam deposition (EBD) tip. An EBD tip with ∼10 nm radius and 1.5 – 4 μm length is grown at the corner of triangular protrusion at the end of bird-beak-like cantilever. However, the length of commercial carbon nanofiber tip ($\leq$ 0.1 μm) is not very convenient high dynamics. The design of tip is a crucial issue to avoid the hydrodynamic effects. Shorter tips cause a closer contact between the cantilever and sample during the imaging process.

Thereby, a higher pressure is applied by the cantilever on to the confined liquid medium between the cantilever and sample, accordingly to the sample, that results an oscillation damping. Ando et al. have shown that the oscillation amplitude is maintained constant during the contact process of the tip when the needle-shaped cantilever tips with 1 μm length have been used [31, 32]. Thus, we have purchased cantilevers without fiber tip and we have grown a tip by electron-beam-deposition on the extremity of cantilever.

1.1.8.1 Electron-Beam-Deposited tip fabrication

The achieving of high resolution AFM image is crucial for surface analyses. The specific structures in nanometer scale or highly rough substrates require a high image quality in order to observe their detailed topography. A sharp AFM tip can improve the resolution of an AFM image since the lateral resolution depends on apex radius (r) of the tip. Therefore single-walled carbon nanotube [33] and electron-beam-deposited (EBD) tips [34, 35] have been appended to the extremity of cantilevers. Also, a bent optical fiber is used instead of commercial AFM cantilevers [36].

Electron-beam-deposited tips provide some advantages over commercial and other type of integrated tips. The conductivity and the hydrophobic properties of the tip can be controlled by the choice of contaminant source. The shape and the length of the tip are tunable. Besides, it is possible to modify the shape of the tip by etching with reactive plasma. Consequently, these tips have a high aspect ratio, low thermal mass and high elastic modulus [28].

Prior to HS-AFM analyses, we have periodically fabricated EBD tips on commercial ultra-short cantilevers (Olympus BL-AC10DS-A2).

The EBD tip fabrications were carried out with a scanning electron microscopy (SEM, JEOL 6500). An electron beam focused onto conductive area, where EBD tip is desired, using the spot mode of SEM. The carbon growth is performed due to the presence of organic molecules in the vacuum chamber. Our procedure consists the injection of phenol gas to inside of the vacuum chamber using a small container. The cantilevers, 7 for each batch, are placed onto the container for EBD tip manufacturing.

The EBD tip fabrication procedure is applied to each cantilever one by one. Figure 1.12 presents SEM images of HS-AFM cantilever with an EBD tip.

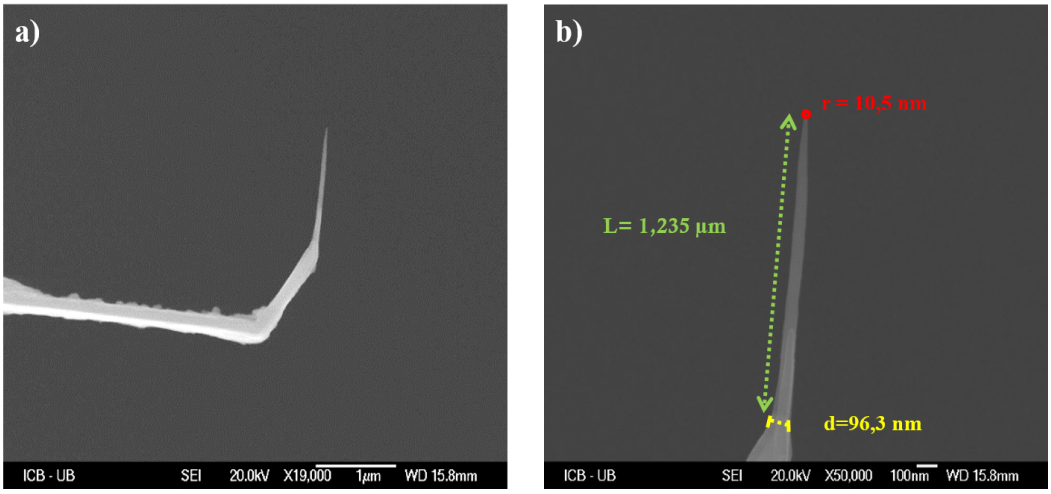

Fig. 1.12: SEM image of EBD tip on ultra-short cantilever (Olympus BL-AC10DS-A2). (a) Side view of cantilever and EBD tip. (b) Focus on EBD tip.

We have controlled the dimensions of electron-beam-deposited tip by varying the electron beam parameters. The length of EBD tip is adjusted by the exposure time of the electron spot. Magnification factor influences the diameter of grown tip. In order to achieve well-shaped sharp tips, it is necessary to have a well-aligned electron beam. A fine electron beam is focused directly down to the extremity of the cantilever at electron energy of 20 kV. The EBD tips are fabricated with full cone angle of 6°, length of 1.5 – 3.5 μm and diameter of apex down to ∼20 nm.

Tab. 1.5: EBD tip fabrication procedure performed on HS-AFM probes (Olympus BL-AC10DS-A2) by SEM (JEOL 6500) using phenol gas.

Magnification factor	**Time (second)**	**Repetition**
50.000	90	2
150.000	90	2
250.000	60	1 or 2

To fabricate an electron-beam-deposited tips, firstly the electron spot is exposed onto cantilever at low magnification factor during 90 seconds. After performing carbon growth on the cantilever, we returned to the imaging mode of SEM and refocused on the tip at higher magnification. The electron beam re-positioned onto extremity of the growth tip and the growth process activated in the spot mode. This procedure is repeated from lower to higher magnification factor until we obtain an EBD tip with desired length. Furthermore, this protocol is applied to used tips to regenerate them. In this case, the exposition parameters are adapted to current tip in order to procure efficient results. A typical procedure of EBD tip fabrication is resumed in Table 1.5.

1.1.9 Optical beam deflection detector

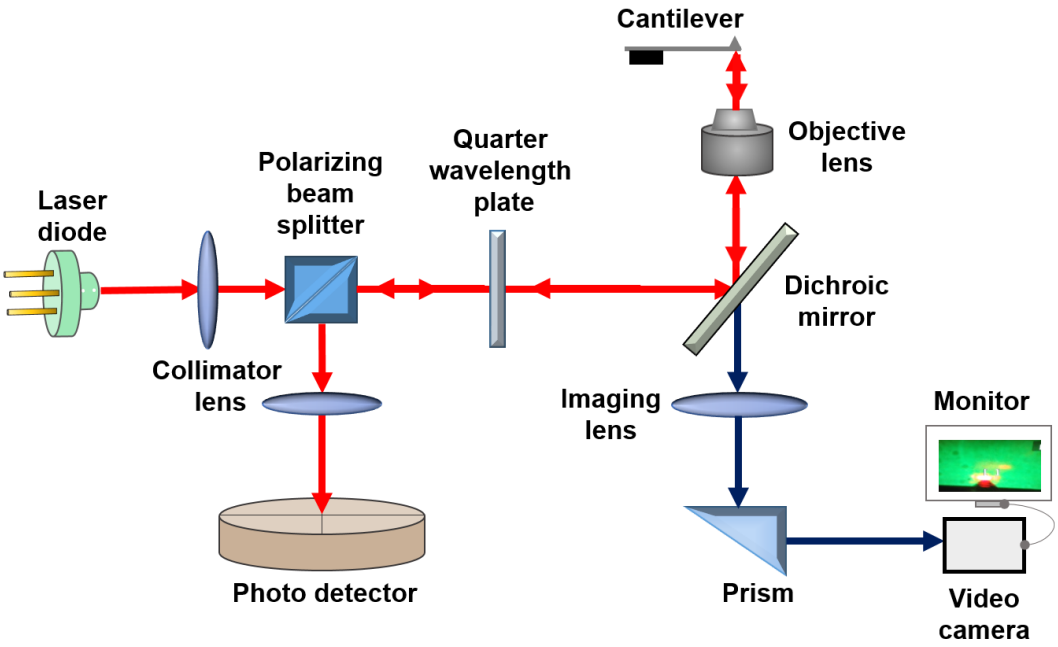

Fig. 1.13: Schematic drawing of HS-AFM optical detection system.

The optical detection system of high-speed atomic force microscopy (HS-AFM) is inverted in comparison with a commercial AFM microscope. More precisely, the sample is on the top of the cantilever. HS-AFM has a specialized optical detection system in order to detect the reflected laser light from miniaturized cantilever [23]. Figure 1.13 visualizes the optical detection system of HS-AFM.

A laser beam (λ = 670 nm) is focused on the cantilever via a collimator lens and an objective lens. The objective lens (Nikon, CFI S Plan Fluor ELWD 40 ×, W.D. 8 mm, N.A. 0.45) is also used for collecting back of the reflected light from the cantilever. The polarizing beam splitter and quarter wavelength plate separate the incident and the reflected light. The reflected light is directed towards the photo detector (4-segmented Si PIN photodiode, 3 pF, 40 MHz) that associated to a custom-made fast amplifier/signal conditioner ($\sim$ 20 MHz).

The high–speed atomic force microscopy probe is illuminated by a halogen lamp to visualize the cantilever and the laser spot which helps to position the laser spot on the edge of the cantilever. The halogen light is collected by the objective lens and passed through the dichroic mirror before to reach video camera.

Recenlty, a commercial high–speed atomic force microscopy became available on the market. Bruker Corporation developed Dimension FastScan AFM microscope and appropriate AFM probes. We have performed analysis on this microscope in order to compare and experiment the differences between comercial and prototype high–speed AFM microscopes.

1.1.10 Dimension FastScan microscope

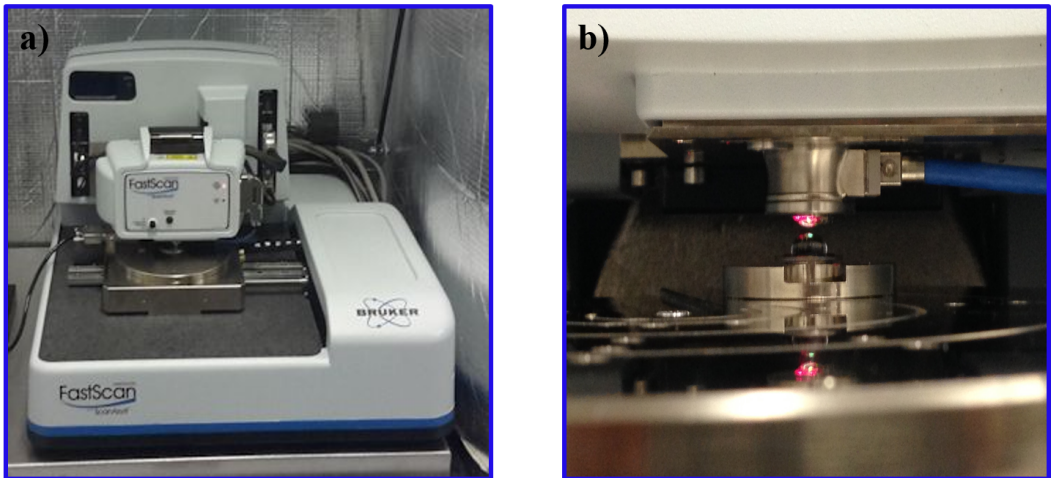

Fig. 1.14: Presentation of FastScan AFM microscope.

Dimension FastScan is a commercial high-speed atomic force microscopy developed by Bruker. This microscope has been developed with the support of Ando's group inside HS-AFM consortium.

The standard version of microscope enables to acquire an AFM image with maximum lateral range of 35 $\times$ 35 μm^2 until 3 μm heights. Involving the closed-loop system decreases the vertical noise below 40 pm. Dimension FastScan offers to zoom and analyze any area on the pre-scanned image without drifting. The analyzing software, Nanoscope, provides to tracking the entities on the surface. Conversely with HS-AFM, each step of the calibration process is automatized keeping the manual operating as an option. The scan rate may be attained almost ten times faster than conventional AFM (example: Multimode 8, Bruker). This microscope provides to gain time with the absence of a specific sample preparation, easiness of operating and relatively fast scan rates.

1.2 Surface Enhanced Raman Spectroscopy

In this section, we will introduce the relevant optical characterization techniques to our work. We have used surface enhanced Raman spectroscopy (SERS) that identifies the chemical properties of samples, therefore it is a complementary technique to AFM. The Raman signal enhancement involves metallic rough surfaces and the signal exaltation due to light - metal interaction is described by *Localized surface plasmon resonance (LSPR)*. LSPR is a specific case of *surface plasmon resonance (SPR)*, thus we presented here all SPR conditions briefly followed by the principle of *Raman spectroscopy* and *surface enhanced Raman scattering*.

1.2.1 Surface Plasmons and Localized Surface Plasmon Resonance

Surface plasmons are electro-magnetic waves that propagate in metallic interfaces when the free electrons of a metallic surface are in resonance with the incident photons. This electromagnetic excitation on the surface of metal is termed as surface plasmon polariton (SPP). Surface plasmons (or more precisely surface plasmon polaritons, SPPs) help to concentrate light on specific areas of a substrate by allowing to manipulate the light-matter interactions. Thus, surface plasmons have many potential in applications in optics, microscopy, sensors for molecule detection, opto-electronic circuit components and surface enhanced Raman scattering.

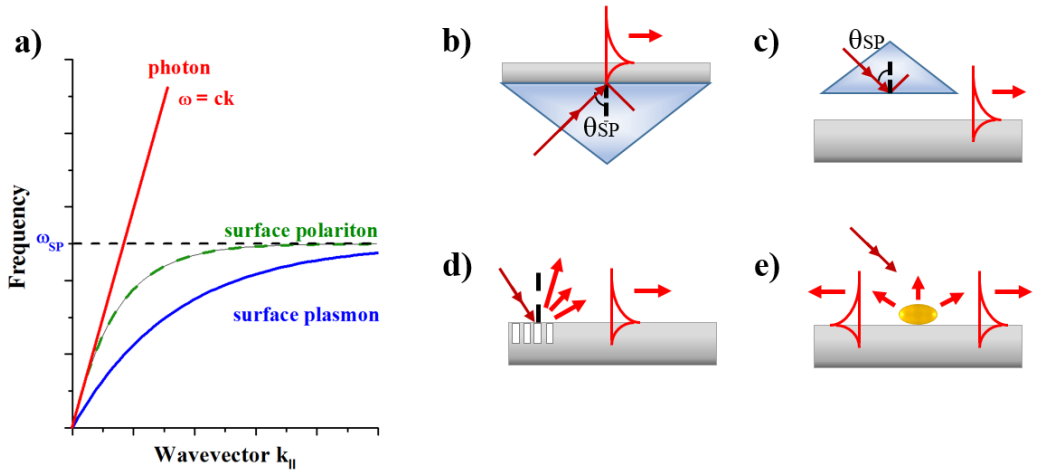

Fig. 1.15: (a) Dispersion curve of surface plasmon polaritons on a metal surface. (b) and (c) Kretschmann and Otto configurations, respectively. (d) Diffraction grating and (e) rough metal surface geometries.

A simple light illumination on the smooth metal surfaces is not enough to obtain surface plasmon polaritons (SPPs) since the wavevector of metal is greater than the incident photon wavevector ($k_{sp} > k$). Figure 1.15.(a) presents dispersion of surface plasmon modes on a metal surface. The surface plasmon modes are always under the light line without presenting any intersection. The excitation of SPP occurs only in one condition where the incident photon and the surface plasmon modes are coupled, $k_{sp} = k$. k_{sp} and k are given by Eq.1.23 and Eq.1.24, respectively.

$$k_{sp}(\omega) = \frac{2 \cdot \pi}{\lambda} \cdot \sqrt{\frac{\varepsilon_1 \cdot \varepsilon_2(\omega)}{\varepsilon_1 + \varepsilon_2(\omega)}} \tag{1.23}$$

$$k = \frac{\omega}{c} \cdot \sqrt{\frac{\varepsilon_1 \cdot \varepsilon_2(\omega)}{\varepsilon_1 + \varepsilon_2(\omega)}} \tag{1.24}$$

Where λ is the wavelength of incident light, ε_1 and ε_2 are the relative dielectric function of two materials, ω is the frequency of wave and c is the speed of light.

The equilibrium between k_{sp} and k can be provided by using a prism or rough metal surfaces. A metal film can be illuminated through the dielectric prism at the angle of incidence greater than the angle of total internal reflection. The Kretshmann configuration is presented in Fig.1.15.(b).

The use of prism provides to increase the wavevector of photon in optically dense medium. Hereby, the resonant light tunnels through the metal resulting a coupling between the light and surface polaritons for certain angle of incidence. The Kretshmann configuration has a very good efficiency that can attain to almost 100 % for thin films but it is not favorable for thick films since the increasing film thickness also increases the tunneling distance, consequently the efficiency of SPP excitation drops. For thick films, SPP can be excited in Otto configuration (Fig.1.15.(c)) where the prism is placed above the thick film with a distance. So photon tunneling occurs through the air gap between the prism and metal substrate. Another approach is a diffraction grating on the smooth surface that can also lead coupling between incidence photon and SPP, –presented in Fig.1.15.(d). Using a rough metal surface is enough itself to excite SPP with conventionally light illuminating (Fig.1.15.(d)). When a smooth surface is exposed to light, a portion of incident light adsorbed on the surface and their energy is transformed to heating. But the rough metal surfaces diffract the incident light at different angles resulting a variation in the wavevector of photon. This variation is represented by $\Delta k_{roughness}$ in Eq.1.25. Thus, the coupling is provided on both air-metal and glass-metal interfaces. In this configuration, we observe localized surface plasmons.

$$k = k_{sp}(\omega) \pm a \cdot \frac{2 \cdot \pi}{\alpha} = k_{sp}(\omega) \pm \Delta k_{roughness} \tag{1.25}$$

Where a is an integer, α is the periodicity of the roughness and $\Delta k_{roughness}$ is the total variation of wavevector due to the roughness. $\pm$ denotes the direction of SPs propagation.

As a result of the surface charge and electromagnetic wave interaction, surface plasmons can propagate along the surface and the SPP electromagnetic field decays exponentially from the surface. The length of propagation depends the type of metal and the wavelength of incident light. The perpendicular SPP field is in order of half of wavelength for the metal-air interface but in the metal-glass interface is limited by skin effect [37].

Localized surface plasmons is a particular condition of surface plasmons in which the propagation process is more complicated. In contrast to surface plasmons, the propagation is occurs in short range, order of tens of nanometer. A configuration like in Fig.1.15.(e), a surface covered by metallic particles, can produce localized surface plasmons (LSPs). LSPs excitation depends on geometric features of surface as size of particles and interparticle distance, and also the dielectric constant of metal. Localized surface plasmon goes in resonance in a specific frequency characterized by previous parameters. Localized surface plasmon resonance plays a significant role on the behavior of surface plasmon polariton (SPP) if both LSP and SPP frequency are close each other. Finally, a significant electromagnetic enhancement occurs at metallic particles due to localized surface plasmon excitation. Thus, localized surface plasmon is indispensable to surface enhanced Raman scattering since it has a remarkable electromagnetic exaltation in small volume.

1.2.2 Raman spectroscopy

Chandrasekhara Venkata Raman was the first person who interested in the inelastic light scattering that is the fundamental principle of Raman Spectroscopy [38].

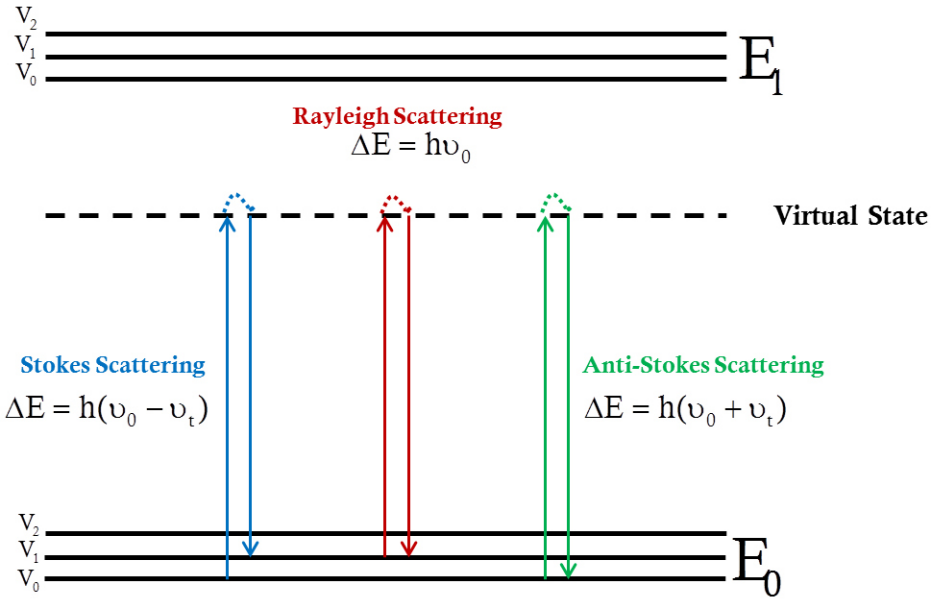

Fig. 1.16: Jablonski energy diagram for Rayleigh and Raman scatterings.

When a beam of light comes through a molecule, it absorbs the energy of incident light. If there is not enough energy to move the electrons of molecule to the excited energy state, the electrons will move to another energy level which called virtual energy state. Since the electrons are not stable at this state, they tend to turn back to their initial state. Mostly, the electrons turn to their initial state with elastic photon scattering as known *Rayleigh scattering*, in which scattered and incident photon have the same energy. Apart from that, there will be also inelastic photon scattering which occurs approximately 1 in every billion photons. In this case, electrons liberate photons to turn their initial state but not to the same vibrational level, it is called as *Raman scattering*. If the electrons move a higher vibrational level than their initial vibrational level, it will be *Stokes Raman scattering* and the opposite case it will be *Anti-Stokes Raman Scattering*. As a result of that, a difference of frequency comes out and it is called *Raman Shift* (cm^{-1}). Raman scattering is not depend on the frequency of incident photons. Raman spectroscopy is a very powerful technique; it can be used for determination of chemical component, the type of chemical bonds and the crystal structure of analyte with very nice spatial resolution.

Figure 1.16 represents quantum illustration for Rayleigh and Raman scattering. But, these scatterings can be also explained by classical physics.

Since light is an electromagnetic wave, its electric field can be given by

$$\overrightarrow{E} = \overrightarrow{E_0} \cdot \cos(2\pi\nu_0 t) \tag{1.26}$$

where ν_0 is frequency of the radiation and t is time. When light interacts with a target molecule, it induces an electric dipole moment that can be expressed by

$$\overrightarrow{\mu} = \alpha \cdot \overrightarrow{E} = \alpha \cdot \overrightarrow{E_0} \cdot \cos(2\pi\nu_0 t) \tag{1.27}$$

where α is molecular polarizability tensor which depends on the conformation of molecule. Besides, it involves the variations originated from the vibration of target molecule.

$$\alpha = \alpha(Q) \tag{1.28}$$

Where Q is the vibration amplitude which corresponds the displacement between the actual position of the molecule and the equilibrium position for a harmonic oscillation. If we consider that the molecules vibrate with a frequency ν_t, Q can be expressed by

$$Q = Q_0 \cos(2\pi\nu_t t) \tag{1.29}$$

On the other hand, Taylor series can be helpful to express polarizability tensor.

$$\alpha = \alpha_0 + [\frac{\partial\alpha}{\partial Q}] \cdot Q + ... \tag{1.30}$$

Where α_0 is the polarizability at equilibrium and produces elastic scattering. Besides, $\frac{\partial\alpha}{\partial Q}$ corresponds to variation of polarizability with respect to Q at this point. This term is the origin of elastic scattering. If we can use Eq.1.30 to develop induced electric dipole (Eq.1.27), the equation becomes

$$\overrightarrow{\mu} = \alpha \cdot \overrightarrow{E_0} \cdot \cos(2\pi\nu_0 t) + [\frac{\partial\alpha}{\partial Q}] \cdot Q_0 \cdot \overrightarrow{E_0} \cdot \cos(2\pi\nu_t t) \cdot \cos(2\pi\nu_0 t) \tag{1.31}$$

Finally, the induced electric dipole moment can given by

$$\overrightarrow{\mu} = \underbrace{\alpha \cdot \overrightarrow{E_0} \cdot \cos(2\pi\nu_0 t)}_{\textbf{Rayleigh Scattering}} + \underbrace{\frac{1}{2} \cdot [\frac{\partial\alpha}{\partial Q}] \cdot Q_0 \cdot \overrightarrow{E_0} \cdot \cos[2\pi(\nu_0 - \nu_t) \cdot t]}_{\textbf{Stokes Scattering}} + \underbrace{\frac{1}{2} \cdot [\frac{\partial\alpha}{\partial Q}] \cdot Q_0 \cdot \overrightarrow{E_0} \cos[2\pi(\nu_0 + \nu_t) \cdot t]}_{\textbf{Anti-Stokes Scattering}} \tag{1.32}$$

The final equation consist of three terms. The first term corresponds Rayleigh scattering whose emitting frequency equals to the frequency of incident light, ν_0. The second and third terms are originated from inelastic scattering and represents Stokes and Anti-Stokes scattering, respectively.

1.2.3 Surface Enhanced Raman Scattering

Raman spectroscopy captured many attentions owing to its abilities in quantitative and qualitative analyses of variety samples such as polymers, chemical compounds, biologic tissues. The invention of laser in 1960 was followed by the development of optical components as CCD (Charge Coupled Detector) and the specialized filters (1980). These advancements influenced positively to Raman spectroscopy and it became popular in '90s. Raman spectroscopy investigations are performed widely for medical and material researches since it is very useful for analyzing samples at all state of matter in small quantity without any special preparation. But this technique is hampered by its low cross-section which causes the low signal intensity and limitations on the detection sensitivity. In 1974, Feischmann et al, used an electrochemically roughed silver electrode to analyze pyridine in order to investigate the role of electrode on the Raman signal intensity [39]. They obtained good signal quality at vibrational bands of pyride. This was the first step at the discovery of *surface-enhanced Raman spectroscopy* (SERS). Three years later, two independent groups concluded that the utilization of the rough silver electrode produces million times stronger signals than the case in which the electrode is absent [40, 41]. The most important disadvantage of Raman spectroscopy, low detection sensitivity, was removed using rough metal surfaces.

1.2.4 Advantages and general features of SERS

Surface-enhanced Raman spectroscopy (SERS) is very powerful analytical tool which has many advantages over other characterization techniques.

Surface-enhanced Raman spectra can be obtained for variety of samples adsorbed on or near the metallic substrates including solid/liquid, solid/gas and solid/solid interfaces. The maximum signal enhancement occurs at the first adsorbed layer onto metallic substrate since the enhancement effect is short-ranged. But also it is possible to have signal exaltation for molecules at the upper adsorbed layer which depends on the morphology of metallic surface and physical environments.

SERS signal intensity depends highly on the morphology and the optical properties of metallic substrate. Gold, silver and copper substrates with submicroscopic structures on the surface result very good enhancement. The atomic scale roughness such as nanoparticles, nanorods, nanowires, adatoms, clusters and atomic steps perform further exaltation.

SERS active surfaces provide to depolarize the Raman bands of target molecule, normally inactivate vibrational modes can be observed in SERS spectra. The selection rules for Raman scattering are not completely valid, they relaxed and that results the appearance of normally forbidden Raman modes in the SERS spectra. Thereby, SERS spectrum contains more Raman bands than classic Raman spectrum.

1.2.5 Enhancement of Raman scattering

Raman scattering is enhanced when the molecules of analyte are in the vicinity of a rough metallic surface. The molecules adsorbed on metal surface result a large scattering cross-section depending on the chemical nature of analyte, its molecular density, the morphology and the type of metallic surface and also the distance between surface and analyte molecules [42].

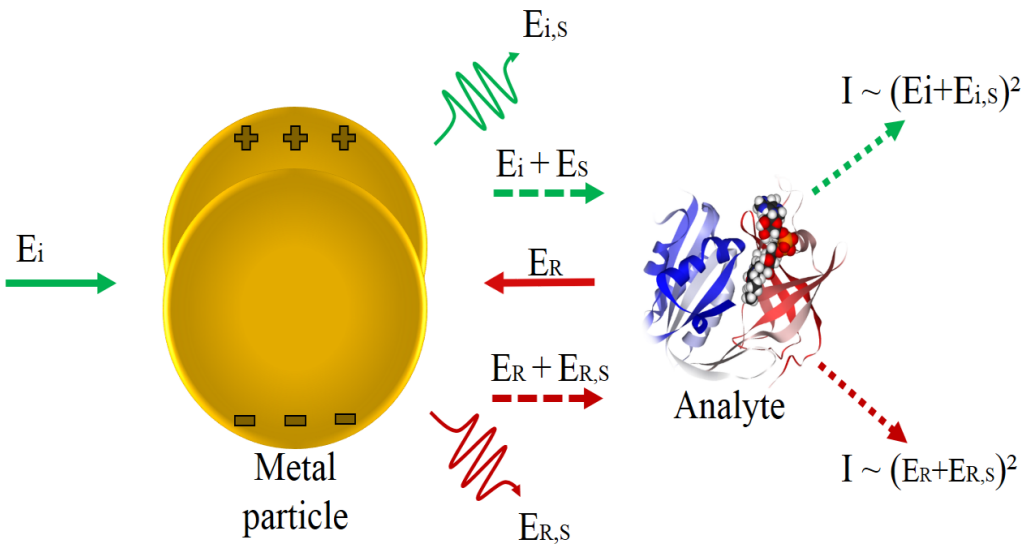

Fig. 1.17: Schematic representation of electromagnetic enhancement mechanism in SERS.

Figure 1.17 represents electromagnetic enhancement mechanism in SERS. The excitation laser beam is an electromagnetic field according to electromagnetic model, E_i, which excites the surface plasmons and induces oscillating dipoles (see Eq.1.27). The scattering occurs only if the plasmons propagates perpendicular to surface. The induced dipoles result a local electromagnetic field on metallic particles. When the incident field reaches to metallic particles, it is magnified by local electromagnetic field, $E_i + E_S$. This magnified field excites the molecules of analyte resulting Raman scattering E_R. The Raman field can also polarizes the metal particle. In fact, the nanoparticles act as an antenna and magnify the scattered Raman field, $E_R + E_{R,S}$. Consequently, scattered Raman signal is enhanced via localized plasmons and the polarization of metallic particles by scattered Raman field. The localized plasmons plays an important role in this enhancement process.

To addition the *electromagnetic* enhancement mechanism described above, there is a *chemical* effect which contributes to the SERS enhancement. The chemical interactions between the metallic surface and analyte molecules originate the chemical effect [43]. A charge transfer or a bond formation strengthen the molecular polarizability which originates the chemical contribution to signal exaltation. The chemical contribution to exaltation is found less than electromagnetic contribution [44, 45]. The contribution of chemical and electromagnetic effects are decoupled [46] as seen from the integrated photon flux at SERS experiment.

$$\phi^{SERS} = \frac{I_I}{\hbar \cdot \omega_1} \cdot \sigma^R \cdot \sum_{i=1}^{N} M_i^{EM} \cdot M_i^{Ch} \tag{1.33}$$

I_I and $(\hbar \cdot \omega_1)$ represent irradiance and energy of incident photon, respectively. σ^R is the temperature and wavelength dependent Raman cross-section. M_i^{EM} and M_i^{Ch} are electromagnetic and chemical parts of enhancement factors, respectively. The calculation consist sum of N molecule for both electromagnetic and chemical enhancement parts.

1.2.6 SERS experiment setup

The localized surface plasmon resonance (LSPR) and surface-enhanced Raman scattering (SERS) measurements were carried out on a home-built microscope. An inverted confocal microscope (Nikon Eclipse Ti-U) was associated with a spectrograph (Shamrock 303, Andor Technology) and a CCD camera (Newton 920, 1024 x 256 pixels, 26 μm, BR-DD, 3 MHz Andor Technology) to procure both absorbance and SERS spectra.

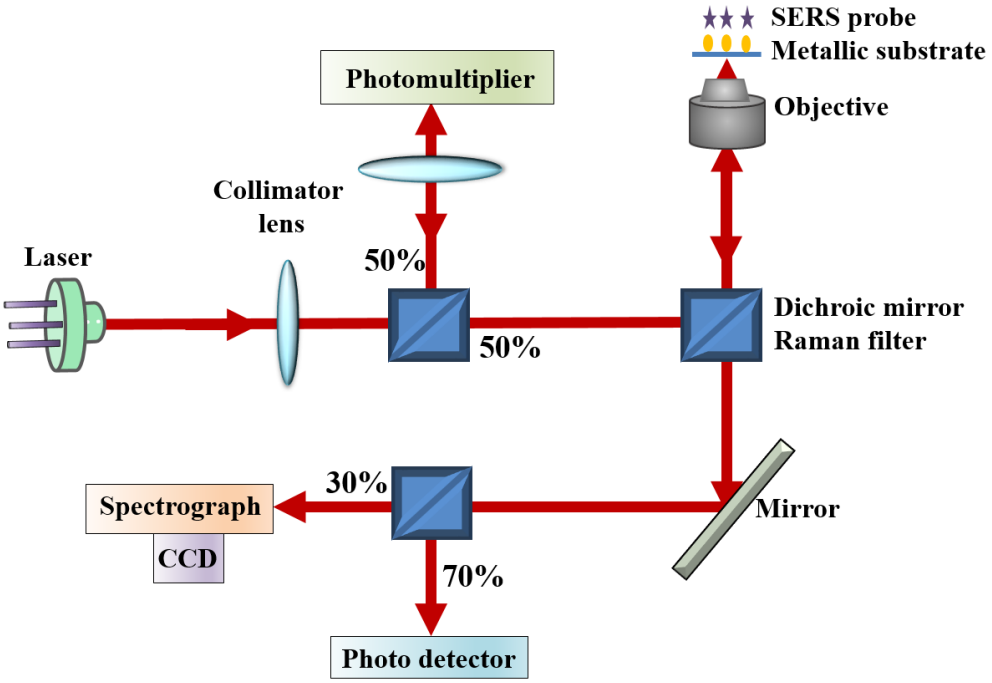

Fig. 1.18: Schematic drawing of SERS setup.

The schematic presentation of our setup is shown in Fig.1.18. Our goal was to detect the adsorption of analyte on nanoparticles (NPs) by absorbance measurements then acquire its chemical signature by SERS anlysis. To achieve this goal, it is necessary to change the light source. The absorbance spectra are recorded under the excitation of a halogen lamp. SERS spectra are obtained via a laser excitation at 785 nm (Micro Laser Systems Inc., France). In both measurements, the light is collected by × 60 objective (Plan Apo VC, N.A :1.2, Nikon).

We post-process all SERS data with a Matlab script to subtract the fluorescent baseline of each spectrum. The parameters for baseline subtraction are chosen after processing all spectra of each sample in order to take into account for baseline variations. The peak positions are estimated from each SERS spectrum for statistical analyses.

1.3 Conclusion

We have presented in detail the principle of atomic force microscopy and surface enhanced Raman spectroscopy in this chapter.

Atomic force microscopy offers topography of sample with an atomic resolution in air or liquid medium. We discussed three operation modes (contact, oscillating contact and Peak force) involving their physical phenomena. We presented conventional AFM, HS-AFM and Dimension FastScan microscopes and their working mechanisms. Conventional AFMs have wide range of varieties in the market. However, in this work we used only Bioscope, Multimode 8 and Dimension 3100 (Bruker). Depending of the size and resolution of image, these microscopes provide to obtain an AFM image in 3 to 10 minutes.

Dimension FastScan microscope was tested by our team during six months. This commercial high-speed atomic force microscopy provides an user-friendly interface to operate microscope with easiness. Microscope Image Registration and Overlay (MIRO) software integrates the AFM images to optical microscopy or any imported images which enable to navigate easily on the sample and collect data on the desired location. This microscope reaches approximatively 10 times faster image acquisition time compared with conventional atomic force microscopes. However, it still remains behind from HS-AFM by considering its scan rates.

If we overview Ando's HS-AFM setup, it is a very sophisticated design which offers to observe real-time dynamics with very short acquisition times (tens of images per seconds). On the other hand, HS-AFM is not a "ready-made" type of microscope, the imaging process involves elaborative preliminary steps such as preparations of the sample stages and fabrication of EBD tips.

More essentially, the operation process of HS-AFM requires an expertise since it is fully manual. However, when all preliminary steps are settled, it provides to achieve the real-time dynamics with very high resolutions. Furthermore, HS-AFM has a flexible design which is convenient for modifications. We will discuss at 4th chapter the coupling of HS-AFM with surface enhanced Raman spectroscopy.

We also introduced the basics of surface enhanced Raman spectroscopy (SERS) in this chapter. Firstly, we have presented the physical phenomena lie on the Raman signal exaltation which is localized plasmon resonance (LSPR). LSPR is a specific case of surface plasmon resonance (SPR) therefore all conditions of SPR are briefly mentioned. The difference between Raman spectroscopy and SERS has been pointed out as well as the advantages of SERS over Raman spectroscopy.

In this work, we have used SERS and AFM to investigate the protein-surface and the cell membrane – virus interactions. The next chapter is dedicated to explain the fabrication procedure and the properties of the used nanoparticle substrates for SERS analyses.

2

Plasmonic Active Nanoparticle Substrates

Raman spectroscopy is a label-free technique for detection and structural analysis of molecular materials. Unfortunately, Raman signals are inherently weak, therefore very few scattered photons are available for the detection. Surface enhanced Raman spectroscopy (SERS) is a useful method in which the weak Raman signals are amplified due to an increment of the Raman cross-section of the analyte. Use of a rough metallic substrate results the local amplification of the electromagnetic field at the proximity of metal nanostructures by the excitation of localized surface plasmon resonances. The crystallinity, shape and separation distance of nanostructures are crucial to support SERS measurements. We will present briefly the most common fabrication procedures of SERS substrates. Afterwards, we will focus our fabrication procedure and the reference samples used to validate the performance of nanocrystalline substrates.

2.1 General features of nanoparticle substrates

A key parameter to take into account in surface enhanced Raman spectroscopy (SERS) experiments is the choice of enhancing substrate. SERS substrates can be roughly classified into three main classes:

- **Metallic electrodes :** Their importance has decreased substantially due to development of substrates with higher amplification power.
- **Metal nanoparticles in solution :** Colloids remain their importance for the plasmonic sensing applications. In colloidal solutions, the nanoparticles are suspended in a liquid media which aid to drive target molecules to the plasmonic surfaces. However, the analyte could be insoluble or incompatible with the liquid media that pose a problem for easy and general applications of colloidal solutions.
- **Nanostructured substrates :** These substrates may be obtained by two main methods: (a) deposition of metal nanoparticles (NPs) from colloidal solutions by drying or evaporation of solvent onto appropriate substrates, or (b) fabrication of nanostructured metal surfaces, taking advantage of micro and nano-fabrication techniques.

Metal nanoparticles (NPs) have promising applications in materials science, communications, biochemistry and medicine due to their optical and topographic features. Gold, silver and copper are widely used in nanoparticle fabrications since their conduction-band electrons can resonate with incident photons. This phenomena is known as *localized surface plasmon resonance (LSPR)*. Localized surface plasmons result the exaltation of the local electromagnetic field that provides to increase the signal strengths and resolution in the field-enhanced spectroscopies such as surface enhanced Raman spectroscopy (SERS) and fluorescence enhanced spectroscopy [47]. In addition, metal NPs provide to control and manipulate of optical signals in nanoscale. Functionalized NPs with specific ligands can be used in the detection of biomolecules.

2.1.1 Synthesis of nanoparticles

2.1.1.1 Bottom – up methods

The main limiting obstacle of Surface Enhanced Raman Spectroscopy (SERS) as an regular laboratory technique is the lack of suitable substrates. Despite the high number of publications and patents where the new active materials are proposed, the commercial substrates are still scarce, often expensive and quite unstable (e.g. requiring a storage in controlled atmosphere and careful handling to maintain their enhancement properties).

The colloidal solutions and the self-assembly techniques constitute the bottom-up methods. The gold colloid solutions have been used from 16th century basically for coloring glass and porcelains. The Lycurgus Cup is a well-known example, made from a glass contains small portion of gold and silver colloidal nanoparticles that generates a dichroic effect. The color of colloid solutions depends on the size of constituting nanoparticles. This principle has been investigated for the first time by Michael Faraday in 1850. In the mid-twentieth century, the discovery of the scanning electron microscopy aid to determine the morphology of nanoparticles in colloidal solutions.

Using the colloidal solutions results large quantity of nanoparticles on the substrate, herewith it enables to cover large substrates. Although, to control the dispersion of nanoparticles over the substrate and achieve a high reproducibility is a challenge. The uniformly sized nanoparticles can be obtained by reduction of gold chloride solution with sodium citrate. An important issue to consider is the concentration of reagents that can influence the average size of nanoparticles and monodispersity. Besides, the variation in the temperature, ionic strength, pH level may cause an aggregation of nanoparticles [48]. Colloidal solutions provide a perfect control on the crystallinity of particles. The nanoparticles can be established in various shapes such as spherical, bipyramidal, square and nanorods [49, 50].

However, there are some approaches to combine top-down and bottom-up methods. For example, the colloidal nanoparticles can be deposited on a substrate after electron-beam lithography (EBL) patterning and surface functionalization [51]. EBL patterning defines the area of nanoparticles, herewith the number of particles in a specific zone. Besides, "Raspberry-Like" gold nanoparticle substrates have been used in our group [52].

Another approach is *nanosphere lithography (NSL)*. The fabrication steps of NSL are presented in Fig.2.1. Firstly, the surface of substrate is coated with polymer spheres and allowed to self-assemble. A metal layer with desired thickness is deposited on the nanospheres. Using the solvents removes the polymer spheres, consequently a metal hexagonally close-packed array remains on the substrate [53, 54].

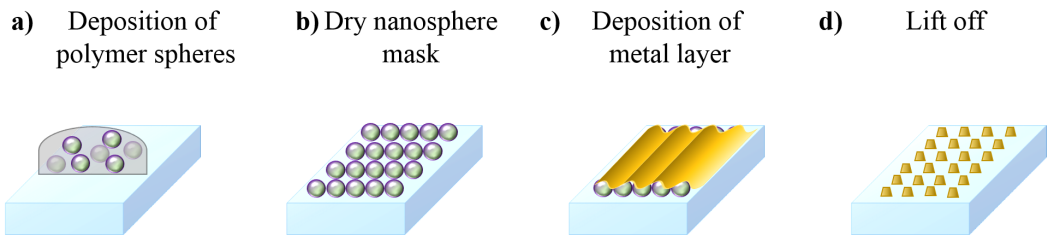

Fig. 2.1: The fabrication steps of nanosphere lithography. (a) Deposition of electron-beam resist, (b) exposition to electron beam and development, (c) deposition of a metal layer and (d) lift off.

Film-over-nanosphere (FON) is metallic substrate fabrication procedure which is commonly used for SERS and LSPR experiments [55]. The fabrication procedure, that is very similar to NSL, involves coating the substrate with the nanospheres and deposition of a metal layer. Fig.2.1.(a)–(c) demonstrates the fabrication steps of FON substrates.

2.1.1.2 Top – down methods

The top-down fabrication methods include microfabrication procedures performed under vacuum. *Electron-beam-lithography* (EBL) is the most commonly used nanoparticle fabrication technique among the top-down methods. This technique provides patterning on a defined area of the surface with various shapes of nanostructures. For example, the nanocylinders [56], nanowires [57], square [58] and triangular [59] shaped nanostructures have been established. Some nanostructures fabricated by EBL in our laboratory are presented in Fig.2.2.

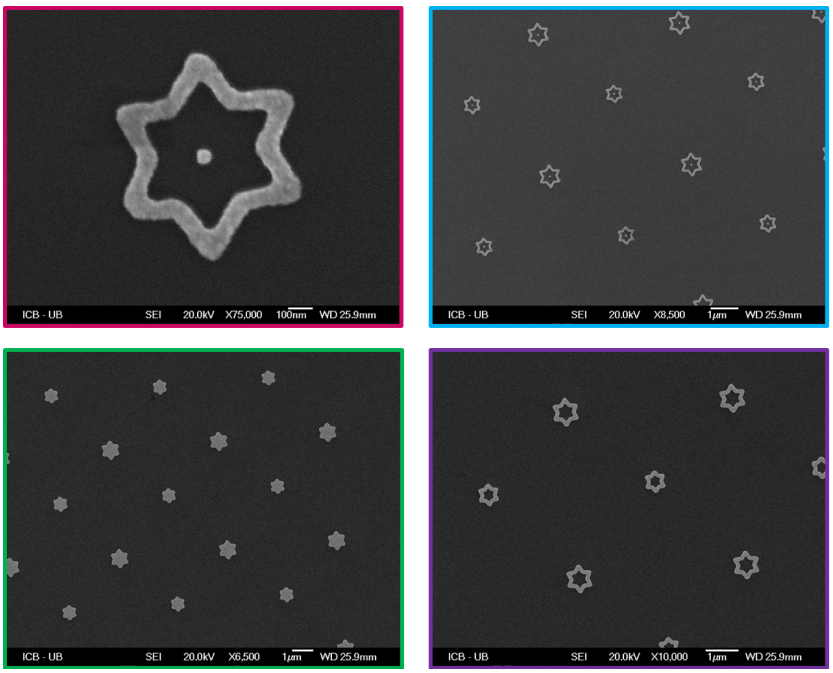

Fig. 2.2: Nanostructures fabricated by EBL at ICB laboratory.

In the last decade, it has become possible to design and built an increasing number of nanoscaled metallic structures, ranging from nanodots to three dimensional scaffolds, with potential applications as SERS analyses. Particularly, the shape, size and spatial distribution of the nanostructures are well controlled by lithographic or direct writing techniques. Therefore, these techniques are commonly used even though the expense of production process that is high due to the cost of machines, materials, masks and time of fabrication. Their low throughput of conventional techniques is strongly limiting their diffusion.

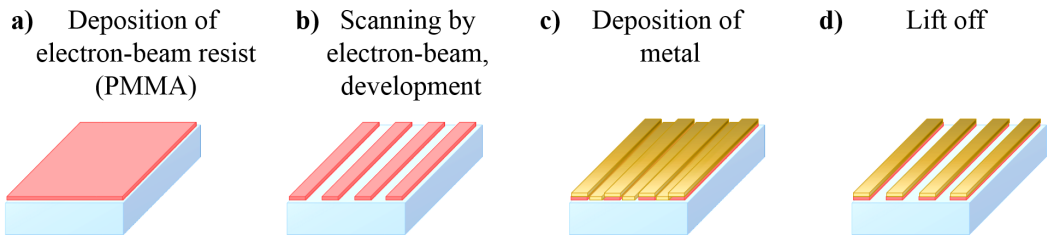

Fig. 2.3: The fabrication steps of electron-beam lithography for manufacturing nanostructures. (a) Deposition of electron-beam resist, (b) exposition to electron beam and development, (c) deposition of a metal layer and (d) lift off.

The fabrication of nanostructures by electron-beam lithography consists of several steps as shown in Fig.2.3. First, an electron-beam resists is deposited on the substrate. The surface of resist is scanned by a focused electron beam in order to obtain desired form of nanostructures. This followed by development that removes the exposed portion of resist. A metal layer is deposited on the substrate and applied to lift off process. A solvent dissolves the remaining resist resulting the presence of only patterned structures on the substrate.

Electron-beam lithography enables to fabricate metal dimers and to control the gap distance [60]. However, it is highly challenging to achieve small structures ($\phi <$ 20 nm) and short interparticle spacing ($\sim$ 10 nm). The nanostructures fabricated by electron-beam lithography are flat and don't posses any sharp edges. It is know that the features with short interparticle spacing and sharp corners enhance the plasmon coupling effect [61, 62]. Thus, that can be considered a disadvantage for plasmonic sensing applications.

Another approach belongs to top-down methods is *evaporation based depositions*. The sputtering, electron gun and thermal evaporation can be listed under this category. *The thermal evaporation* is used widely to deposit a metal layer after electron-beam lithography process (e.g., Fig.2.3.(c)) and also for achieving a nanoparticle substrate.The thermal annealing technique is a time saving method, especially compared with electron-beam lithography or other sophisticated methods. Besides, thermal annealing technique can address to surfaces of a few cm^2 range although that is limited to hundreds of μm^2 for electron-beam lithography.

Table 2.1. summarizes nanoparticle fabrication methods and their advantages.

Tab. 2.1: Nanoparticle fabrications methods.

Methods	**Advantages**	**Disadvantages**
EBL	Variety of shape	Limitation interparticle Spacing, time-consuming
Ther. Evap.	Easiness and interparticle spacing	Limited shapes
Colloids	Controlled crystallinity and variety of shape	Distribution over the surface
NSL	Specific patterning	Limited shapes
FON	Easiness	Limited shapes

We used the thermal evaporation technique in this work to fabricate the nanoparticle covered substrates. This technique is attractive since it enables to cover large areas by using an unsophisticated fabrication process. However, they are often hindered by the limited control of the size, shape and distribution of nanoparticles, which do not contribute to reproducible measurements. We have developed a novel fabrication process to avoid these inconvenient.

2.1.2 The fabrication procedure of plasmonic – active SERS substrates

Substrates constituted of arrangement of metal nanoparticles are crucial in the development of chemical and biological sensors [63, 64, 65, 66, 67, 68] based on surface plasmon resonance (SPR) or Surface-Enhanced Raman Scattering (SERS) [69, 70]. A surface roughness on the nanometer length scale is a key element for a Raman signal exaltation [41, 40] and consequently nanoparticle-covered surfaces have captured much attention for producing reliable sensing platforms. The intensity of the Raman signal depends highly on the optical properties of the metal surface and localized surface plasmon resonances (LSPR) are an important parameter to consider for achieving large enhancements [71, 72, 73, 74].

The LSPR wavelength sensitively depends on the size, shape, coupling distance and constitutive material of the nanoparticles [73, 74, 75, 62]. It is crucial to control the nanoparticle geometry and the surface coverage for optimum sensing capabilities. Therefore, we have fabricated various substrates including silver, gold and bimetallic silver-gold nanoparticles at different geometries on a glass substrates and we investigated their LSPR wavelength and SERS performance. We have used two protocols, called "GDC" and "non-GDC", in order to modify the topographic and mechanic features of substrates. The fabrication details for both protocols are listed in Tab.2.2.

Tab. 2.2: The fabrication steps of non-GDC and GDC nanoparticle substrates.

	Non - GDC	**GDC**
Substrate	Glass	Glass
Pre-treatment	No pre-treatment	Glow Discharge Cleaning at 2.8×10^{-2} Torr during 1 hr
Metal deposition	Physical Vapor Deposition	Pre-heating of substrate at 450 ℃ Physical Vapor Deposition
Annealing	450 ℃ during 1 h	No annealing

Regardless of the type of the fabrication protocol, the glass substrates are thoroughly cleaned with trichloroethylene. The gold crystalline nanoparticles are fabricated by the following protocols.

2.1.2.1 Conventional physical vapor deposition method (non-GDC)

The metallic nanoparticle substrates were produced via a conventional thermal annealing method. Gold amorphous film was deposited on a cleaned slide by the physical vapor deposition method (PLASYS MEP300). All thermal depositions were carried out when the pressure in the chamber was 2×10^{-7} Torr. Gold was evaporated at a constant rate of 0.05 nm/s from a resistively heated tungsten boat.

The sample was rotated during the evaporation to achieve a homogeneous deposition. We investigated film thickness ranging from 2 to 10 nm. After the deposition of the film, the substrates were annealed at 450 ℃ for 1 hour to form crystalline nanoparticles.

2.1.2.2 Physical vapor deposition method with glow discharge cleaning (GDC)

For this fabrication process, we added an intermediate preparation step just after the chemical cleaning of substrate. The cleaned substrates were exposed to a *Glow Discharge Cleaning* at 2.8×10^{-2} Torr during one hour. After the glow discharge cleaning process, the substrates were heated at 450 ℃ in vacuum chamber when the pressure was 2×10^{-7} Torr. The evaporated gold forms crystalline nanoparticles on the surface in presence of the substrate heating. The parameters used for metal deposition was kept constant for both GDC and non-GDC fabrications.

The substrates, before and after LSPR or SERS measurements, were imaged by scanning electron microscopy using an operating voltage of 20 kV (SEM, JEOL 6500 and JEOL 7500-F).

2.1.2.3 The difference between GDC and non-GDC protocols

The difference between GDC and non-GDC protocols is came from the glow discharge cleaning and the surface heating.

The main difficulty for forming gold nanoparticles by an annealing process is the non-homogeneity of the resulting particles. The reason is related to the wettability of the glass resulting in a low-adhesion of the gold film on the surface as well as the non-uniformity of the nanoparticles during annealing. To improve the surface wettability, we developed an in-situ pre-treatment of the surface that involves use of glow discharge cleaning at pressure of 2.8×10^{-2} Torr during one hour. Glow discharge cleaning dissociates the water molecules forming OH radicals and H atomes [76, 77]. The OH radicals remain on the surface in the strongly bound state and only the hydrogen molecules are desorbed to the gas phase and pumped out of the chamber.

The uniform presence of OH radicals confers i) better adhesion to the gold on the surface, ii) an uniform distribution of nanoparticules during the annealing process and iii) a better mechanical stability of these nanoparticules. We analyzed both GDC and non-GDC substrates by SEM and HS-AFM microscopies.

We used a heating process during the metal deposition to change the morphology of the substrates. Our aim is to achieve a homogeneous coverage of uniformly sized nanoparticles on the substrate. Figure 2.4 presents the comparative SEM images obtained from the different substrate processing.

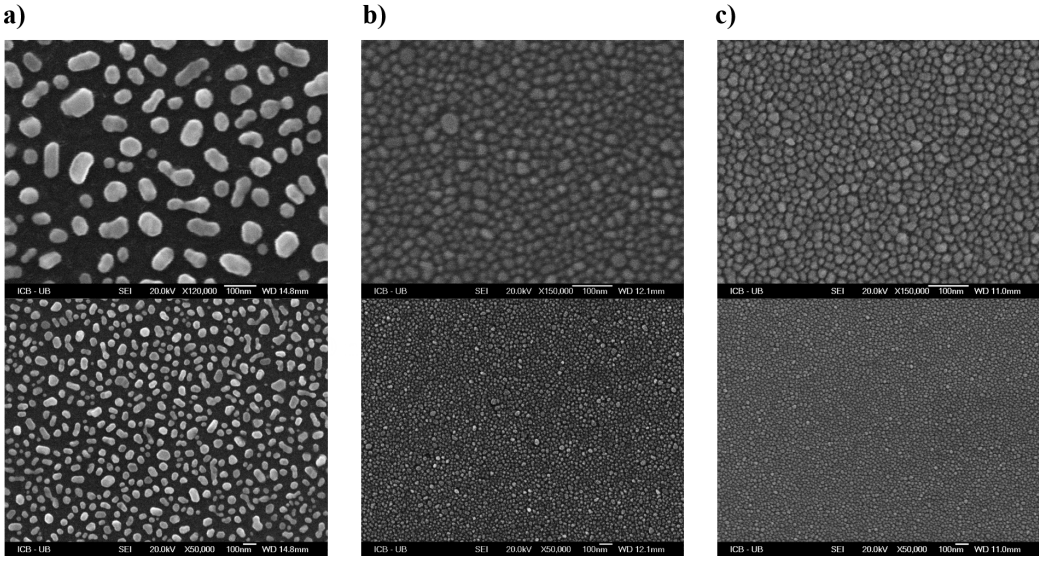

Fig. 2.4: SEM images of Au nanoparticle substrates fabricated by (a) non-GDC protocol and (b) evaporation of Au in the presence of pre-heating (450 °C). (c) GDC protocol; the glass substrate is cleaned by GDC method and Au evaporated in the presence of pre-heating (450 °C).

In Figure 2.4.(a), the image presents result of a conventional annealing method –non-GDC protocol. For Fig.2.4.(b), gold was evaporated onto glass substrate in the presence of a Peltier for heating at 450 ℃. The image of Fig.2.4.(c) is obtained from GDC protocol where a glow discharge cleaning is performed prior to the evaporation of gold in the presence of surface heating. These results clearly show that the heating of surface during the metal deposition has a drastic impact on the morphology of nanoparticles and the interparticle distance.

However, GDC process provides a better particle uniformity and interparticle distribution compared to merely heated substrates. GDC process increases the surface adhesion, which in turns, narrows down the size distribution of the nanoparticles.

2.1.3 Mechanic stability of nanoparticles

The unique advantage of high–speed atomic force microscopy is the real-time observation of topography at nanometric scale. Here, we have used this technique to evaluate the mechanical stability of nanoparticles. The two type of gold nanoparticle substrates described above are implemented to HS-AFM analyses in liquid medium.

The HS-AFM experiment consists several preparation steps that are essential for achieving successive images. These initial steps will be pointed out briefly.

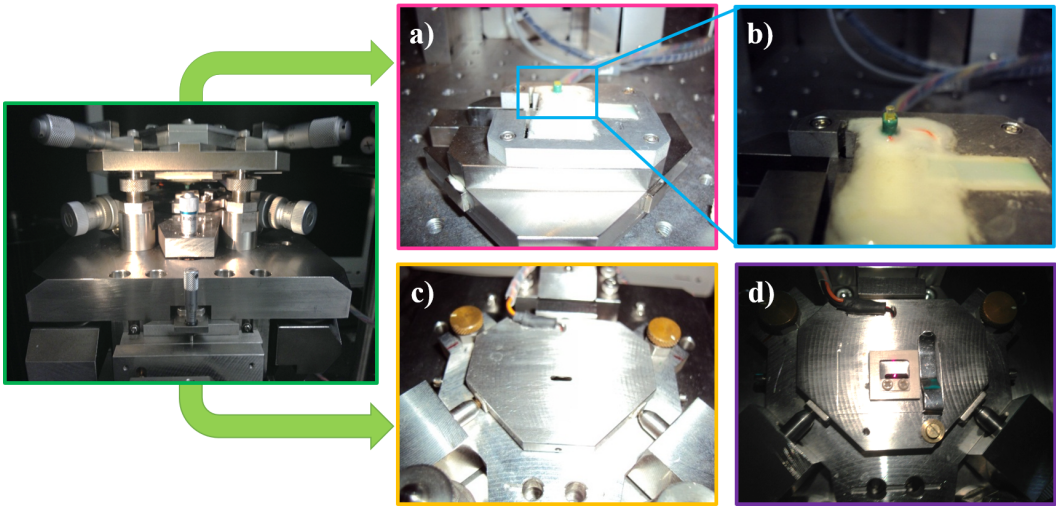

Fig. 2.5: HS-AFM head. (a) Scanner, (b) focus on scanner and the glass rod, (c) the split and (d) the liquid cell.

- **HS-AFM tips :** Sharp EBD tips were fabricated on ultra-short cantilevers (Olympus BL-AC10DS-A2) prior to analyses. The fabrication procedure of EBD tips was described in previous chapter.
- **Cleaning :** The liquid cell of HS-AFM was cleaned with a detergent (DECON 2%) and disinfected by ethanol (70 %).

The liquid cell rinsed off with pure bi-distillated water (PURELAB UHQ II, ELGA), then dried under nitrogen flow.

- **Sample :** Each gold nanoparticle substrate was pasted on the top of glass rod (sample stage) by an epoxy glue. Ultimately, the sample-attached glass rod was fixed on the Z-piezo of HS-AFM by transparent nail polish (Fig.2.5.(b)).

After the preparation steps, an ultra-short cantilever with EBD tip was placed into the liquid cell (Fig.2.5.(c)). Here, we compare the GDC substrate with the in-situ heated non–GDC substrate in order to evaluate the contribution of glow discharge cleaning to the mechanical stability of nanoparticles. Two types of gold nanoparticle substrates were analyzed by HS-AFM in the same experimental conditions. The topography of substrates achieved in phosphate buffered saline (PBS) solution. PBS tablets are purchased from Sigma-Aldrich (pH 7.2 – 7.6). AFM analyses were carried out at controlled atmosphere. The temperature was maintained at 20 ℃ for both FastScan AFM and HS-AFM experiments. The high-speed atomic force microscopy images of these two of substrates are presented in Fig.2.6.

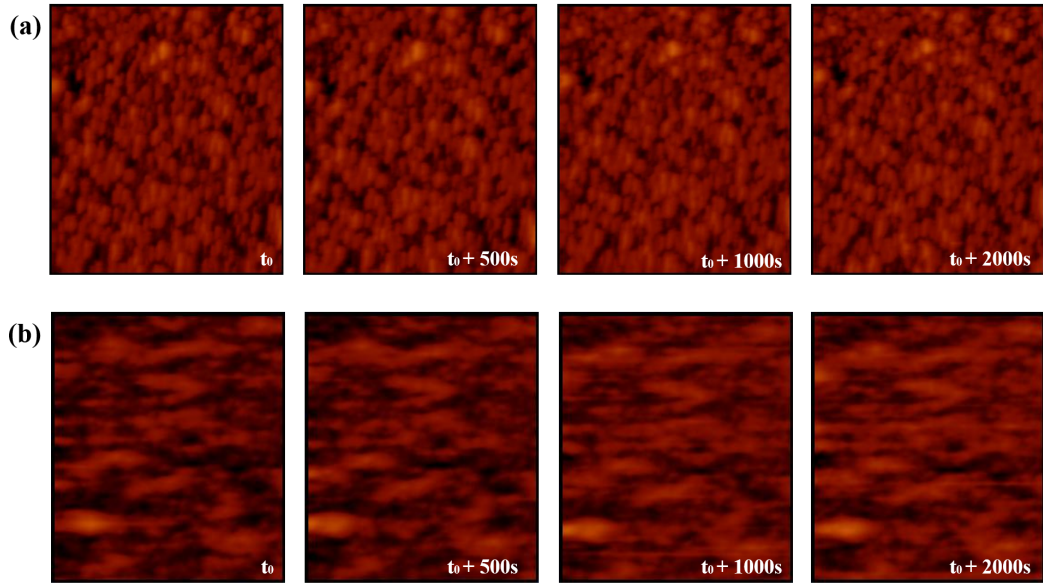

Fig. 2.6: Successive HS-AFM images of the gold nanoparticle substrates obtained in PBS medium with 1 image/s scan rate. All images are in 300 nm × 300 nm and 400 × 400 pixel. (a) GDC substrate. (b) Thermal evaporated substrate in the presence of pre-heating at 450 ℃.

The successive images were acquired by scanning 300 nm^2 area of the substrate during 2000 s. All the frames were obtained with a scan rate of 1 image /s. We present the time lapse of the topography of GDC substrate (a) and in-situ heated non–GDC substrate (b). The difference of stability between the two substrates is striking. The adhesion of nanoparticles on the non–GDC substrate is weak and diffusion of nanoparticles is readily observed. From this high-speed AFM study, we have conclude that glow discharge cleaning prior to gold evaporation improves the mechanical stability of nanoparticles on the glass substrate.

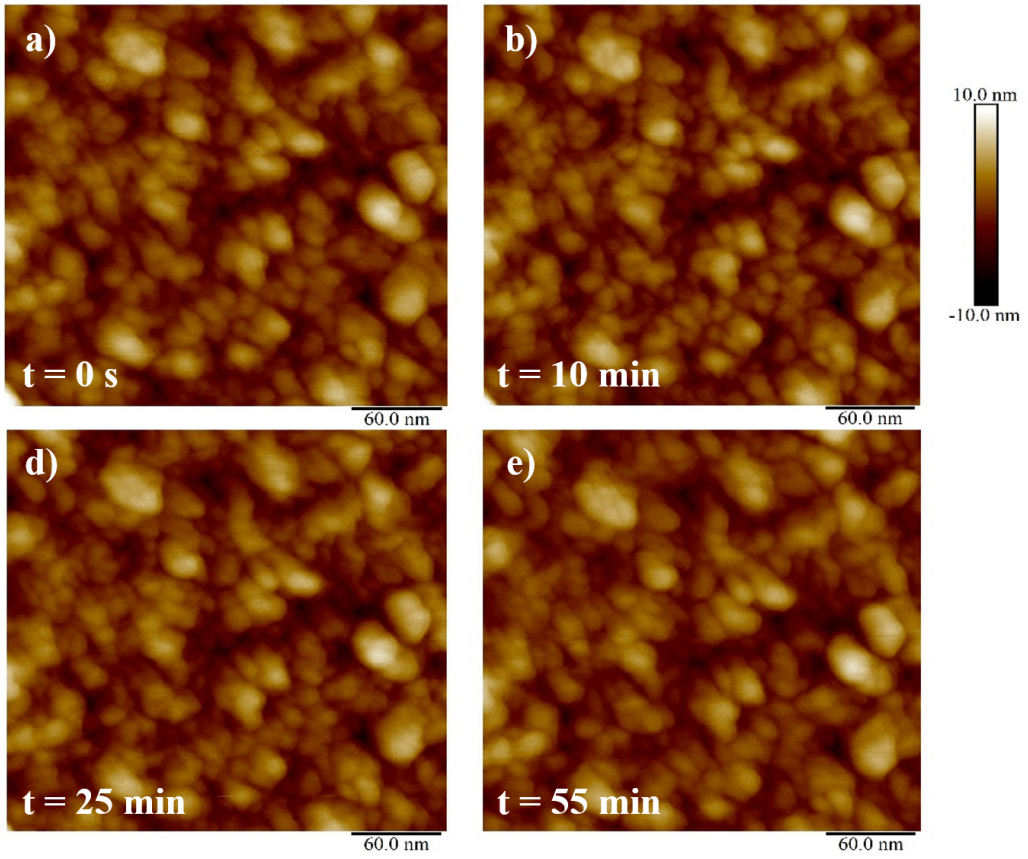

Fig. 2.7: Au nanoparticle substrates are imaged in PBS to observe mechanical stability of the nanoparticles on the glass substrate aganist to time.

We analyzed 300 × 300 nm^2 of GDC nanoparticle substrate by Dimension FastScan AFM microscope using FASTSCAN-D probe (k = 0.25 N/m - F = 110 kHz, Bruker) with 22.3 Hz scan rate during 55 minutes. The AFM images are presented in Fig.2.7.

The results showed that there is not any deformation on the substrate caused by tip induced forces.

2.1.4 Crystallinity of nanoparticles

We examined the crystal quality of gold nanoparticle substrates by X-Ray diffraction (XRD). The XRD 2θ patterns were obtained by using an X-Ray position sensitive detector (CPS 120, Inel) with Cu K_α radiation from a fixed anode at 40 kV, 40 mA. Data were collected within the range $0 < 2\theta < 115°$ with a 0.03° step size and a 1 s step time.

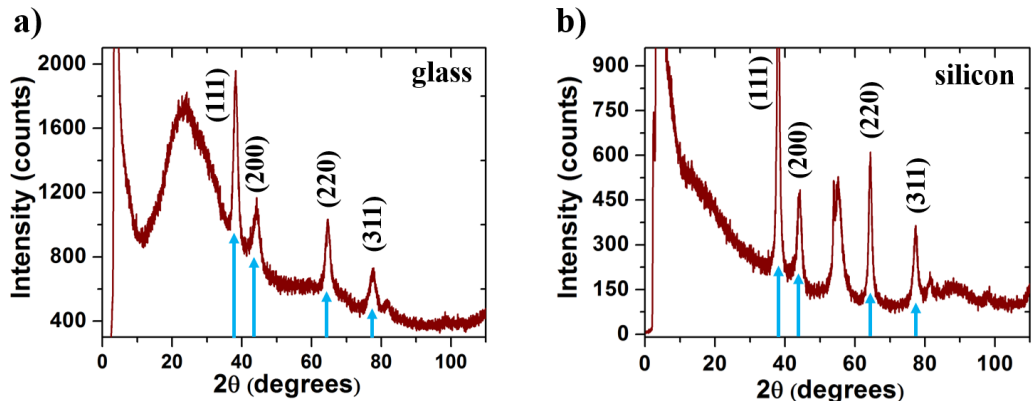

Fig. 2.8: XRD results of Au nanoparticles on (a) glass and (b) silicon substrates.

The XRD patterns of gold nanoparticles on both glass and silicon substrates are shown in Fig.2.8.(a) and (b). The observed 2θ values are 38°, 44°, 64° and 77°, they are marked with arrows on the graph. The edge lengths (a = b = c) and interaxial angles ($\alpha = \beta = \gamma = 90°$) of crystalline structure were found equivalent. According to this result, we assume that the substrates are constituted of crystalline gold nanoparticles with face centered cubic lattice. The space group of the crystalline is Fm3m, known as the Rock-salt structure. Furthermore, the crystallinity of nanoparticles is independent of the substrate.

2.1.5 Geometric features and homogeneity of nanoparticle substrates

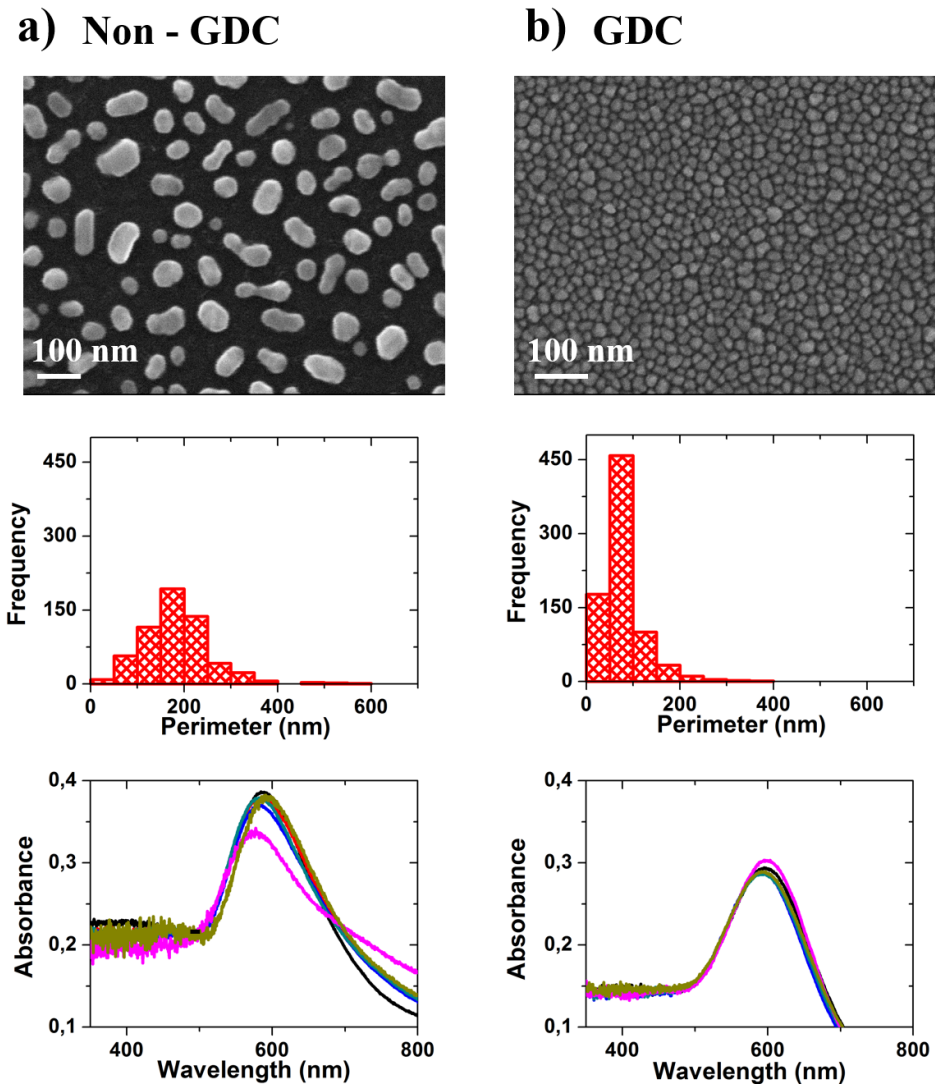

Fig. 2.9: SEM images of a substrate obtained without (a) and with (b) glow discharge cleaning. The corresponding perimeter histograms and absorbance spectra are shown below the SEM images. The absorbance spectra were taken at 6 different locations on the substrate surface.

We have investigated the morphological features of non-GDC and GDC substrates [78]. We have performed a statistical analysis on the SEM images to determine the size distribution of the nanoparticles.

For this purpose, a Matlab script using the Otsu method [79] was implemented for identification of the nanoparticles on surface.

Figure 2.9 shows SEM images of the two fabrications as well as the perimeter histogram of the formed nanoparticles. Post-annealing of an evaporated gold film usually results to a wide distribution of nanoparticle geometry. The poor affinity between the glass surface and the gold causes a low-adhesion of the film which recesses inhomogeneously during the heat treatment. Figure 2.9.(a) shows a characteristic scanning electron micrograph of the large variety of shapes produced, including spherical forms, nanorods and pentagon-like geometries. The average perimeter (P) of the nanoparticles is found at P=180 $\pm$ 15 nm for the non-GDC substrate. Figure 2.9.(b) displays a micrograph of the resulting surface morphology after the GDC process. There is a clear improvement of the nanoparticle homogeneity with almost uniform sizes and forms. The perimeter histogram features a narrower distribution compared to non-GDC substrate with a center at 70 nm. We finally note that the interparticle distance for GDC substrate ranges between 1 nm to 3 nm on the entire substrate thus enabling optimum near-field coupling.

In the following, we have investigated the plasmonic response of the substrates by measuring their absorbance spectra at 6 different locations in order to analyze the homogeneity and reproducibility. The measurements for respective substrates are reported at the bottom of Fig. 2.9. A marked resonance is visible for both types of substrates. Despite a smaller nanoparticle size for the GDC substrate, we have observed a residual redshift compared to non-GDC substrate (from 587 nm to 593 nm). This shift probably originates from the small interparticle distance and the associated increased coupling. The six spectral resonances for the GDC substrate were constant to about 3 nm regardless of the observation position. These results confirm the high homogeneity of the GDC substrates over the entire surface, in agreement with SEM images.

Here, we examined only GDC Au nanoparticle substrate by Dimension FastScan. The analyses were carried out in the same experimental conditions with HS-AFM experiments. The AFM images of GDC substrate are given in Fig.2.10.

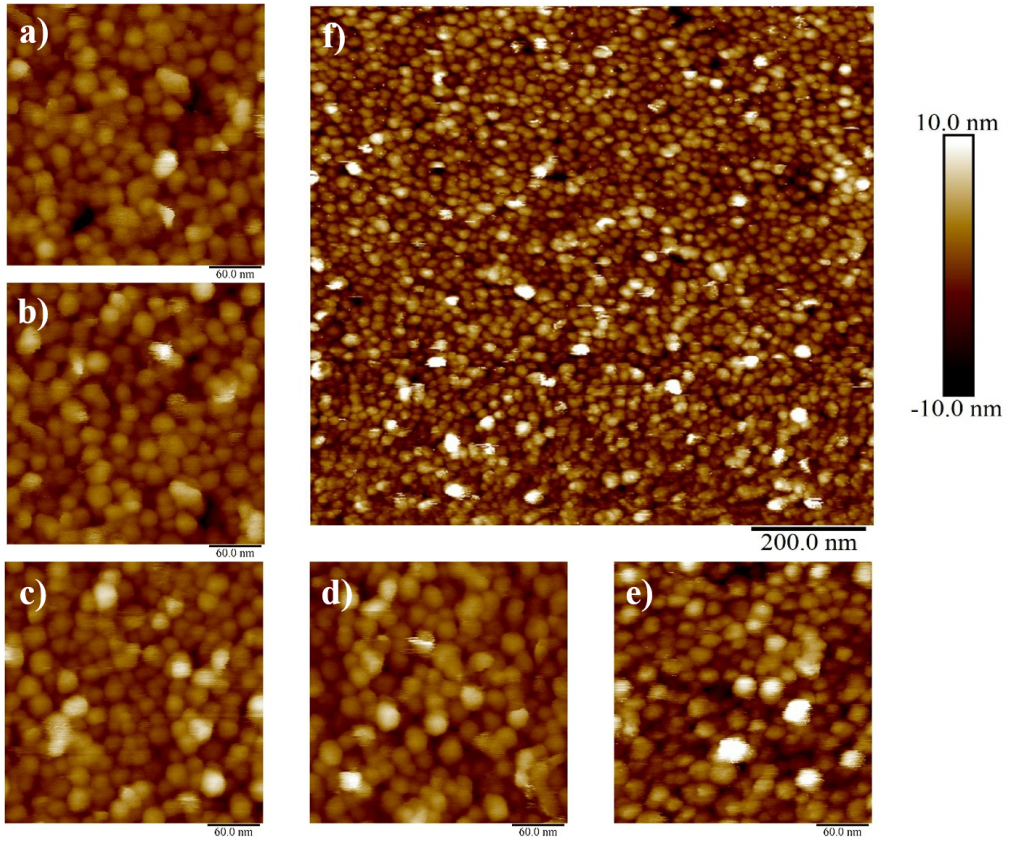

Fig. 2.10: AFM images of GDC Au nanoparticle substrate. (a) to (d) are 300 nm scaled images of different zones on the substrate obtained by : scan rate = 1.95 Hz, amplitude = 250 mV and drive amplitude = 740 mV. Another GDC Au nanoparticle substrate is presented in (e) and (f) at 300 nm and 1 μm scan size. Scan rate is 3.92 Hz for (e) and 1.95 Hz for (f). The amplitude = 136 mV and drive amplitude = 477.3 mV are equal for both images.

Several areas on the GDC Au nanoparticle substrates are presented in Fig.2.10.(a)–(f). These results indicates that GDC substrates are originated from the homogeneous distribution of uniform nanoparticles all over the surface. The size of particles found in conventional AFM images are a few nanometer larger than HS-AFM results that can be explain by the effect of convolution induced by AFM probe. We used a specialized commercial probe for high speed scanning of biological samples (FASTSCAN-D, Bruker). The convolution effect of these probes are larger because of the pyramid shape of tip although EBD tips has a needle form.

2.2 Validation of SERS substrates

Proteins, membranes, and viruses are complex and the dynamic of their structures has not been clearly analyzed by Atomic Force Microscopy (AFM) and SERS. Besides, there is a lack of knowledge of the SERS literature, the SERS signature of all biomolecules has not been investigated. To demonstrate the efficacy of our nanoparticles substrates, we used well-known molecules: *Methylene blue (MB)* and *bipyridine ethylene (BPE)*.

We did not demonstrate a new concept of calibrating surface enhanced Raman scattering (SERS) intensities. We have used for all experiments two different laser power (1 mW or HS-AFM laser diode power set at 0.3 mW). We have used the same analyte concentration to improve the comparability, reproducibility and repeatability of our analysis. Two samples have been used for validation of our experimental setup. Our aim was to study protein – surface interactions (isolated free molecules) and cell membrane – virus interactions (linked molecule on diffuse bilayer) via surface enhanced Raman spectroscopy (SERS) measurements.

2.2.1 Bipyridine ethylene

The theoretical and experimental vibrational assignments of Trans-1,2-bis(4-pyridyl) ethylene have been already studied [80]. Bipyridine ethylene has been used for testing the performance of colloids [81, 82], nanorods [83, 84] and nanostructured substrates [85, 86, 87] on Raman signal exaltation. The fact that it has been studied widely in the literature approve that bipyridine ethylene could be consider as a reference sample in order to validate our experimental procedure.

Trans-1,2-bis(4-pyridyl)ethylene is a chemical compound with chemical formula $C_{12}H_{12}N_2$. Besides, it is known that it yields a large signal intensity at SERS spectrum when analyzed on gold substrates [85].

In this part, we have used *trans*-1,2-bis(4-pyridyl)ethylene (BPE) to examine the efficacy of our SERS substrate.

The surface enhanced Raman spectroscopy and absorbance spectrum measurements, for only this work, were performed at LNIO / UTT in collaboration with Prof. P.-M. Adam and J.-L. Bijeon.

The absorbance measurements were carried out on a home-built setup. The sample was illuminated with UV-Vis light (OCEN Optics DH2000-BAL) using multimode fiber. The diameter of spot was 300 μm on the sample. The light focused on the sample and collected back from the substrate via objectives (Opto Photonics Mitutoyo M plan Apo fluo SL, $\times$20, N.A.=0.28 and $\times$10, N.A.=0.23).

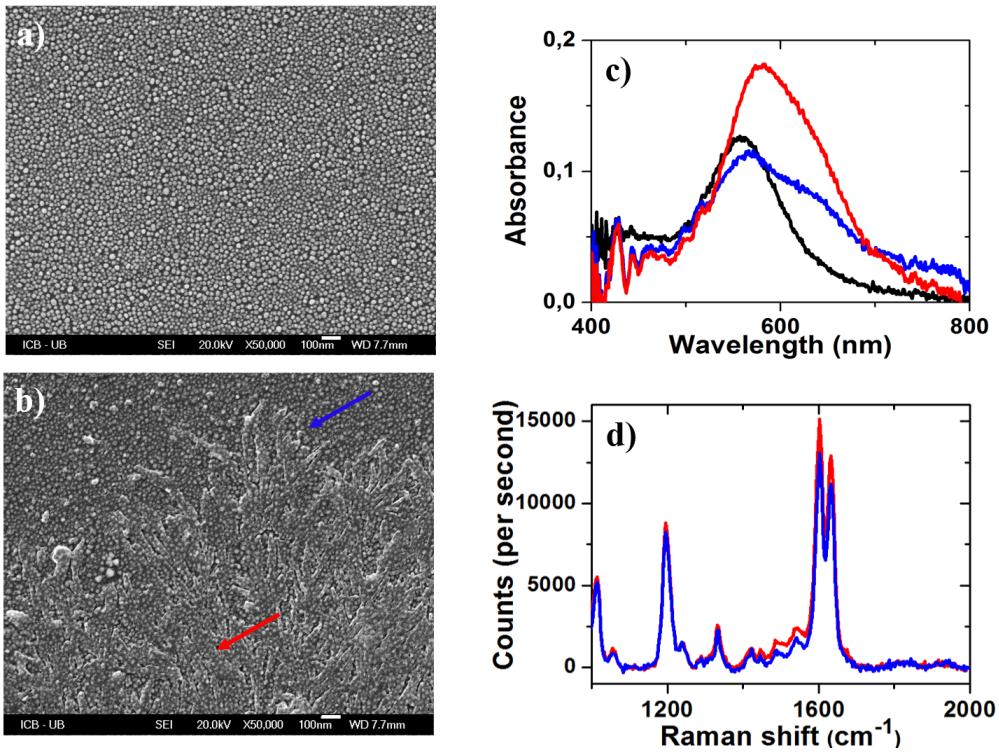

Fig. 2.11: SEM images of Au nanoparticle substrate (a) before and (b) after BPE deposition (50 μl, 10^{-5} M). (c) Absorbance spectrum of Au nanoparticle substrate (black line) and BPE at the edge (blue line) and in the center (red line) of droplet. (d) SERS spectra of BPE collected from at the edge (blue line) and in the center (red line) of BPE droplet.

The bipyridine ethylene (BPE) droplet (50 μl) at 10^{-5} M concentration was deposed on SERS substrate followed by incubation under a chemical hood during 1 hour. The substrate with BPE droplet was blown with nitrogen.

SEM images of Au nanoparticle substrate (a) before and (b) after BPE deposition are shown in Fig.2.11. The absorbance spectra are displayed in Fig.2.11.(c). The gold substrate is presented with black line in the figure and it exhibit a maximum at 560 nm. The red and blue lines correspond to the absorbance spectra of BPE in the center and at the edge of droplet, respectively. As seen from SEM image (Fig.2.11.(b)), the center of droplet contains more molecules than edge that results higher optical density and larger shift at absorbance spectrum.

The SERS spectra were recorded by a spectrograph (Horiba) under 632.8 nm excitation laser light. The scattered Raman light collected via 10× air objective. The acquisition time was 1 s per spectrum. Accordingly with the absorbance results, the Raman signal obtained from the center of BPE droplet is found more intense. The following peaks were achieved for both spectra; 1011, 1060, 1195, 1237, 1332, 1421, 1495, 1542, 1601 and 1633 cm^{-1}. We found a good agreement with literature [80].

2.2.2 Methylene blue

Methylene blue (MB) is a chemical compound that has many applications in different fields such as biology, chemistry and medicine. It was involved in the treatment of malaria and some cancer.

We have used methylene blue molecules as a reference sample to test efficacy of our SERS substrates [78]. For example, Au ring arrays [88], Au sputtered substrates [89], cap shaped Ag nanoparticles [90], borohydride-reduced Ag colloids [91] and Ag nanoparticles deposited on anodic aluminum oxide templates [92, 93] were implemented for methylene blue analyses.

Methylene blue is in solid state at room temperature (22 ℃) in the form of dark green powder. Methylene blue is applied generally in liquid state for LSPR and SERS experiments. When methylene blue dissolves in water, it becomes a blue solution. MB has ring structures constituted by different elements. It is a heterocyclic chemical compound with chemical formula $C_{16}H_{18}N_3SCl$.

Methylene blue could be either in monomer or dimer form depending on the analyte concentration.

UV-vis absorption spectrum of methylene blue shows that two peaks are detected in the red-region, at 612 and 664 nm [89]. However, the monomers have an absorption peak at 662 nm whereas the dimers have an absorption peak at 610 nm [94].

Methylene blue (MB) molecules are non-resonant at the used excitation laser light in our experiment (785 nm), since their absorption spectrum is not in the same wavelength range [89, 95]. The efficacy of our nanoparticle substrates on SERS experiment was investigated by using different SERS substrates. We used several nanoparticle substrates constituted by different metals as well as at different geometries. Additionally, the sensitivity of the SERS substrate is examined with MB at various concentrations (from 10^{-6} to 10^{-15} M).

2.2.2.1 Choice of SERS substrate

The aim of this study is investigate the impact of nanoparticle geometry as well as their components on the SERS signal intensity. For this purpose, we have fabricated six different batches of SERS substrates from gold, silver and bimetallic silver-gold nanoparticles at different particle sizes. Both GDC and non-GDC protocols are used in order to procure these substrates.

First two substrates, named (a) and (b), corresponds to the typical gold nanoparticle substrates fabricated by non-GDC and GDC protocols, respectively. The rest of the substrates are produced by modifying GDC and non-GDC protocol in order to vary the optical and morphological features of the substrates.

Third substrate named (c), is fabricated using the GDC protocol. Firstly, a thin silica film with 20 nm thickness was deposited on the glass substrate. Then, the crystalline gold nanoparticles were formed on the silica layer. Substrate (d) consists of the gold nanoparticles which are suspended from the glass substrate via silica pillars. To do that, the gold nanoparticles are evaporated on the silica layer, as described for substrate (c). This step was followed by a reactive ion etching (RIE) of the substrate in order to etch the silica located between the nanoparticles. The crystalline Au nanoparticles acts as a physical mask. The etching was performed with 5 cc of SF_6 gas at 30 Watt under the pressure of 7.2×10^{-3} mbar.

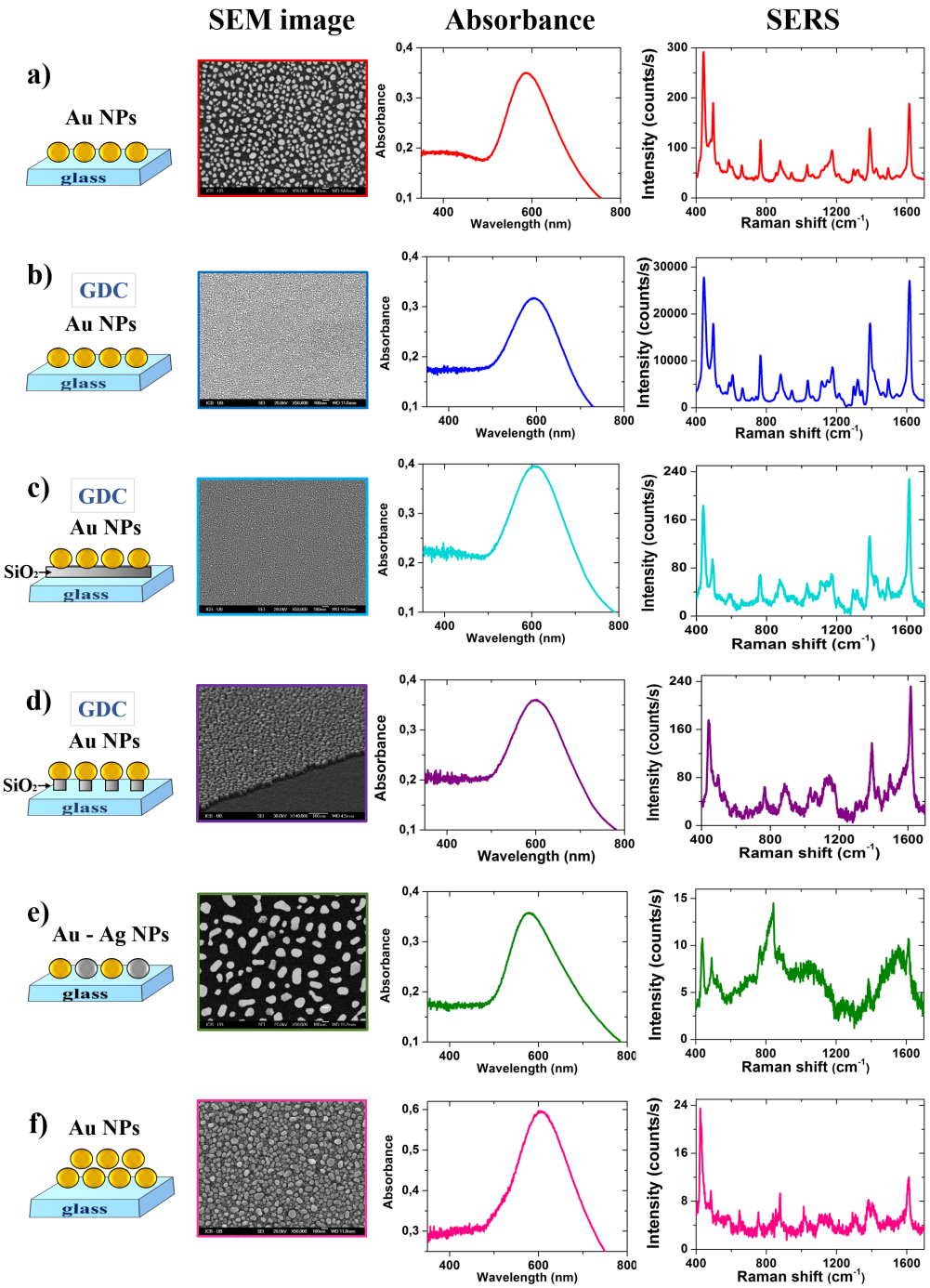

Fig. 2.12: Schematic representation and SEM images of SERS substrates presented with LSPR spectra of substrates. SERS spectra of methylene blue (10^{-6} M) on the corresponding substrates are shown. Au nanoparticle substrate (a) without and (b) with glow charge cleaning (GDC). Au nanoparticles on (c) silica layer and (d) silica pillars. (e) Au-Ag bimetallic and (d) twice deposited Au nanoparticle substrate. Scale bar is 100 nm for all SEM images.

Last two substrates were fabricated using non-GDC protocol. It is necessary to remark here that these two substrates were produced by two successive film deposition. More precisely, the first amorphous layer was deposited (Au or Ag) on the glass substrate and followed by thermal annealing to form crystalline nanoparticles. This step is repeated by the deposition of a second amorphous (Au) layer and followed by thermal annealing. The bimetallic Ag - Au nanoparticle and successive twice deposited Au-Au nanoparticle substrates are referred as (e) and (f), respectively.

The schematic presentation, SEM image and absorbance spectrum of each substrate are presented in Fig.2.12. The SERS performance of the substrates is evaluated by detecting methylene blue solution at 10^{-6} M concentration. All SERS experiments were carried out in liquid medium and the temperature was maintained at 20 ℃.

LSPR wavelengths were found at 587, 593, 607, 577, 600, 577 and 605 nm for the presented substrates in Fig.2.12.(a) to (f). The LSPR results concerning the substrate (a) and (b) have already discussed earlier (see Fig.2.9). GDC substrate has a residual redshift compared to non-GDC substrate due to the small interparticle distance and the associated increased coupling. The substrate (c), in which the gold nanoparticles lays on the silica layer, exhibits the largest λ_{max} value. When the silica layer between the nanoparticles is etched, thereby the nanoparticles are suspended on silica pillars (d), the λ_{max} value is 7 nm blue-shifted. Substrates (e) and (f) were fabricated by the same protocol which consist of two successive metallic layer deposition. The only difference between these two substrate is that the substrate (e) contains silver as a second layer whereas the substrate (f) contains gold. After post-annealing process (performed after each layer deposition), the size and distribution of nanoparticles are clearly different for these two substrates (Fig.2.12.(e) and (f)). The bimetallic Au-Ag substrate (e) has the lowest λ_{max} value due to presence of Ag. On the other hand, the substrate (f) has a λ_{max} which is closer to the other gold SERS substrates. The relative absorbance value is higher for the substrates (d) and (e) in comparison with other substrates shown in Fig. 2.12, since the nominal thickness of these substrates is thicker [96].

The fabrication procedure of these substrates with their λ_{max} wavelength at absorbance spectrum and the maximum signal intensity at SERS spectra are listed in Tab.2.3.

Tab. 2.3: Fabrication details of SERS substrates with λ_{max} wavelength at absorbance spectrum. Maximum Raman signal intensity, I_{max}, is obtained from corresponding SERS spectrum of Methylene Blue at 10^{-6} M concentration.

Substrate	**Layer(s)**	**Fabrication protocol**	λ_{max} **(nm)**	I_{max} **(cps)**
(a)	Au NPs	non-GDC	587	291
(b)	Au NPs	GDC	593	27810
(c)	Au NPs on SiO_2 layer	GDC	607	225
(d)	Au NPs on SiO_2 pillars	GDC	600	226
(e)	Ag and Au NPs	non-GDC	577	12
(f)	Au and Au NPs	non-GDC	605	24

Figure 2.13 presents the schematic drawing of the nanoparticle substrates arranged in function of their Raman signal yields.

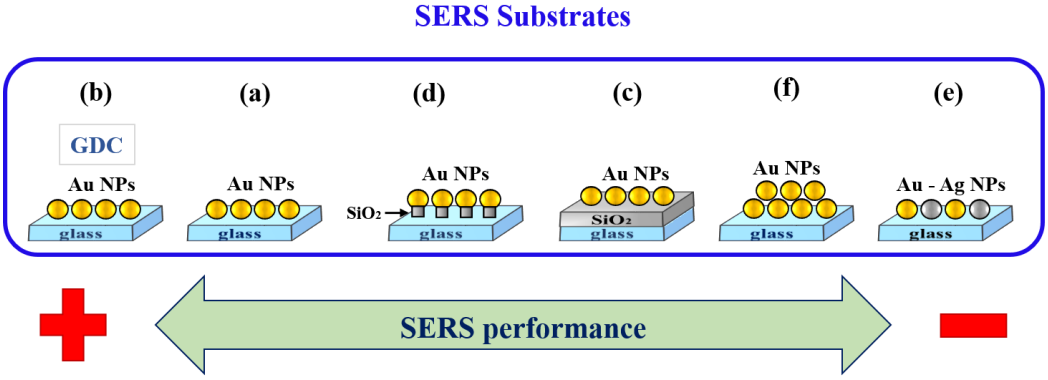

Fig. 2.13: Schematic representation of SERS substrates. Au nanoparticle substrate (a) without and (b) with glow charge cleaning (GDC). Au nanoparticles on (c) silica layer and (d) silica pillars. (e) Au-Ag bimetallic and (d) twice deposited Au nanoparticle substrate. Scale bar is 100 nm for all SEM images.

We have recorded approximately 100 times stronger SERS signal intensity with the substrate (b) comparing with substrate (a). This is linked to the unique surface geometry (uniform size and very short interparticle distances) of substrate (b) which evidently produces stronger signal enhancement.

The morphological features of the substrate (b) and (c) is seen quite similar from SEM images, although GDC substrate has ∼125 times stronger SERS signal intensity. This indicates that the adjacent silica layer at the vicinity of the nanoparticles probably decreases the plasmon coupling of nanoparticles and that yields low Raman signal intensity. Concerning the substrate (d), where the gold nanoparticles lay on the silica pillars, the SERS spectrum is very similar to the spectrum of substrate (c). The suspending of nanoparticles from glass substrates should have increase the plasmon coupling. On the other hand, methylene blue is very small molecule hence it may drop on the glass substrate by traversing the interparticle distance of nanoparticles. Therefore, being far from the vicinity of nanoparticles decreases the Raman signal intensity of methylene blue.

The bimetallic Au-Ag substrate consist of a large variety of nanoparticle shapes including spherical forms, nanorods and pentagon-like geometries as the substrate (a). The common features of these both substrates is the fabrication by non-GDC protocol which yields the variety of nanoparticle shape. On the other hand, the interparticle distance and the size of nanoparticles are larger for the substrate (e). This is linked to the presence of silver, accordingly the silver-gold interactions during post-annealing process. Consequently, we have observed the lowest Raman signal intensity and number of peak for substrate (e).

The surface of substrate (f) is fully charged compared with the other non-GDC substrates (substrates (a) and (e)). The successive gold layer deposition and the post-annealing process result a coverage of the substrate with nanoparticles at various shape and height with very short interparticle distances.

This configuration is not optimum for Raman signal exaltation due to high inhomogeneity, nevertheless it produces two times stronger SERS signal than substrate (e).

Consequently, the typical GDC fabrication –substrate (b)– produced the highest SERS performance that includes the highest number of peaks at the SERS spectrum with approximately 100 times stronger signal intensity compared with other fabrications. Hence, the sensitivity, homogeneity and repeatability of SERS spectra production are investigated for only typical GDC fabrication.

2.2.2.2 Sensitivity of GDC gold nanoparticle substrates

To characterize the plasmonic response of the GDC substrate, absorbance measurements of the film were studied by varying concentration of methylene blue (MB). For this aim, methlylene blue was prepared at four different concentrations (10^{-15} M, 10^{-12} M, 10^{-9} M and 10^{-6} M) by diluting with deionized pure water (PURELAB UHQ II, ELGA). For each concentration, the spectra were collected from six different positions under the MB droplet including the center and edges. No substrate was re-used since the molecular adsorption of the previous solution could cause an error signal even after rinsing with solvent, detergent, or distilled water. In order to record comparable results, the substrates were first submitted to absorbance measurement in order to determine the characteristic LSPR wavelength before exposing the surface to reporter molecules.

The absorbance spectra of MB are presented in Fig. 2.14 for 10^{-15} M, 10^{-12} M, 10^{-9} M and 10^{-6} M concentrations. The relative change in absorbance (ΔI), the full width at half maximum (FWHM) of resonance and the centered wavelength (λ_{max}) are reported in Tab.2.4 for each investigated concentration.

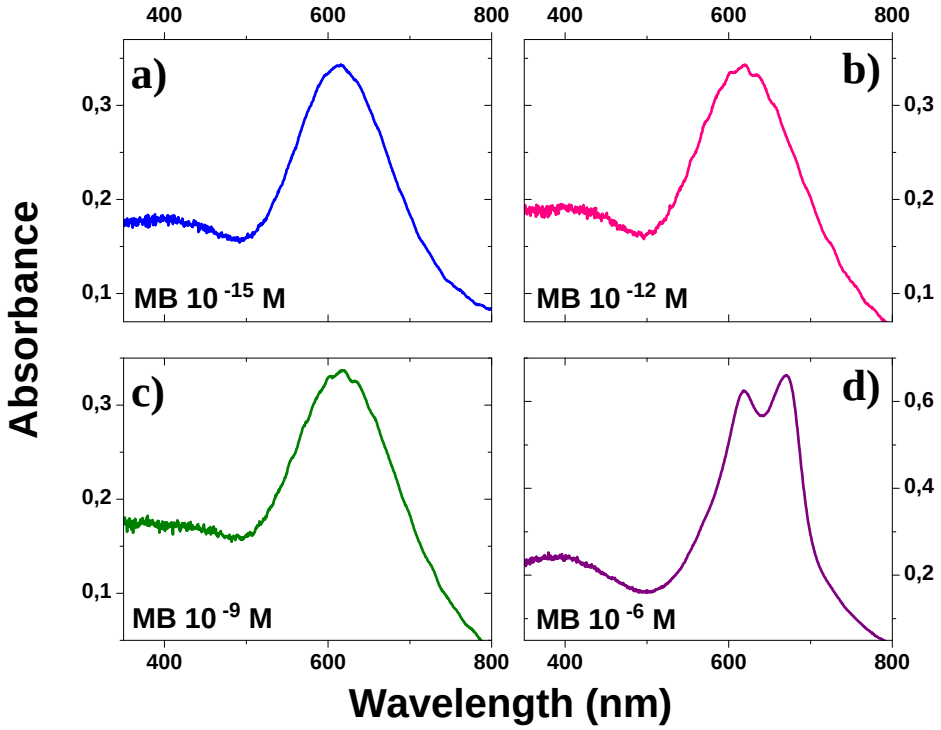

Fig. 2.14: LSPR spectra of 10 μl of Methylene Blue on Au nanoparticle substrate at (a) 10^{-15} M, (b) 10^{-12}, (c) 10^{-9} and (d) 10^{-6} M concentrations.

Tab. 2.4: Investigation of methylene blue concentration impact on the LSPR resonance of the GDC substrate.

Concentration (M)	**ΔI**	**FWHM (nm)**	**$\Delta\lambda$ (nm)**	**λ_{max1} (nm)**	**λ_{max2} (nm)**
10^{-15}	0.184	113	21	614	–
10^{-12}	0.177	116	26	619	–
10^{-9}	0.179	112	25	618	–
10^{-6}	0.478	104	-	619	670

We have observed that the λ_{max} values of the absorbance spectra vary less than 1 nm for any observation position in the droplet for a given concentration of methylene blue. The adsorbed molecules cause a shift in $\lambda_{\max}$ due to the change in local refractive index [97]. Here, we have measured $\Delta\lambda$ shifts, of 21 nm, 26 nm and 25 nm for 10^{-15}, 10^{-12} and 10^{-9} M concentrations, respectively. We have observed the highest relative absorbance intensity for methylene blue at 10^{-6} M. For this concentration, the absorbance spectrum features two peaks corresponding to the absorption peaks of methylene blue [98] that are modulating the LSPR spectrum. Regarding this LSPR analysis, we conclude that the sensing response is not linear. This is linked to the quantity of adsorbed species on the surface which is not proportional to the volume concentration since no surface functionalization was applied.

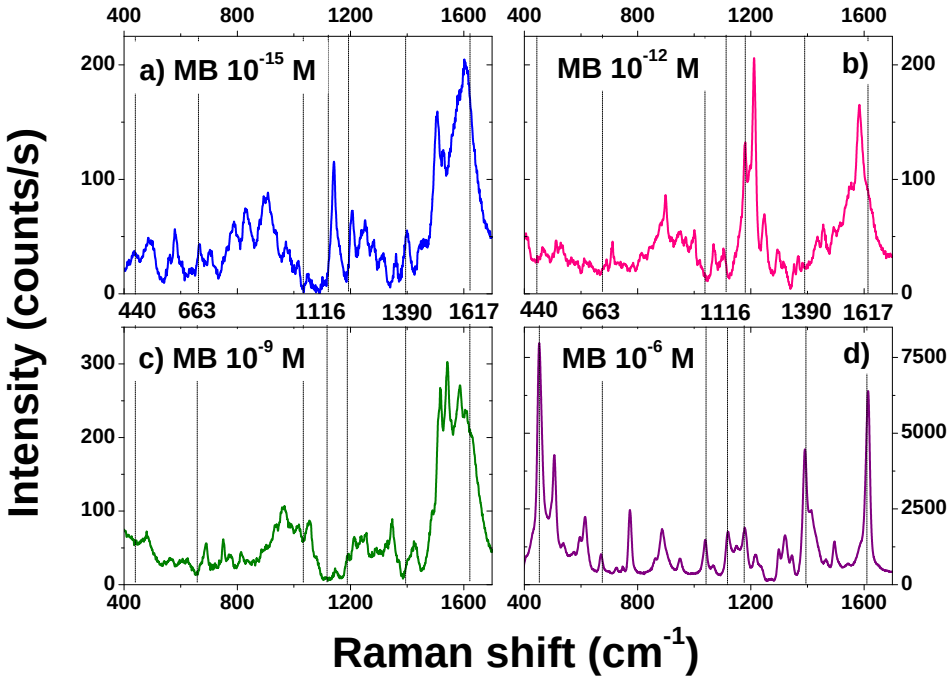

Fig. 2.15: SERS spectra of MB at various concentrations on Au nanoparticle substrate. (a), (b), (c) and (d) correspond to SERS spectrum of MB at 10^{-15} M, 10^{-12} M, 10^{-9} M and 10^{-6} M concentrations, respectively.

We have investigated the SERS response of the molecules exposed to GDC-substrates at four different concentrations (10^{-6} M, 10^{-9} M, 10^{-12} M and 10^{-15} M). Figure 2.15 displays the corresponding Raman spectra acquired with the same experimental parameters. Seven characteristic lines of methylene blue (MB) are labeled in the spectra [90] and listed in Tbl.2.5.

Tab. 2.5: The Raman shifts, the peak occurrence and band assignments of Methylene Blue are taken from Xiao et al.[90]. Abbreviations: ν, stretching; α, in-plane ring deformation; β, in-plane bending; γ, out-of-plane bending and δ, skeletal deformation.

Peak N°	**Raman shift (cm^{-1})**	**Band assignments**
1	440	δ(C-N-C)
2	663	γ(C-H)
3	1032	β(C-H)
4	1116	γ(C-H)
5	1177	ν(C-N)
6	1390	α(C-H)
7	1617	ν(C-C) ring

Fluctuations of the Raman line intensities and spectral wandering are observed for the lower concentrations than 10^{-6} M. These effects are subject to intense discussions in the literature [99, 100, 101] and are usually explained by the nature of the enhancement processes [46, 102], the diffusion of the specimens [103, 52], and measurements at the single molecule level [104, 105]. Among the four spectra, the largest number of peaks detected are unsurprisingly observed for the highest concentration since the Raman intensity is concentration dependent [106, 107].

2.2.2.3 Homogeneity of GDC gold Nanoparticle substrates

In order to assess the spatial reproducibility of the measurement, we show in Fig. 2.16.(a) a confocal map of the spectrally integrated SERS response as a function of sample position with respect to the laser focus.

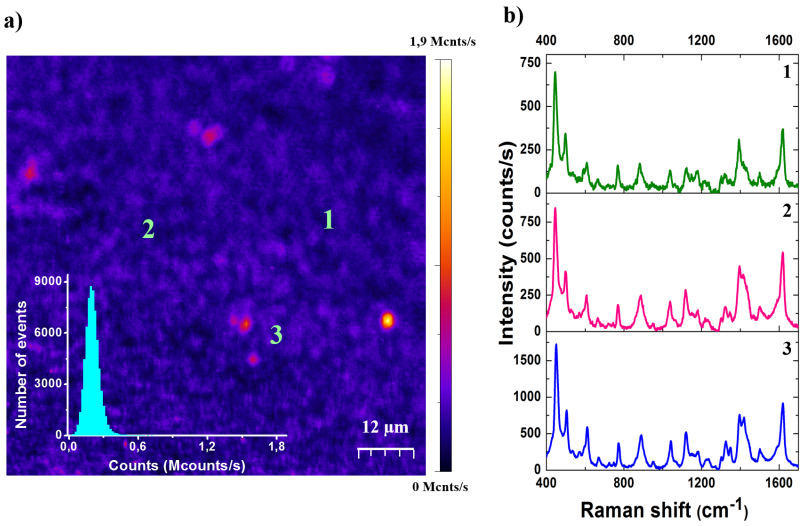

Fig. 2.16: Confocal integrated Raman intensity map obtained at 10^{-6} M of methylene blue on a GDC Au nanoparticle substrate. SERS spectra were collected from different positions on the Raman scattering map.

The 60 μm $\times$ 60 μm scan is obtained from a methylene blue solution concentrated at 10^{-6} M. We have chosen this concentration to insure a homogeneous spatial coverage of the molecules on the substrate. The histogram of detected photon counts (inset of Fig. 2.16.(a)) indicates a relatively narrow distribution centered at 2 kcnts/s. SERS spectra collected from three different positions labeled on the map shown in Fig. 2.16.(b). For such concentration, the observation point has almost no impact on the peak position of the SERS spectra. This is linked to uniformity of the interparticle distances and nanoparticle sizes already emphasized in Fig. 2.16.(b) that yield to a homogeneous Raman response across the sample. A few pixels of the Raman intensity map generate a higher Raman intensity (bright spots) and are probably resulting from residual structural defects of the substrate or a local aggregation of the molecules.

Note that the amplitude of the SERS signals in Fig. 2.16.(a) and (b) differs because the confocal image represents an integrated signal measured with an avalanche photodiode whereas the spectra are acquired with a CCD camera with a different quantum efficiency.

2.2.2.4 Repeatability of SERS spectra production

We have recorded a total of 392 SERS spectra for each concentration of methylene blue (MB) in order to perform statistical analyses. Each spectrum was examined by a Matlab script in order to determine the peak positions. We have qualified by their statistical occurrence (over 40 %) 38 peaks on the SERS spectra when taking into account all concentrations. 26 peak matches were obtained between our results and the literature [90, 93]. From Matlab data, we have calculated the observed peak occurrence versus corresponding wavenumbers (cm^{-1}).

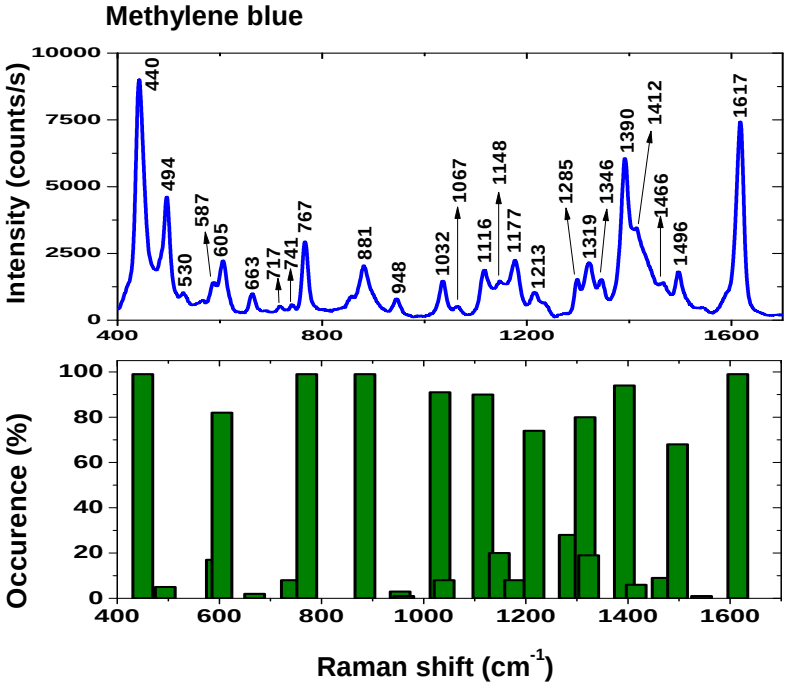

Fig. 2.17: SERS spectrum of methylene blue and the occurrence histogram of peak positions obtained from 392 SERS spectra of methylene blue at 10^{-6} M concentration.

Figure 2.17 presents the Raman bands of MB with their observation frequency.

The wavenumbers at 440, 605, 767, 881, 1032, 1116, 1319, 13904 and 1617 cm^{-1} are observed with over than 80 % of occurrence for SERS spectra of methylene blue at 10^{-6} M concentration. This indicates the high reproducibility of our substrates for SERS experiments. We listed all observed Raman bands of MB with their occurrence in Tab.2.6.

Tab. 2.6: Enhanced Raman bands of MB obtained from all SERS spectra at different concentrations. † and § corresponds to the reference [90] and [93], respectively.

Raman band (cm^{-1})	440†, §	494†	530	587§	605†	663 †, §
Occurrence (%)	99	5	1	17	82	2
Raman band (cm^{-1})	717†, §	741	767	881†	948§	1032†, §
Occurrence (%)	12	8	99	99	3	91
Raman band (cm^{-1})	1067†, §	1116†	1148	1177	1213†	1285
Occurrence (%)	8	90	20	8	80	28
Raman band (cm^{-1})	1319†, §	1390†, §	1412†, §	1466†, §	1496	1615†, §
Occurrence (%)	80	94	6	9	68	99

Finally, we have observed the sensitivity of a molecular detection performed on GDC Au nanoparticle substrates. We have detected eight specific Raman bands of methylene blue even for attomolar concentration (462, 823, 954, 1031, 1152, 1256, 1375 and 1542 cm^{-1}). We found a significant contribution of GDC process to homogeneity of substrates and this leads the generation of "hot spots" all over the substrate. Therefore, the production of successive SERS spectrum is became only function of molecule distribution on the substrate.

2.3 Conclusion

A home-built SERS – absorbance setup was used for analyzing reference samples.

We have developed two fabrication procedure to procure metallic nanoparticle–covered substrates. Our protocol is flexible and it allows the fabrication of gold, silver, bimetallic silver-gold and multilayer nanoparticle substrates. We have investigated the impact of morphology and constituent metal

of the nanoparticles on the localized surface plasmon resonance (LSPR) and surface enhanced Raman spectroscopy (SERS) measurements.

The accuracy of our SERS setup has been confirmed by analyzing *trans*-1,2-bis(4-pyridyl)ethylene. The performance of gold nanoparticle substrates has been evaluated with methylene blue at various concentration (from 10^{-6} to 10^{-15} M). We have detected eight specific Raman bands of methylene blue even for 10^{-15} M concentration. The homogeneity of SERS spectra production has been investigated over the surface area by confocal integrated Raman intensity map. We have detected ten Raman bands over than 80% of occurrence for SERS spectra of methylene blue at 10^{-6} M concentration.

In next chapter, we will present our HS-AFM and SERS co-applications for biomolecule detection.

3

Applications of HS-AFM and SERS for biomolecule detections

Surface enhanced Raman spectroscopy is a powerful characterization technique for chemical analyses. The constitution and design of nanoparticle substrates plays a crucial role for achieving an enhanced spectrum.

Prior to biomolecule detections, we have investigated the efficacy of our SERS substrates with well-known SERS analytes as *trans*-1,2-bis(4-pyridyl)ethylene (BPE) and Methylene Blue (MB) in the previous chapter. We have evaluated the sensitivity, homogeneity and repeatability of the plasmonic-active substrates.

The present chapter is dedicated to SERS and HS-AFM analyses of complex biomolecules including human microsomal cytochrome b5, small heat shock protein Lo 18, murine noroviruses and detergent resistant membrane domains of leukaemic monocyte macrophage cells. This work can be considered under three parts:

1. Detection of complex human microsomal cytochrome b5,
2. Investigation of conformational changes of small heat shock protein Lo 18,
3. Cell membrane–virus interactions.

3.1 Detection of complex human microsomal cytochrome b5

3.1.1 Cytochrome b5

In collaboration with the Institute FEMTO-ST (UMR CNRS 6174), under the direction of Drs. W. Boireau and C. Elie-Caille, we have performed experiments relative to the conception of new biosensors (Labex ACTION Smart System – WP4 Microsystems, technologies & components integration) using gold nanoparticle substrates. We have investigated small hemoprotein cytochrome b5 by LSPR and SERS, however only SERS results are presented in this manuscript.

In organites and mostly in mitochondrion of eukaryotes and aerobic prokaryotes, cytochrome b is a component of respiratory chain complex III (also called bc1 complex) involved in electron transport at mitochondrial membrane. Mitochondrion produces adenosine triphosphate (ATP), a complex molecule that contains the nucleoside adenosine and a tail consisting of three phosphates. This complex molecule is critical for all life forms from the simplest to the most complex ones. Adenosine triphosphate is a highly energy-giving molecule that serves as the primary energy currency of the cell. ATP is the most widely distributed high-energy compound within the human body. This ubiquitous molecule is used for building complex molecules, to contract muscles, generate electricity in nerves and light fireflies. All fuel sources of nature, all foodstuffs of living things, constitute the raw materials enabling ATP production by the organism, which in turn powers virtually every activity of the cell and organism.

Cytochromes are membrane-bound (i.e. inner mitochondrial membrane) hemoproteins containing heme groups that can be responsible of ATP generation, or implied in detoxication of human organism through a collaboration with cytochrome P450 monooxigenase that is responsible for the metabolism of a wide range of endogeneous or exogeneous subtrates – via electron transport. Cytochromes a, b and c can served to transfer the electrons to higher redox potential molecules [108].

Cytochrome b5 is a ubiquitous membrane-bound hemoprotein found in microsomes of animals, plants, fungi and purple phototrophic bacteria. The heme group is a highly conjugated ring system (which allows its electrons to be very mobile) surrounding a metal ion, which readily inter-converts between the oxidation states. It is a small acidic membrane protein in the form of cylinder. This protein shows a high identity for mammalians. It plays a part in the number of reduction, oxidative and elongase reactions as an obligate component or modifier [109].

3.1.2 Analysis of human cytochrome b5 protein

We have evaluated the sensing capacity of our SERS substrates with a relevant human protein. We have investigated the performance of our fabrications on the SERS experiment with the reference samples previously. The advantage of references samples is their known spectral features and high yield at Raman intensity. Our aim in this study was to implement our substrates to Raman identification of a complex biomolecule.

Cytochrome b5 is derived from human microsomal cytochrome b5 by genetic engineering resulting in the substitution of (i) the 26 C-terminal amino-acid residues by the – NGHHHH–COOH sequence and (ii) the serine 23 in Hb5(His)4 by a cystein as previously described [110, 111]. Cytochrome b5 was reduced with dithiothreitol (DTT) in order to obtain a 3D structure which is surrounded by unique cysteine and unique sulfhydryl residue. To have this sulfhydryl moiety aid to perform packed and oriented self-assembled cytochrome b5 monolayer onto gold surface via chemisorption. Thereby, the protein is adsorbed by the gold nanoparticles and immobilized on the SERS substrate. The homogeneity and orientation of a reconstituted and self-assembled layer of engineered cytochrome b5 on a gold film has already been shown using TOF-SIMS and AFM approaches [112, 113].

In our experimental conditions, cytochrome b5 solution at 4.8×10^{-9} M concentration is diluted by 104×10^{-9} M of DTT.

This concentration of cytochrome b5-DTT solution is too low to establish a self-assembled monolayer onto gold nanoparticle substrate. LSPR analysis of cytochrome b5 in function of concentration can be aid to understand the etablishement of protein monolayer on the substrate. This analysis requires the functionalizaton of the nanoparticle substrate. However, we prefered to keep the same experimental conditions with the Raman experiments where the analyte is directly deposited on the nanoparticle substrate. Therefore, we have analyzed the distribution of cytochrome b5 - DTT solution on the substrate by conventional AFM. We haven't performed HS-AFM analysis since the protein is immobilized on the substrate.

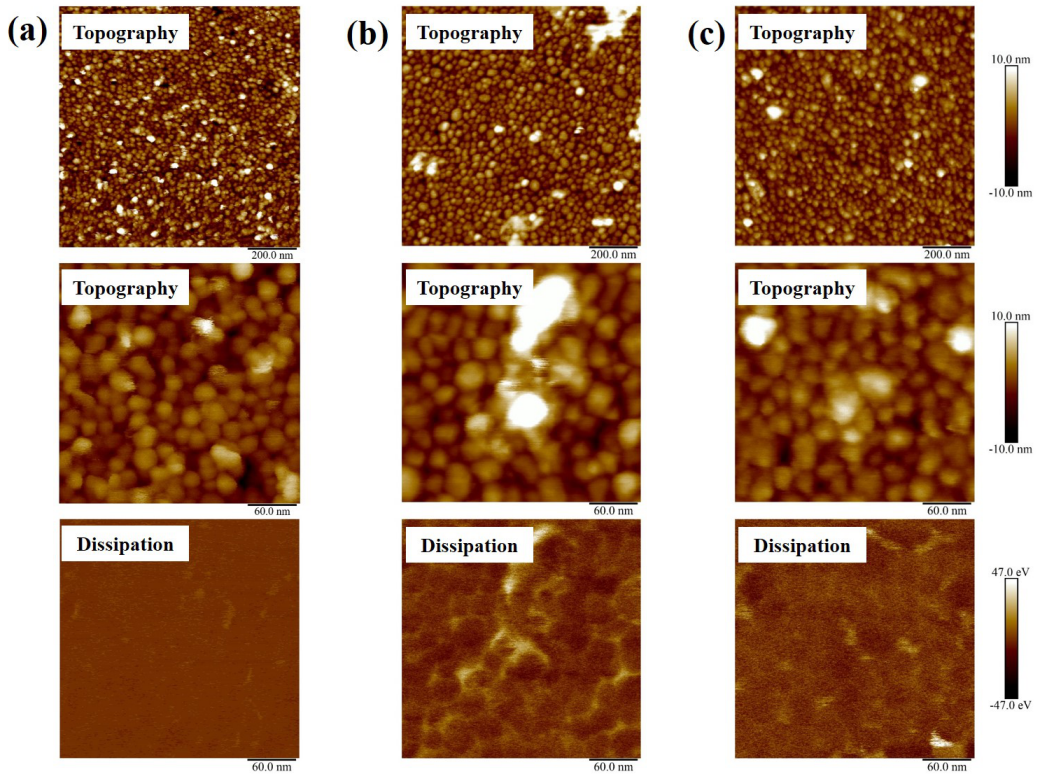

Fig. 3.1: AFM images of Au nanoparticle substrates are obtained in PBS medium using PeakForce mode. Scan sizes are 1 µm and 300 nm. Topography and dissipation images are presented for each sample. (a) Au NPs. 90 μl of cyt b5-DTT solution was deposited on Au NPs substrate at (b) [4.8:104] nM and (c) [4:86] μM concentrations.

AFM images of the GDC substrate were obtained in PBS medium. Figure 3.1.(b) and (c) are the topography images acquired after the deposition of [Cytb5:DTT] solutions at [4.8:104] nM and [4:86] μM concentrations, respectively.

As seen from topography images, it was difficult to distinguish the proteins from the nanoparticles regardless of the concentration because of the size of the gold nanoparticles. However, the concentration impact is more evident on the dissipation channel (last line).

The series of images were obtained from an AFM operating in PeakForce mode (Bruker, Multimode 8). The dissipation images are constructed from the hysteresis measured between approach and retract tip/surface distance at each pixel. A surface constituted of one kind of material should have a homogeneous dissipation image as in the case of the bare gold substrate. The dissipation image of case (b) shown an evident contrast. We have attributed this variation to the co-presence of Au nanoparticles and cytochrome b5. To verify this hypothesis, we have compared the dissipation images of the gold surfaces covered by more concentrated cytochrome b5 - DTT solution. As expected, the overall contrast of the image is reduced as the result of a greater amount of cytochrome b5 absorbed on the nanoparticles.

The absorption band of cytochrome b5 is centered at 510-560 nm [114, 115]. Our experiments are carried out using an excitation light of 785 nm in order to evaluate the performance of our substrate at detecting vibrational fingerprints of non-resonant proteins at nanomolar concentrations. The SERS spectrum of cytochrome b5 - DTT is presented in Fig.3.2.

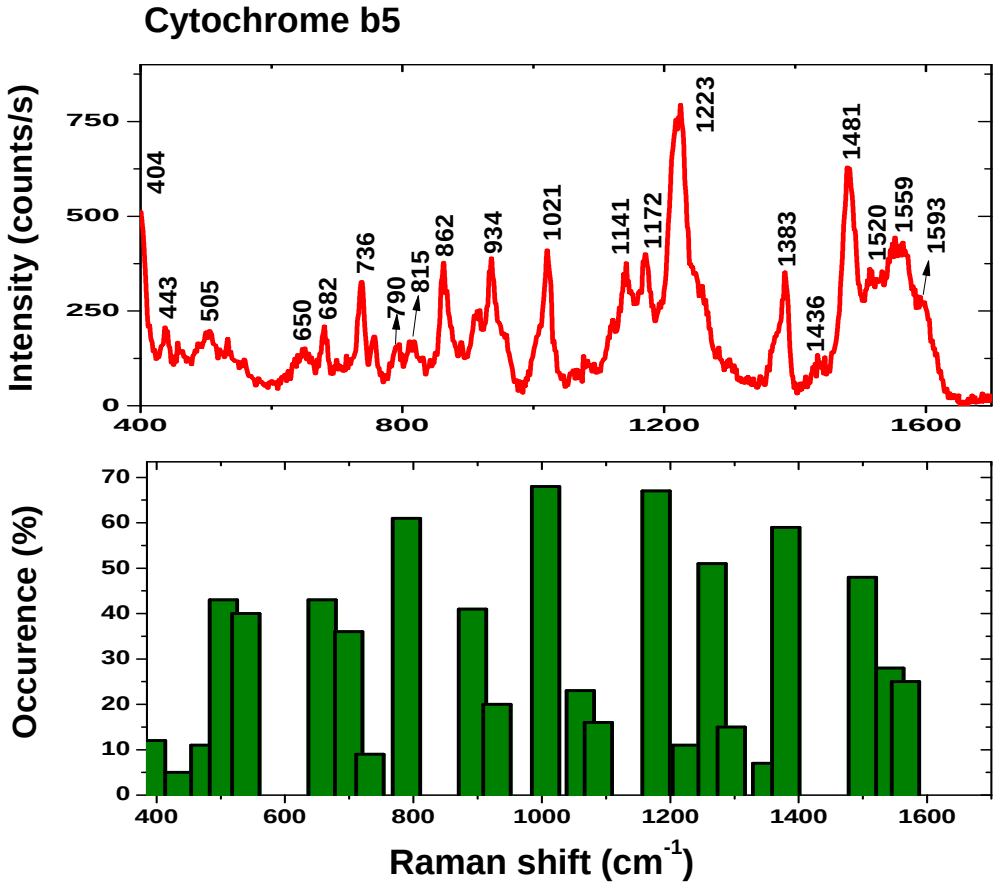

Fig. 3.2: SERS spectrum of cytochrome b5 - DTT [4.8:104] nM solution and histogram of peak positions.

We have compared our data with those of purified cytochrome b5 protein of rat and horse liver microsomes [114, 115]. We have found that the peaks at 736 cm^{-1}, 934 cm^{-1}, 1141 cm^{-1}, 1172 cm^{-1}, 1223 cm^{-1}, 1383 cm^{-1}, 1559 cm^{-1} are common for cytochrome b5 proteins regardless of its origin. These bands are slightly shifted in our SERS spectra due to presence of metal substrate. Similarly, we have observed the peak coincidences with those of resonance Raman spectra of cytochrome b558 [116]. The occurrence of peak positions is given at Fig.3.2. The wavenumbers at 790 cm^{-1}, 1006 cm^{-1}, 1172 cm^{-1}, 1265 cm^{-1} and 1383 cm^{-1} have a more than 50 % occurrence.

3.2 Investigation of conformational changes of small heat shock protein Lo 18

In collaboration with the Institute IUVV UMR PAM (AgroSup), under the direction of Pr. J. Guzzo and Dr. S. Weidmann, we have performed experiments on a small heat shock protein that involved in the malolactic fermentation of wine... in Bourgogne of course!

The small heat shock proteins can form a dimer (basic block) or an oligomer conformation in function of the pH level [117, 118]. In this section of the thesis, we have investigated the conformational changes of small heat shock leuconostoc oenos protein by AFM and SERS. HS-AFM analyses are implemented to observe the topographic variations in the real-time whereas SERS analyses are performed to detect corresponding chemical features of the protein.

Leuconostoc oenos (Lo 18) is a small heat shock protein (sHsp) produced by a lactic acid bacteria Oenococcus oeni (O. oeni) when the bacteria are in a stress environment or at the stationary growth phase [119, 120, 121]. The organic acids and external pH influence the growth of O.oeni [122]. Lo 18 protein regulates the acidity of wine that improves the quality and stability of wine.

The small heat shock proteins are diversified in sequence and molecular mass ranging between 14 and 43 kDa [123]. They are widely distributed in many organisms at different cellular localization, suggesting an involvement in various cellular mechanisms [124]. A common feature of small heat shock proteins is their association to form large oligomer complexes of 150 to 600 kDa in bacteria. Many studies have shown that small heat shock proteins protect denaturated polypeptides against irreversible aggregation. This action called chaperone activity and it has been demonstrated in-vivo and in-vitro experiments for small heat shock proteins [125, 126]. The molecular chaperone function of the small heat shock Lo 18 protein can be influenced by the concentration, pH level, chemical and thermal stress [127, 128].

3.2.1 Observation of conformational changes of Lo 18 protein

sHsp Lo 18 production, the extraction from bacteria and the purification processes have been reported previously [129]. The protein solution is kindly provided by J. Guzzo and his research team. The initial pure protein solution (3μg/ml) is diluted by 100 times (30 ng/ml) with pH 6, pH 7 and pH 9 solutions. The diluted sHsp Lo 18 solutions at different pH levels were analyzed on a mica surface using the EBD tip deposed ultra-short cantilevers (Olympus, f=580 kHz, k=0.1 N/m with an oscillation amplitude limited to 0.5 nm). The successive HS-AFM images of sHsp Lo 18 at three different pH levels are presented in Fig.3.3. All images are in 35 $\times$ 35 nm^2 size and recorded with the scan rate of 4 frame/s.

According to experimental results, we have found that sHsp Lo 18 has a dimer form at pH 9. The diameter of basic block (dimer) of the protein has found around 3.5 nm. However, sHsp Lo 18 has an oligomeric conformation at pH 7 and 6, as seen from Fig.3.3. It has been previously reported that sHsp Lo 18 has 16-18 sub-units in its oligomeric conformation (or 8-9 basic blocks) at pH 5, 6 and 7 and it has a dimeric form at pH 8 and 9 [129, 130].

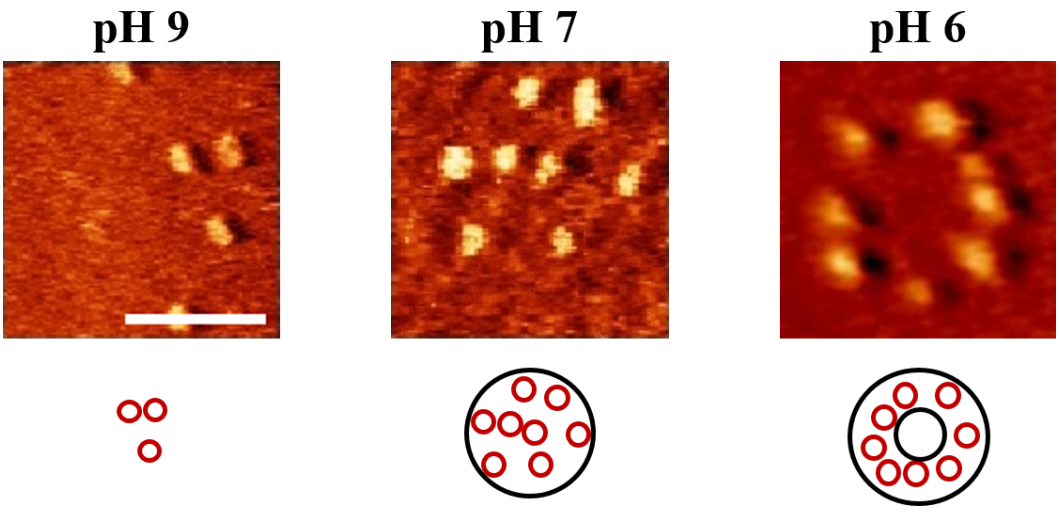

Fig. 3.3: HS-AFM images of sHsp Lo 18 at different pH levels. Images were recorded at a scan rate of 4 frames/sec and in a scan area of 35 nm $\times$ 35 nm.

The number of sub-units as well as the velocity of dimers on the mica surface are given in Table.3.1. The velocity of dimers were calculated for each pH level from their trajectory. The highest velocity with 70 nm/s is found at pH 9 where the protein is in dimeric form. At pH 6, sHsp Lo 18 forms oligomers and the velocity of dimers decreases to 9 nm/s due to the interactions between the dimers.

Tab. 3.1: Experimental HS-AFM results of sHsp Lo18.

pH level	Number of sub-units	Diameter	Velocity of dimers
9	2	3.5 nm	70 nm/s
7	16–18	15–17 nm	12 and 47 nm/s
6	16	13 nm	9 nm/s

The chaperone activity of small heat shock protein Lo 18 is particularly optimized at pH 7. Therefore, we have focused on this pH level to observe the oligomer formation.

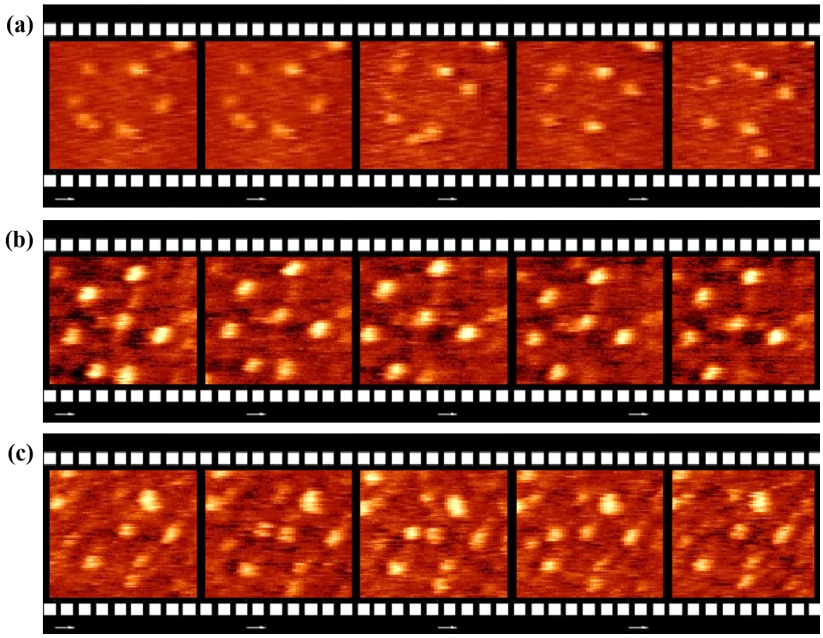

Fig. 3.4: HS-AFM images of sHsp Lo 18 at pH 7. (a) First conformation of protein, a ring-like structure is formed by six dimers. (b) Second conformation, a dimer is moved in the center of ring-like structure. (c) Third conformation, two dimers are present in the ring-like structure. Scan rate = 4 frames/sec and scan size = 35 nm × 35 nm.

The morphology of sHsp Lo 18 at pH 7 is presented in Fig.3.4. HS-AFM imaging was carried out in the same conditions with previous sHsp Lo 18 analyses. A ring-like structure is formed by the organization of 6 to 8 dimers due to the hydrophobic forces at pH 7. The average diameter of ring-like structure has found 15 nm. We have observed that the dimers move around an equilibrium position thereby the gap distance evolve over time. The velocity of dimers at the ring-like structure has found 12 nm/s. In Figure 3.4.(b), an additional dimer was found in the center of ring-like structure that indicates the conformational changes of the protein. We have observed three different conformations for this pH level. The third conformation of Lo 18 is presented in Fig.3.4.(c) where the ring-like structure consists of two dimers in the center. These dimers at the center of ring-like structure has higher mobility than those of the ring-like structure and their velocity has found 47 nm/s. The observed topographic features of sHsp Lo 18 are agreed with previous results [129].

3.2.2 SERS analysis of Lo 18 protein

We have investigated the chemical variations of sHsp Lo 18 in function of pH level and concentration by SERS measurements. The protein solutions were deposited directly on a crystalline gold nanoparticle substrate without any functionalization. The gold nanoparticle substrates -referred as GDC- were previously described (see subsection 2.1.2.1). Prior to SERS experiments, the optical features of the substrates were analyzed by LSPR measurements.

All SERS spectra were collected from the liquid samples in ambient conditions. The samples were excited via 785 nm laser light with the spot diameter of 300 nm. The spectra of the protein were recorded with 1 s acquisition time which is relatively close to the scan rate of HS-AFM images (4 frame/s, see Fig.3.3). This aids to compare the dynamics of sHsp Lo 18 obtained from both HS-AFM and SERS analyses.

Firstly, we have investigated the conformational changes of sHsp Lo 18 at pH 7. The initial pure protein solution (3 μg/ml) was diluted by 100 times with phosphate buffered saline (PBS) solution. PBS tablets are purchased from Sigma-Aldrich (pH 7.2 – 7.6 at 25 ℃).

We have presented three characteristic spectra of sHsp Lo 18 at pH 7 in Fig.3.5.(a)-(c). These three spectra are attributed as the typical signature of the sHsp Lo 18 at pH 7 after archiving 1000 spectra.

A Matlab script was used to determine the peak positions and subtract the baseline. The occurrence histogram of peak positions is given in Fig.3.5.(d). The peaks at 894, 977, 1143, 1228, 1351, 1507, 1540 and 1600 cm^{-1} are found more than 40% of occurrence. These peaks are associated to chemical signature of the protein at pH 7. The appearance / disappearance of some peaks at one spectrum to another is explained by structural variations in the middle of the ring-like structure of protein. The occurrence of these peaks is around 10%.

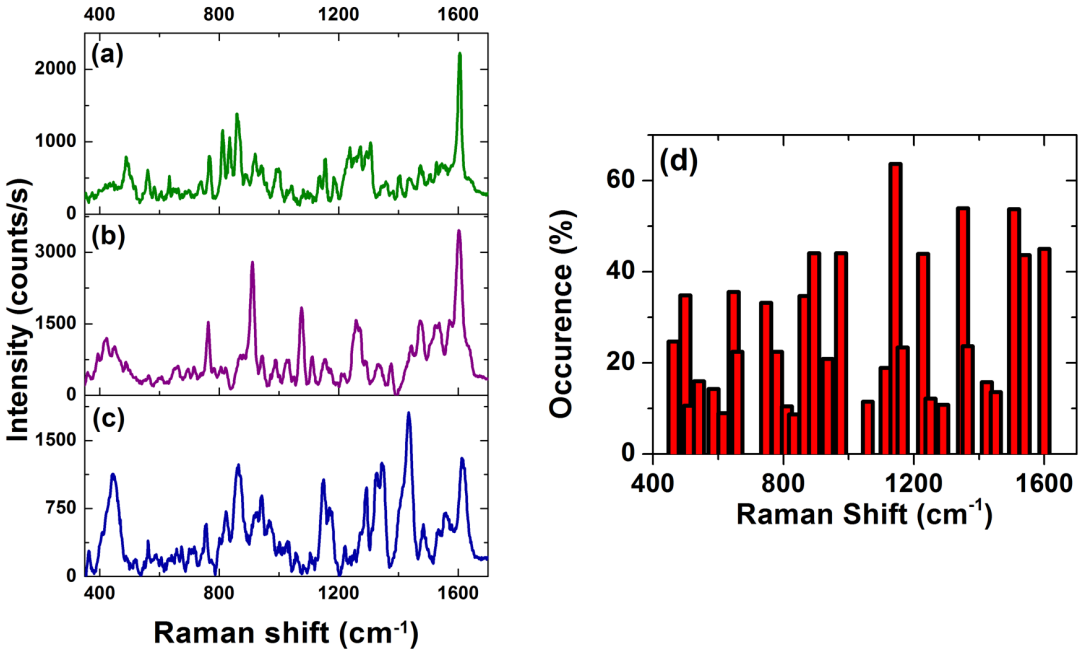

Fig. 3.5: (a), (b) and (c) three characteristic SERS spectra of sHsp at pH 7. (d) The occurrence histogram of peak positions obtained from all data at pH 7 (1000 spectra).

The fluctuations at peak positions are explained by the orientation of molecules that already has been shown by fixing different sides of proteins on a substrate via electrostatic forces [131]. In our case, we have already observed the vibrational motions of the dimers of sHsp Lo 18 by HS-AFM.

This can be influence the peak positions at SERS spectra. The additional one or two dimers in the center of ring-like structure could decrease the vibrational motion of surrounding dimers that can also count a reason of change in SERS spectrum.

We have analyzed sHsp Lo 18 in function of pH level and concentration. The initial pure protein solution (3 μg/ml) was diluted by 100 (30 ng/ml) and 10000 (0.3 ng/ml) times with pH 6, 7 and 9 solutions. SERS spectra of sHsp Lo 18 at low concentration is presented for three pH levels in Fig.3.6.(a). Three principal peaks are found at 1130, 1440 and 1550 cm^{-1} for each pH level of the protein. Also four peaks with low Raman signal intensity are obtained at 800–1000 cm^{-1} region. Any significant difference at the SERS spectra of three pH levels is observed.

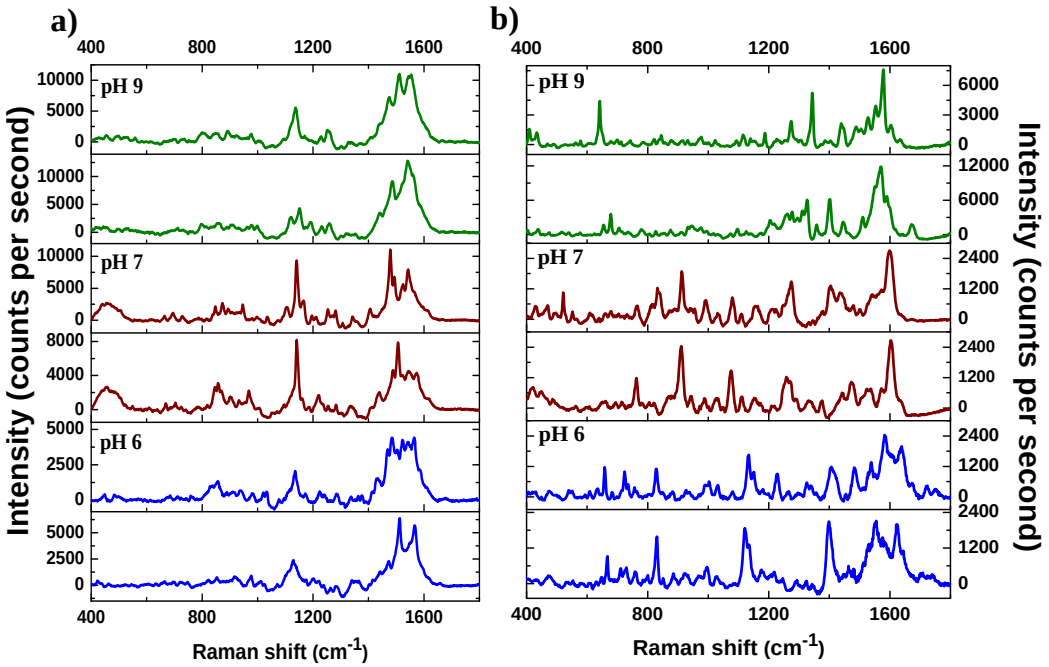

Fig. 3.6: SERS spectra of sHsp Lo 18 solution at (a) 0.3 ng/ml and (b) 30 ng/ml.

The basic blocks of Lo 18 can form higher oligomeric structures due to the forces raised from the interaction between dimers. These forces involve electrostatic, van der Waals and hydrophobic forces and they are pH level dependent. In the acidic solutions, H_3O^+ ions are in majority that results an increase at the hydrophobic interactions thereby the aggregation of the protein.

This is the reason of higher oligomeric conformations (or 8-9 basic blocks) at pH 6 and 7, and conversely in basic block structure at pH 9.

Considering the quantity of the protein on the surface (0.3 ng/ml), the basic blocks may not close enough to interact with each other and to form the oligomeric structure. Therefore, we concluded that the SERS spectra of Lo 18 at low concentration represents the signature of the basic blocks regardless of pH level.

The sHsp Lo 18 forms a ring-like structure with 8 basic blocks at pH 6 via forces explained earlier. But additional one or two basic block can be find in the middle of the ring like structures at pH 7. Finally, Lo 18 protein presents three conformations at pH 7. The region between 800 and 1000 cm^{-1} is found more occupied on SERS spectra of high concentrated Lo 18 protein solution (30 ng/ml) at pH 6 and pH 7.

The Raman bands of sHsp Lo 18 is given in Table.3.2. The Raman bands at 420, 450, 705, 775, 827, 911, 977, 1125, 1258 and 1343 cm^{-1} are found in all spectra and considered as characteristic signature of sHsp Lo 18. The slight variations in peak positions, as can see from table, are explained by the mobility and the orientation of protein. It has already been observed that the mobility of sHsp Lo 18 can be varied 40 nm/s to 300 nm/s in function of pH level. Furthermore, according to pH level, H_3O^+ or HO^- ions can be in majority (or neutral at pH 7) in protein solutions and this electrostatics changes can influence the attachment of protein on the gold nanoparticle surface.

Finally, we present the characteristic Raman spectrum of sHsp Lo 18. The results are confirmed by repetitious measurements. Ten Raman bands are found in common for all pH level of protein, indicating these peaks are associated to the building structure of protein. The conformational changes due to pH level are observed. The disappearance of some Raman bands at low concentration are observed to comparison with higher one, that was expected since Raman spectroscopy is also a quantitative technique.

Tab. 3.2: Enhanced Raman bands of sHsp Lo 18 obtained from SERS spectra shown in Fig.3.6.(b).

pH 6		**pH 7**		**pH 9**	
30 ng/ml	**3 ng/ml**	**30 ng/ml**	**3 ng/ml**	**30 ng/ml**	**3 ng/ml**
428	412	420	423	425	414
466	452	450	456	444	453
-	488	481	-	475	-
-	-	501	-	503	508
529	-	523	-	538	527
545	-	560	-	-	553
585	-	598	-	573	-
606	-	-	-	-	-
666	-	655	661	655	-
-	680	692	-	680	-
711	705	714	705	715	703
765	762	761	775	784	794
798	-	-	-	-	-
-	813	804	-	-	-
827	851	820	851	826	854
888	911	911	900	876	904
923	-	-	927	949	-
998	974	983	968	977	980
1025	1021	1031	-	-	1006
-	-	1078	-	-	-
-	-	1116	-	1103	1117
1123	1122	1157	1138	1125	1144
1174	-	-	-	1198	1192
1219	1207	1212	1214	-	1236
1249	1258	1258	1255	1264	1264
1294	1280	-	1280	-	-
1344	1352	1332	1343	1327	1321
1396	-	1375	-	1362	1362
-	-	1400	-	1395	-
-	-	1444	1441	1447	-
1460	1472	1472	-	-	1479
-	-	1504	1507	1507	-
1551	1520	1532	1545	-	1545
-	1570	-	1573	1570	-
-	-	1602	-	-	-
1626	1655	-	-	1671	-
1697	-	-	-	-	-
1763	-	-	-	-	-

3.3 Cell membrane - Virus Interactions

In collaboration with the INSERM Research Centre UMR866 “Lipids, Nutrition, Cancer – LNC”, under the direction of Pr. P. Pothier and Dr. G. Belliot, we have investigated the murine norovirus binding on the cell membrane.

In this part, we have studied a model system, which involves of murine noroviruses (MNV) and mouse leukaemic monocyte macrophage (RAW 264.7) cells, in order to study gastroenteritis disease. A preliminary study of *real-time polymerase chain reaction (RT-PCR)* technique indicates that the *detergent resistance domains* of RAW cells are involved the murine norovirus binding which depends on the presence of cholesterol. According to these results, we have sought a deeper knowledge on the topography and chemistry of the RAW DRMs - MNV interactions via atomic force microscopy and surface enhanced Raman spectroscopy experiments. Here, we introduced the properties of gastroenteritis disease and the components of model system as well as including the experimental results.

3.3.1 Gastroenteritis

Human noroviruses (NoVs) infection is a significant worldwide disease. Noroviruses are perhaps the perfect human pathogens. These viruses possess essentially all of the properties of an ideal infectious agent: highly contagious, rapidly and prolifically shed, constantly evolving, evoking limited immunity and only moderately virulent allowing most of those infected to fully recover, thereby maintaining a large susceptible pool of hosts. These characteristics have enabled noroviruses to become the leading cause of endemic diarrhea disease across all age groups [132], the leading cause of food-borne disease [133] and the cause of half of all gastroenteritis outbreaks worldwide [134].

Human noroviruses have been identified for the first time after acute gastroenteritis in a school in Norwalk/Ohio (USA) in 1968. Noroviruses cause 90 % of non-bacterial epidemic gastroenteritis in human. Each year, approximately 1.4 billion people get this disease and 1.6 to 2.5 million of them lose their lives.

The mortality of gastroenteritis is higher for old persons and it is between 0.8 to 2.8 %.

The disease is transferred by the faeco-oral way, either direct contact or via contaminated environments. The incubation of noroviruses in human metabolism is 24 to 48 hours. The symptoms are vomiting, diarrhea and abdominal pain. To prevent this disease, the hygienic precautions are important. For example, the diluted chlorine and iodine-based disinfectants effectively eliminate murine norovirus infectivity [135]. Currently, any treatment, neither vaccine nor drug, is available to treat gastroenteritis.

3.3.2 Noroviruses

Noroviruses belong to the genus Norovirus in the family Caliciviridea. Noroviruses have a large genetic diversity that classified under five genogroups. Du-Ping et al. classified noroviruses by using an alignment based on the predicted 3D structures analyzing 164 deduced amino acid sequences of norovirus [136]. The classification contains three levels that are (i) strain, (ii) cluster and (iii) genogroup. Mostly the genogroup 1 and 2 but also 4 can infect humankind. Additionally, the porcine, bovine and murine infections are caused by the second, third and fifth genogroups, respectively. Table 3.3. summarizes the genogroup of noroviruses and their hosts.

Tab. 3.3: Genogroups and hosts of noroviruses.

Genogroup	**Host**	**Cluster**
G1	Human	8
G2	Human\Porcine	17
G3	Bovine	2
G4	Human	1
G5	Murine	1

The cell culture system is an indispensable element to simulate NoVs infection in order to reveal their working mechanism and develop a cure. However, to cultivate the human noroviruses is a big challenge, therefore there are many obscurities about noroviruses. To date, murine noroviruses (MNV) are the only cultivatable noroviruses which can be used as substitute to study human norovirus interactions with its host [137, 138]. Thus, we studied a model system by investigating murine norovirus infection on mouse leukaemic monocyte macrophage (RAW) cells. The RAW 264.7 is a macrophage-like cell line derived from tumors induced in male BALB/c mice by the Abelson murine leukemia virus.

3.3.2.1 Murine Noroviruses

Murine noroviruses (MNV) are a small icosahedral non-enveloped viruses (28 to 35 in diameter). The viral genome is a positive single-stranded RNA of 7.382 nucleoids that contains open reading frames. These open reading frames encode non-structural polyprotein and the major (VP1) and minor (VP2) capsid proteins. The VP1 capsid protein of adeno-associated virus type 2 is carrying a phospholipase A2 domain required for virus infectivity [139]. VP1 and VP2 differ by the presence of a N-terminal extension in the minor protein VP1. The capsid encapsulates the genomic sDNA. Capsid proteins are responsible for the attachment to host cell receptor TFRC (transferrin receptor).

The viral genome is found in the capsid that contains 90 dimers of proteins [140]. The X-Ray crystallographic studies on noroviruses shows that each capsid constituted of an N-terminal arm (N), a shell (S) and a C-terminal (C) protruding domain[140, 141, 142]. The task of S domain is a formation of a shell that surrounds the viral genome. However, this shell is unable to bind to receptors. The radius of the shell is between 100 and 145 Å that can be extended until $\sim$ 190 Å due to the presence of prominent protrusion on the external surface of the shell [140]. The P domain generates arch-like structures on the capsid surface by dimerization. P domain is divided into two subdomains P1 and P2 which can provide the stability to capsid via intermolecular interactions. Additionally, the norovirus P2 subdomain involves sites for cell binding.

Murine noroviruses share many biochemical and genetic features with human noroviruses. Besides, the shape and size of murine norovirus are found similar to human noroviruses. The infection of a mice by murine norovirus was described for the first time in 2003 [143]. Furthermore, murine noroviruses can be transmitted from infected mice to uninfected one [138]. This indicates that murine norovirus spreads by faeco-oral way as human noroviruses. By considering the common features between murine norovirus and human noroviruses, the murine norovirus model system provides to understand human norovirus infection and the host reaction.

Prior to investigate the murine norovirus infection mechanism, we have firstly analyzed murine noroviruses in order to observe their morphological features. For this purpose, the murine norovirus strain CW1 was kindly provided by Herbert Virgin IV (Washington University, St. Louis, MO) and propagated by infecting 80% confluent monolayers of RAW 264.7 cells in D-MEM without FBS. Thereafter, murine noroviruses are collected from cells, purified and applied to Western blot analyses.

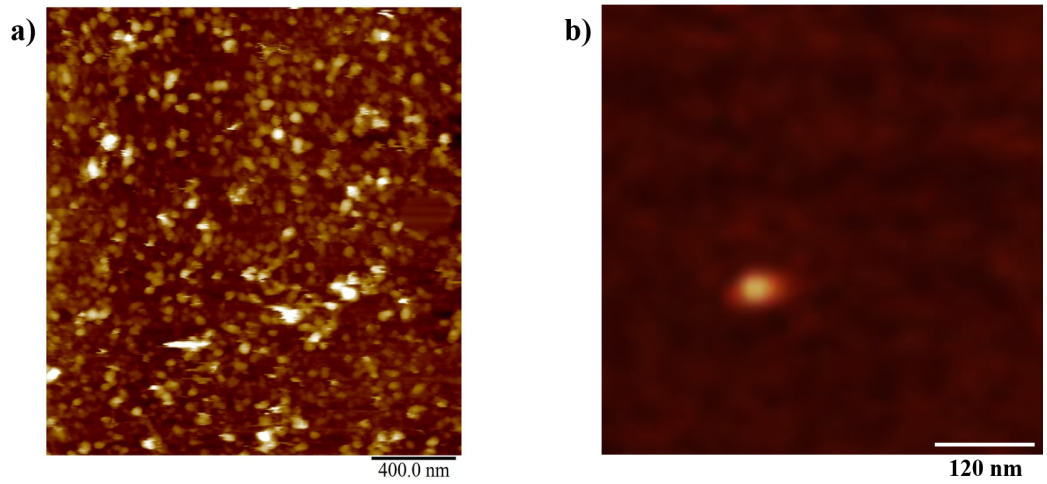

Fig. 3.7: (a) MNV imaged with oscillating contact mode in PBS medium by Multimode 8 microscope using DNP-S probe (k = 0.35 N/m - F = 50-80 kHz, Bruker). Scan size = 2 μm, scan rate = 1 Hz, amplitude = 99 mV, drive amplitude = 250 mV. (b) HS-AFM image of MNV observed in PBS with EBD tip attached Olympus AC-10 probe. Scan size = 600 nm, scan rate = 1.2 image/s, 128 $\times$ 128 pixels^2.

AFM and HS-AFM analyses were carried out in phosphate buffer saline (PBS) solution (pH 7.4 - Lonza, Levallois, France). The initial murine norovirus solution with $5\times10^{7.4}$ pfu/flasque concentration was directly deposited on freshly cleaved mica disk and incubated during five minutes. The AFM image of murine norovirus obtained with oscillating contact mode is presented in Fig.3.7.(a).

In this concentration, the surface of mica is overcharged, as seen from AFM image. Thus, we have diluted the initial solution 1000 times in order to obseve an isolated murine norovirus. The diluted solution was deposited on the mica surface in a similar way and implemented to HS-AFM analyses (Fig.3.7.(b)). However, any dynamics related to murine norovirus is observed. This is linked to the electrostatic interactions between murine noroviruses and the mica surface.

We have performed statistical analyses based on the AFM data to define the dimensions of murine noroviruses. Ten AFM images of three different murine norovirus samples were processed with Nanoscope (Bruker) software to measure the height and area of structures. The height and area histograms were plotted with OriginPro 8 and presented in Fig.3.8.(a) and (b), respectively.

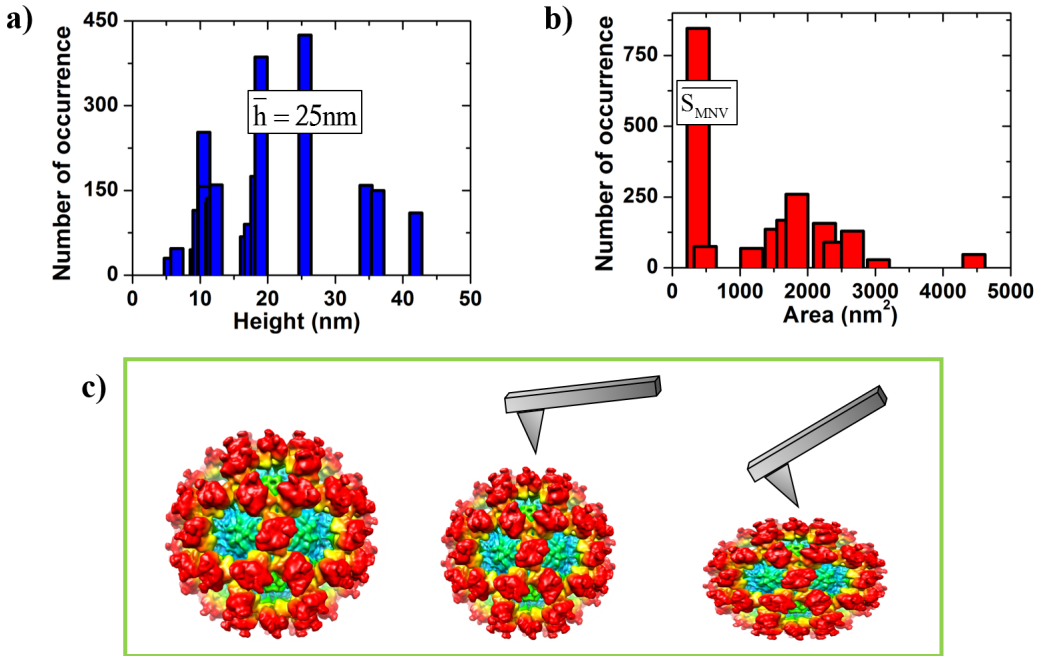

Fig. 3.8: (a) Height and (b) area histograms of MNV based on AFM data. c) Schematic representation of MNV deformation due to the applied forces by AFM tip.

According to the histogram results, the height and area of murine noroviruses are found 25 nm and 381 nm^2 ($\Phi \simeq 22$ nm), respectively. To prevent the deformation of murine noroviruses due to applied forces by tip, as presented in Fig.3.8.(c), a low amplitude value (99 mV) was maintained on a cantilever with small spring constant (DNP-S, k = 0.35 N/m - F = 50-80 kHz, Bruker). However, both histograms involve variations that is attributed the interaction between murine noroviruses and mica surface. Besides, we have observed a slight impact of the incubation time on the form of murine noroviruses. Thereby, we have defined five minutes as the optimal incubation time.

3.3.3 Mouse leukaemic monocyte macrophage (RAW) cells

Macrophages are a type of the white blood cell found in mostly all tissues. They discovered by Elie Metchnikoff in 1884.

The main task of macrophages is to help to defense mechanism, innate and adaptive immunity. They digest cellular debris and foreign substances. There are several type of macrophages and the totality of these cells named as *Mononuclear phagocyte system*. Macrophages are localized strategically in the body in order to defense the metabolism. Thus, they are classified in the function of their localization. For example, macrophages found in bone marrow and blood are called *monocyte* cells.

Macrophage cells are involved the study of the virus replications and the tumour targeting. Precisely, the murine norovirus infection on RAW 264.7 cell line and the change of cell morphology due to virus replication has been studied [137].

We have investigated the morphology of RAW 264.7 cells on the glass flask by AFM. The analyses were carried out in PBS medium. The AFM images are presented in Fig.3.9.

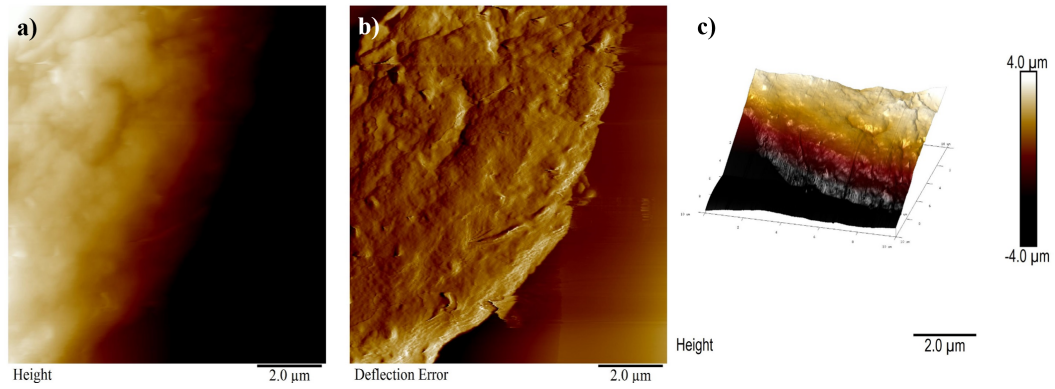

Fig. 3.9: RAW cell border imaged in PBS medium by MultiMode 8 with oscillating contact mode. (a) Topography, (b) deflection and (c) 3D AFM images.

AFM results indicate that RAW cells have a rough cell surface. Their surface roughness is found R $\backsimeq$ 480 nm (from more than 30 AFM images). Our aim is in this study to investigate the murine norovirus binding on RAW cell and accordingly caused topographic changes via AFM. However, to observe the structures in tens of nanometer (see Fig.3.7) on a surface with hundreds nanometer of roughness is meaningless. Therefore, we have decided to investigate the murine norovirus binding on the detergent resistant membrane domains of RAW 264.7 cells. The properties of detergent resistance domains are firstly presented and followed by experimental results.

3.3.4 Detergent Resistant Membrane domains

A cell is a building block for all living creatures. In addition to the outer membrane that results in the formation of a typical cell (this membrane is often referred to as the plasma membrane), cells contain intracellular membranes that serve distinct functions in the formation of various intracellular organelles, e.g. the nucleus and mitochondria. Biological membranes are the structures that define and control the composition of the space that they enclose. Membranes provide to transfer entities, information and energy between its compartments and act as a selective permeable barrier. All membranes exist as dynamic structures whose composition changes throughout the life of a cell.

Cell membranes are composed of lipid in bilayer form, protein and carbohydrate that exist in a fluid state. The lipid bilayer is a thin polar membrane made of two layers of lipid molecules. The carbohydrates of membranes are attached either to lipid forming glycolipids of various classes, or to proteins forming glycoproteins.

The lipid and protein compositions of membranes vary from cell type to cell type as well as within the various intracellular compartments that are defined by intracellular membranes. Protein concentrations can range from around 20% to as much as 70% of the total mass of a particular membrane. The lipids making up components of membranes are of three major classes that includes glycerophospholipids, sphingolipids, and cholesterol. There are approximately 5 $\times 10^6$ lipid molecules in a 1 μm $\times$ 1 μm area of lipid bilayer. The most abundant membrane lipids are the phospholipids.

All of lipid molecules in a cell membrane are amphipathic (or amphiphilic) -that means, they have a hydrophilic ("water-loving") or polar end and a hydrophobic ("water-fearing") or non-polar end. The hydrophilic head of phospholipids is found in the external part of leaflets contacting to intra or extra cellular compartments. On the other hand, the hydrophobic tails of two leaflets are face to face at the inner part of the membrane bilayer. Phospholipids have a polar head group and two hydrophobic hydrocarbon tails. The tails are usually fatty acids, and they can differ in length (they normally contain between 14 and 24 carbon atoms). One tail usually has one or more cis-double bonds (i.e. unsaturated), while the other tail does not (i.e. saturated). Each double bond creates a small kink in the tail. Differences in the length and saturation of the fatty acid tails are important because they influence the ability of phospholipid molecules to pack against one another, thereby affecting the fluidity of membrane.

Membrane bilayers can be found in the different phases determined by their fluidity. Accordingly, the fluidity of membrane depends on both its temperature and its composition (insaturation of hydrophobic tails at phospholipids and the concentration of cholesterol for example). Lipid molecules readily exchange places with their neighbors within a monolayer ($\sim 10^7$ times per second).

This gives rise to a rapid lateral diffusion, with a diffusion coefficient (D) of about 10^{-8} cm^2/sec, which means that an average lipid molecule diffuses the length of a large bacterial cell (~ 2 μm) in about 1 second.

A membrane bilayer changes from a liquid state to a two-dimensional rigid crystalline (or gel) state at a characteristic freezing point. From gel to fluid phase, the transition is characterized by melting temperature, T_m. In the gel phase, acyl chains of lipids are crystallized due to strong hydrophobic interaction. Although, lipids are dynamic and oscillating perpendicular to the membrane plan in the fluid phase. Therefore, a membrane domain is thinner when it is in the fluid phase. This change of state is called a *phase transition* and the temperature of transition is lower if the hydrocarbon chains are short or have double bonds. A shorter chain length reduces the tendency of hydrocarbon tails to interact with one another, and cis-double bonds produce kinks in the hydrocarbon chains that make them more difficult to pack together, so that the membrane remains fluid at low temperatures. The phase transition in phospholipid bilayers can be observed by atomic force microscopy [144]. For HS-AFM experiments, we have taken care of the laser diode power (minimize to 0.15 mW) to prevent increasing of the temperature above membrane.

The presence of cholesterol and sphingolipids results in intermediary phase, called as liquid ordered phase, that possess aligned acyl chains in gel phase and high mobility in the fluid phase. Cholesterol molecules enhance the permeability-barrier properties of the lipid bilayer. They orient themselves in the bilayer with their hydroxyl groups close to the polar head groups of the phospholipid molecules. In this position, their rigid, plate-like steroid rings interact with– and partly immobilize– those regions of the hydrocarbon chains closest to the polar head groups. By decreasing the mobility of the first few CH_2 groups of the hydrocarbon chains of the phospholipid molecules, cholesterol makes the lipid bilayer less deformable in this region and thereby decreases the permeability of bilayer to small water-soluble molecules. Although cholesterol tends to make lipid bilayers less fluid, it is mostly found at the high concentrations in eukaryotic plasma membranes.

Additionally, it prevents the hydrocarbon chains from coming together and crystallizing. In this way, it inhibits possible phase transitions.

Cell membranes contain domains that enriched in certain lipids, cholesterol and proteins but poor in docosahexaenoic acid (DHA). These domains are termed as *lipid raft* [145]. There is still controversy about their existence. However, they classified under three types; caveolae, glycosphingolipid enriched membranes (GEM) and polyphosphoinositol riched rafts. It may also be that there are inside rafts (PIP2 rich and caveolae) and outside rafts (GEM). Many functions, as cholesterol transport, endocytosis and signal transduction, have been attributed to rafts. The fatty-acid chains of lipids within the rafts tend to be extended and so more tightly packed, creating liquid ordered domains. It is therefore rafts are exist in a separate ordered-phase that floats in a sea of poorly ordered lipids. Their higher dynamic allows the movement of proteins and lipids in and out directions of the rafts. Conversely to non-rafts domains, the movement of each leaflet are dependent in raft domains since sphingolipids have longer hydrophobic tails.

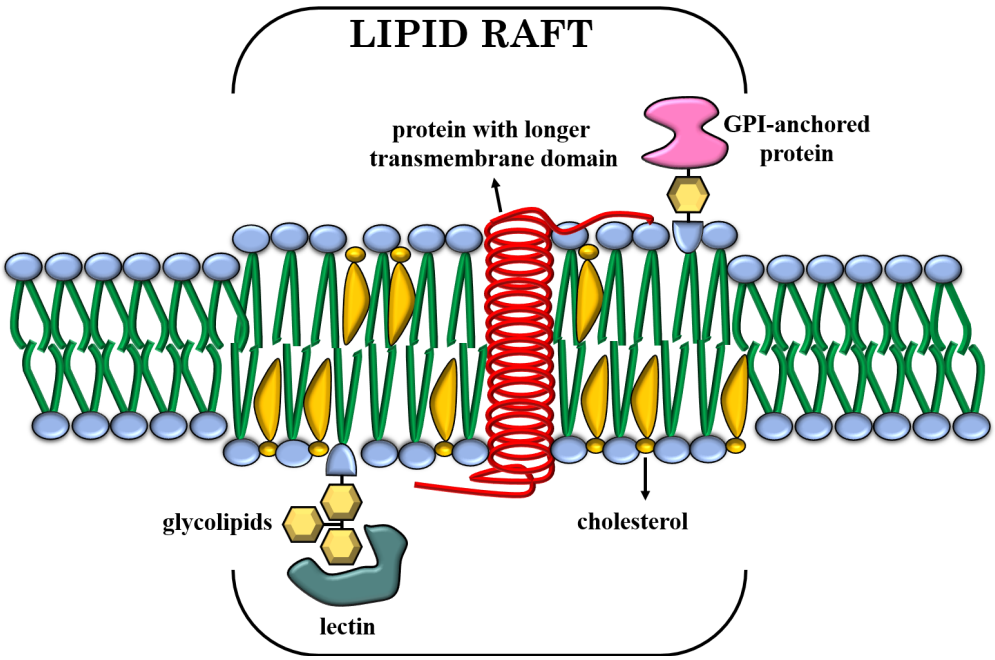

Fig. 3.10: Structure of lipid rafts.

Lipid rafts are formed by aggregation of specific lipids in the plane of membrane due to intermolecular interactions. These interactions involve van der Waals interactions between long saturated acyl chains of sphingolipids and glycosphingolipids and also hydrogen bonding between adjacent glycosyl moieties of glycosphingolipids. Additionally, the saturated lipids and glycolipids have ability to promote their interactions with cholesterol [146].

Cell surface proteins have tendency to bind into liquid ordered domains, preferentially into rafts. These proteins can be summarized by the glycosylphosphhatidylinositol (GPI) [147], the Src-family tyrosine kinases [148], hedgehog, heterotrimetric G proteins, phospholipid binding proteins [149], flotillins [150] and caveolins [151]. Figure 3.10 illustrates the structure of lipid rafts.

Lipid rafts can be found in a distinctive shape on the cell surface as flask-shaped invaginations. This specific shaped raft structure termed as *Caveolae* [152, 153]. Caveolae are generated from flat lipid rafts via the polymerization of caveolin, especially VIP21-caveolin. The caveolea structures are absent for lymphocytes and neuronal cells. VIP21-caveolin plays a key role on the formation of ceveolea that have been shown by injection of VIP21-caveolin to lymphocytes, which results the formation of invaginations on the membrane surface [154]. Furthermore, caveolin has crucial tasks as interaction with other membrane proteins, organization and equilibrate cholesterol [155].

Flotillins are specific to flat lipid rafts likewise caveolins for caveolae. The flats rafts and caveolae, these both types of rafts, contain different components as well as their morphology [148].

The tightly packed organization of sphingolipids and cholesterol in lipid rafts provides resistance to detergent applications. Therefore, they are known as *Detergent Resistant Membrane (DRM)* domains. Detergent resistant membranes can float at the low of density sucrose solution during centrifugation that provides to obtain isolated raft domains. However, the physical properties as the size of detergent resistant membranes can be affected by the type of used non-ionic detergent [148].

Since there is two kind of rafts, flat and caveolae, it is necessary to use flotillins and/or caveolin as a marker after detergent resistant membranes extraction to distinguish flat rafts and caveolea. Furthermore, they may aggregate easier than native rafts. The native rafts can be observed only on the membrane surface of the living cell [156]. Thus, the DRM facilities the biochemical and physical studies on lipid rafts.

3.3.5 Interactions between RAW DRMs and MNV: Preliminary study of MNV infection

We have investigated the murine norovirus binding on detergent resistant membrane domains of mouse leukaemic monocyte macrophage cells. In such biophysical studies, fluorescence microscopy and vacuum based characterization techniques have been widely used [142, 139, 157, 158]. Our aim was to detect the direct interactions between the detergent resistant membrane domains and virus without harming the natural form of the samples or involving a marker. Atomic force microscopy (AFM) have already been used to achieve the topography of lipid rafts, supported bilayers, DRMs and viruses in liquid mediums [144, 156, 159, 160]. On the other hand, surface enhanced Raman spectroscopy (SERS) is a prominent chemical characterization technique has been increasingly implemented to biomolecule investigations in the field of chemistry, physics, biological science and medicine. Its efficacy has been proved by performing complex biomolecule investigations such as nasopharyngeal cancer detection [161], the observation of prion protein expressions in cell membrane [162] and the chemical modifications in bacteria cell wall due to antibiotics [163]. In this study, the murine norovirus detection on detergent resistant membranes was carried out with real time polymerase chain reaction and surface enhanced Raman spectroscopy. To validate data, we correlated these results with the topographical features obtained from atomic force microscopy and high-speed atomic force microscopy.

The real-time polymerase chain reaction (RT-PCR) is a detection and quantification technique based on the targeting of DNA or RNA molecules. We have used this laboratory technique to detect MNV in order to investigate the MNV binding on RAW DRMs.

We have prepared four samples prior to RT-PCR analyses :

- Detergent resistant membranes (DRMs) of leukaemic monocyte macrophage (RAW) cells,
- Methyl-beta-cyclodextrin (MβCD) treated RAW DRMs,
- Murine norovirus infected RAW DRMs,
- Murine norovirus infected MβCD treated RAW DRMs.

The preparation process of each sample is simply visualized in Fig.3.11.

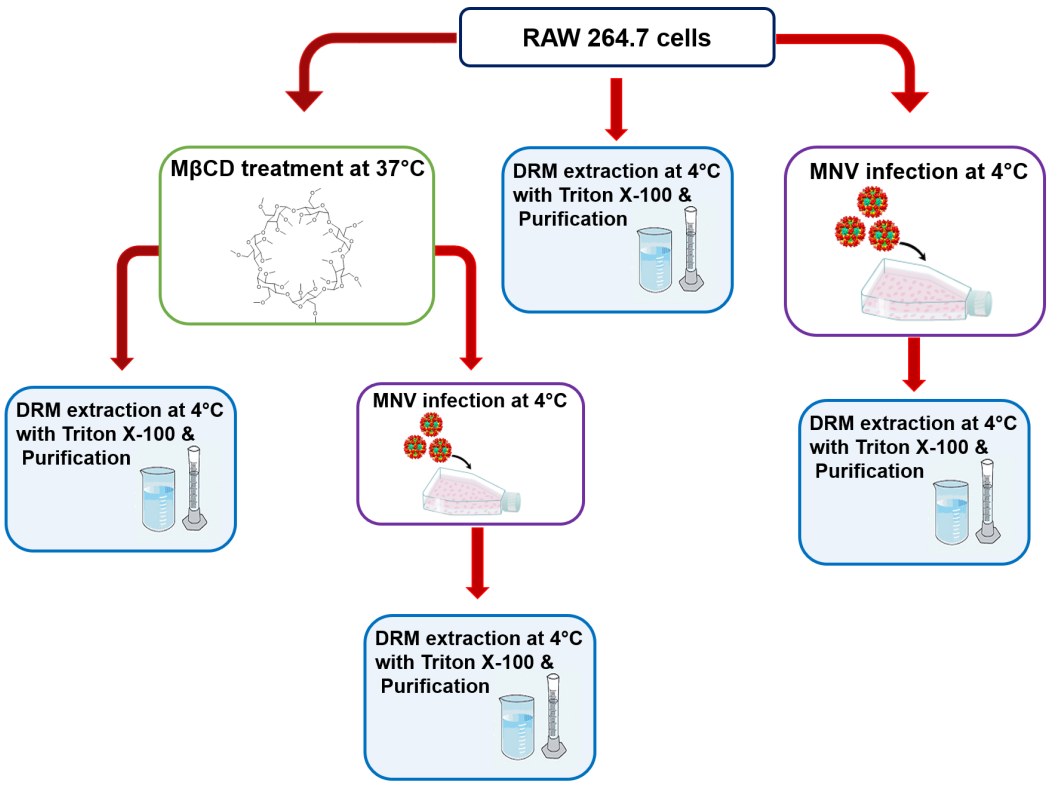

Fig. 3.11: Schematic presentation of the preparation process of the samples. *Graphic image of MNV is obtained from reference* [162] *with permission of authors.*

The preparation procedure of each sample is described by following paragraphs.

The extraction of detergent resistant membrane domains from RAW 264.7 cells was carried out by a detergent treatment at the low temperature. The DRM purification was performed by ultracentrifugation onto a sucrose gradient. The Western blot technique was applied to DRM-sucrose solution. The cholesterol was used as marker of the DRMs and measured by fluorometry (Amplex® Red Cholesterol Assay Kit from Life Technologies). The cholesterol measurements on RAW DRMs is given in Fig.3.12.

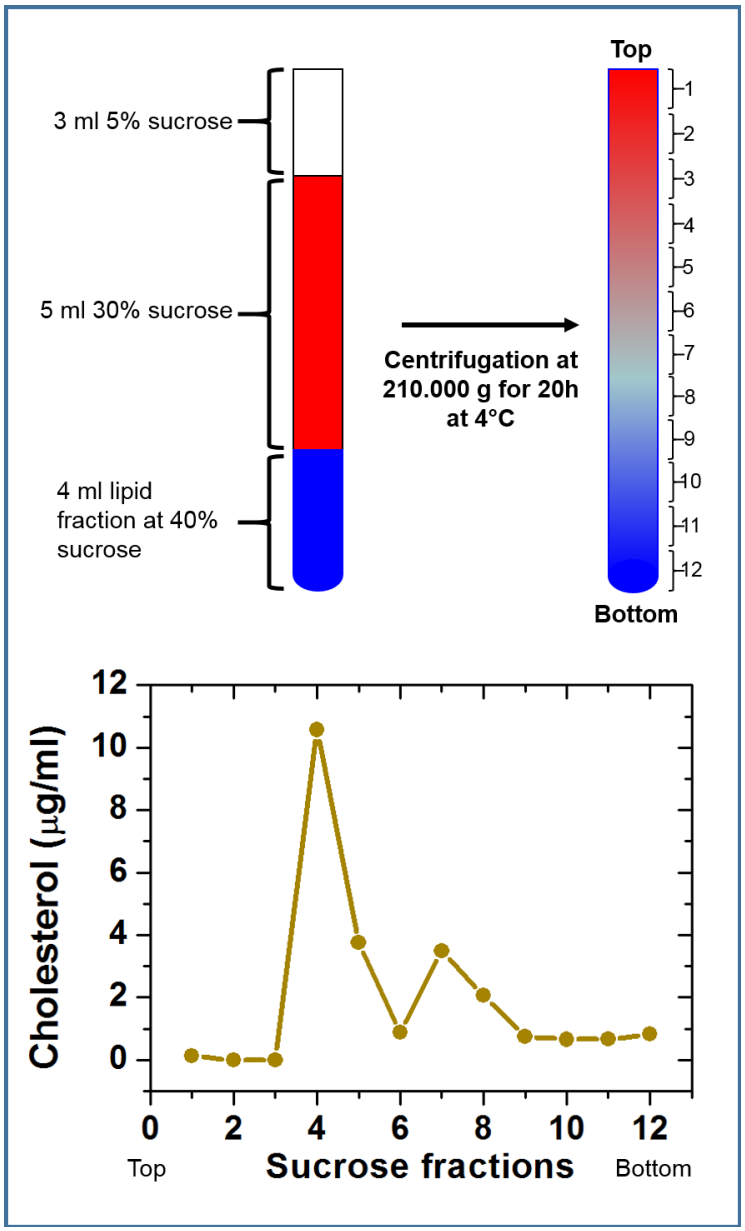

Fig. 3.12: Schematic presentation of the preparation process of the samples.

Cholesterol concentration was given in μg/ml and the highest amount of cholesterol is found at the 4th fraction that is considered as the DRM-enriched fraction. The cholesterol measurements were carried out periodically after each DRM extraction process.

The murine norovirus infection of RAW cells carried out after washing of the cells with Phosphate Buffer Saline (PBS) pH 7.4 (Lonza, Levallois, France) and incubating for 1 hour at 37 ℃ with DMEM base. For each flask, the cells were inoculated with $5 \times 10^{7.4}$ plaque forming units (pfu) of MNV in a total volume of 10 ml. Then the cells were placed at 4 ℃ for 1 hour to prevent virus internalization. At this stage, the cells were twice washed with cold PBS and directly used for DRM extraction.

Methyl-beta-cyclodextrin was used for increasing the solubility of non-polar substances, in our case it was cholesterol. Methyl-beta-cyclodextrin (MβCD) is a compound consist of sugar molecules. MβCD has a rigid doughnut-shaped structure and cholesterol can be lodged inside. Since cholesterol is one of the main component of rafts, MβCD treatment break downs the raft structure.

Before the methyl-beta-cyclodextrin implementation, the cells were washed with PBS and incubated with DMEM media. Afterwards, the media was replaced with 15 ml per flask of DMEM base containing 20 mM of MβCD and incubated for 1 hour at 37 ℃. The cells were inoculated with murine norovirus and immediately placed at 4 ℃ for 1 hour.

Following DRM purification, RNA was extracted from 100 μl of each fraction using a Nuclisens Easy MAG system (bioMérieux, France) according to the manufacturer's instructions. RNA was eluted in a final volume of 50 μl and used for NoV molecular detection. Detection of the murine norovirus viral genome was performed using taqman technology. Five microliters of RNA was used for real-time RT-PCR as described previously [135]. The experiments were performed in triplicate.

The copy number of the murine norovirus genomic RNA was determined by plotting the threshold cycle values of each sample on a standard curve generated with serial dilutions of a known quantity of a plasmid containing the full-length cDNA of the MNV strain CW1 (kindly provided by H. Virgin IV).

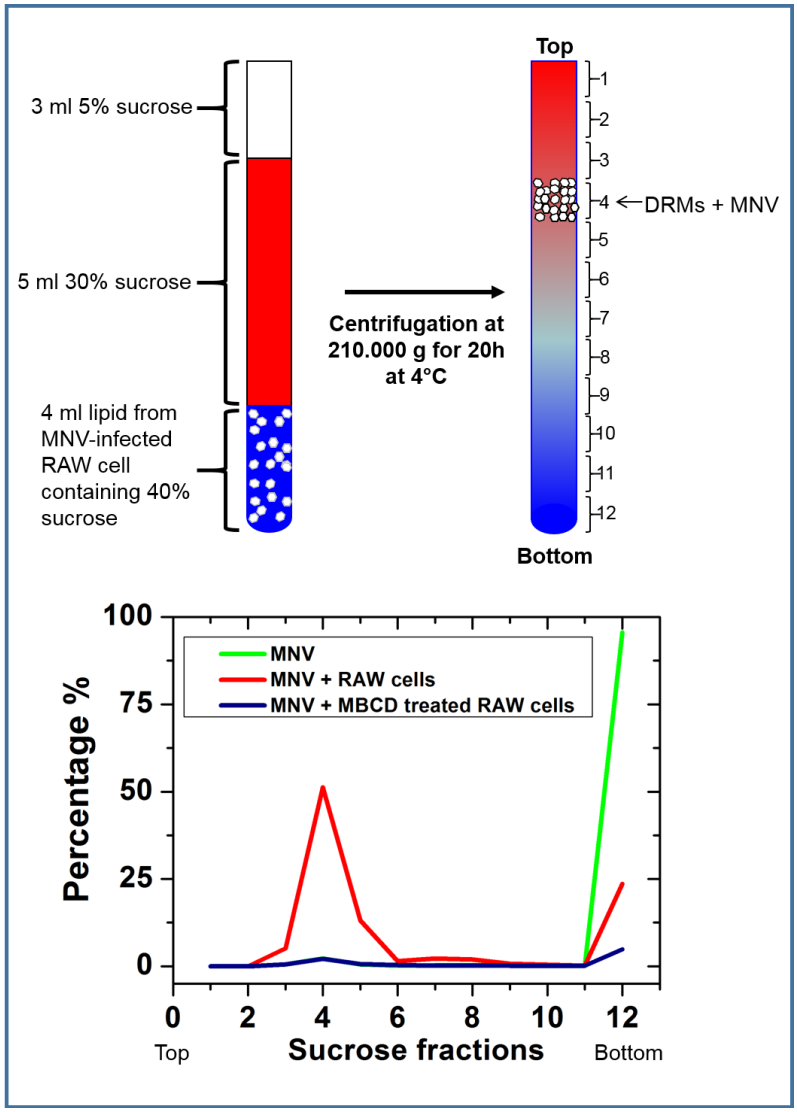

Fig. 3.13: RT-PCR results for MNV detection. MNV alone in sucrose solution (pink line), on infected RAW DRMs by MNV (dark red line), pre-treated RAW DRMs by MβCD followed by MNV infection (purple line).

Figure 3.13. displays the MNV detection on 12 fraction of (i) MNV - sucrose solution, (ii) the infected RAW DRMs by MNV and (iii) the MβCD treated DRMs infected by MNV.

(i) The 12th fraction of MNV-sucrose was found as the richest fraction in MNV regarding the RT-PCR results. This indicates MNVs are relatively heavy and sink to the bottom of MNV - sucrose solution.

(ii) The MNV binding on RAW DRMs was investigated by RT-PCR and plotted in Fig.3.13. For this analysis, the DRM extraction was carried out on the MNV inoculated cells. According to the RT-PCR results, more than 60 % of MNV was found at 4th fraction of DRMs. This fraction was found rich in lipid rafts, depending upon previous cholesterol measurements. The fact that MNVs were found at lipid raft region, we have assumed that the presence of DRMs promotes the MNV attachment.

(iii) To ensure that the MNV binding depends to the presence of DRMs, we pre-incubated the cells with MβCD prior to the MNV inoculation. The RT-PCR results of this sample is plotted with a purple line in Fig.3.13. Consequently, almost any MNV was detected at all fractions of this sample. These results indicate that DRMs are involved to the MNV binding, furthermore this attachment is cholesterol dependent.

3.3.6 AFM analysis of RAW DRMs - MNV interactions

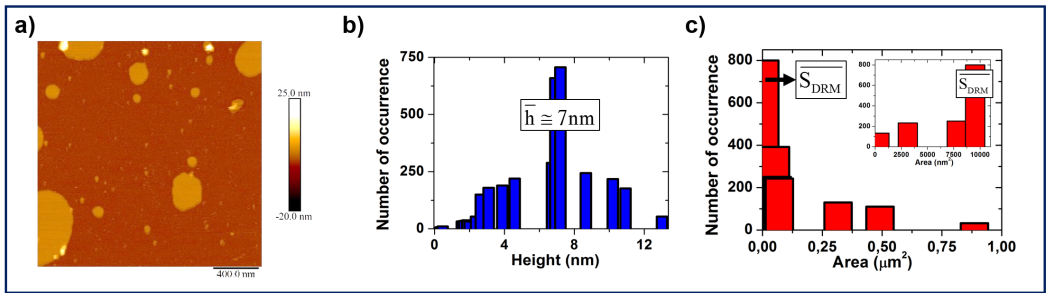

Fig. 3.14: (a) AFM image of RAW DRMs. Scale bar is 400 nm. (b) Height and (c) area histograms of presented sample.

We have first investigated the detergent resistant membrane domains and murine noroviruses by atomic force microscopy (AFM) in order to determine their morphological features.

A commercial AFM (Bruker Dimension FastScan) in FastScan Bio tapping mode has been used with FASTSCAN-D probe (k = 0.25 N/m - F = 110 kHz, Bruker) to discriminate the virus, membrane and substrate. The AFM images with corresponding height and area histograms are given in Fig.3.14.

The average height and surface area of RAW DRMs were 7.2 ± 0.2 nm and 9500 ± 550 nm^2 (with approximate diameter of ∼ 100 nm), respectively. Membrane rafts are flat structures and they are found at various heights. The height histogram presents the structures with over 8 nm of thickness, those are considered as micelle. The maximum surface area of DRMs reaches to 0.75 μm^2. These characteristic parameters of membrane domains vary in function of the cell type and the detergent treatment. The thickness of DRMs as well as the diameter are strongly influenced by the components such as GM1, cholesterol and the type of lipid [164, 165, 166].

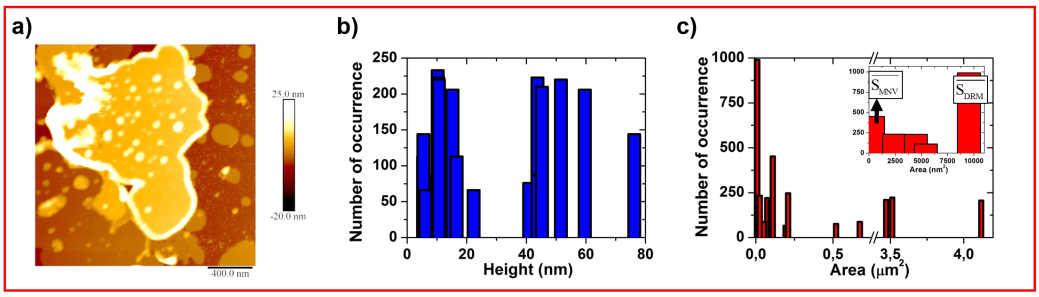

Fig. 3.15: (a) AFM image of MNV infected RAW DRMs. Scale bar is 400 nm. (b) Height and (c) area histograms of presented sample.

RAW cells were incubated with murine norovirus inoculum prior to detergent resistant membrane domain extractions. The topography of the infected DRMs were shown in Fig.3.15. A significant change in topography was observed compared with the DRMs sample (Fig.3.14). The area histogram contains a large population at 380 nm^2 that corresponds to the size of MNV, as defined previously (Fig.3.8). The presence of MNV provokes the aggregations of RAW DRMs resulting large structures with area up to 4 μm^2.

Dynamics of detergent resistant membrane domains of RAW cells as well as the aggregation of DRMs in the presence of murine noroviruses have been observed using FastScan Bio tapping mode (Dimension FastScan AFM, Bruker) with FASTSCAN-D probe (k = 0.25 N/m - F = 110 kHz, Bruker). The successive AFM images at Fig.3.16 present (a) mobility of DRM domains and (b) dynamics of DRMs aggregation.

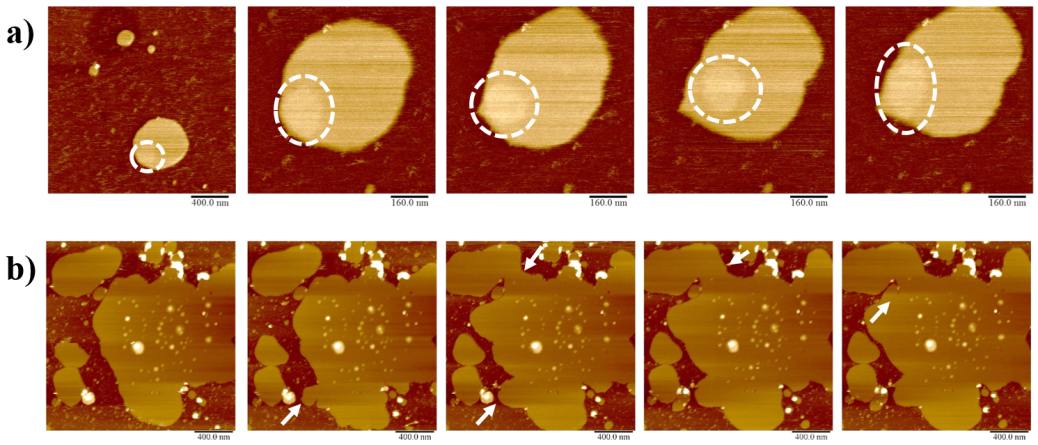

Fig. 3.16: AFM image of (a) RAW DRMs and (b) MNV infected RAW DRMs.

RAW DRMs can contain a specific area on itself that has higher dynamics then rest of the structure. These areas are highlighted by circles on the upper image series of Fig.3.16. We associated these highly dynamics areas to a DRM fraction where the glycosphingolipids have longer sugar residues. Since a chemical identification on this area on the moment of analysis was absent, thus it remains as a hypothesis. However, we visualize this scenario in Fig.3.17.

The RAW DRM presented in Fig.3.16 has $\sim$ 6.5 nm thickness and the circled area is $\sim$ 1 nm thicker than the rest of structure. As it has mentioned before that, lipid raft derived DRM structures involve a high concentration of sphingolipides.

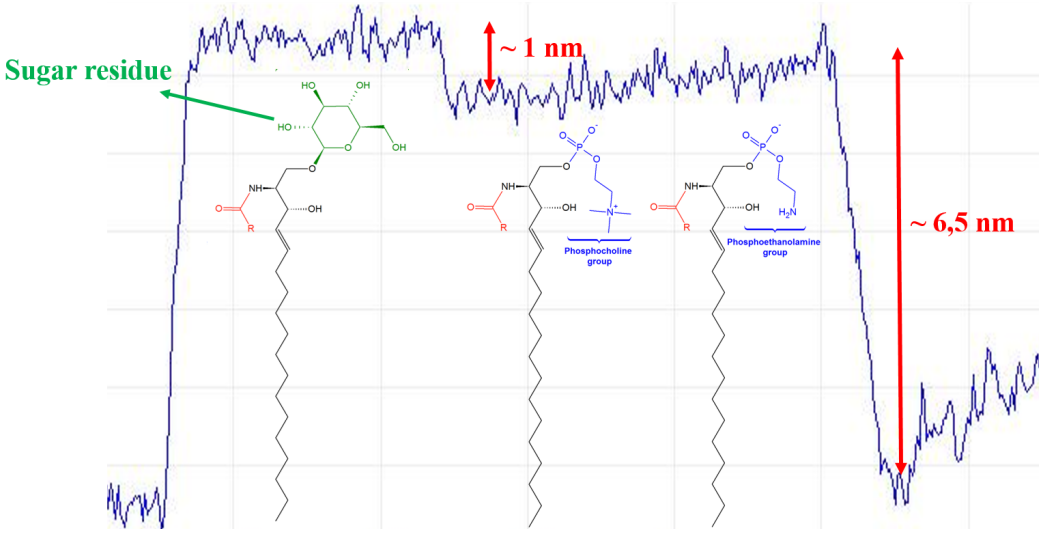

Fig. 3.17: The section image of RAW DRM presented in Fig.3.16.(a).

Among sphingolipides, glycosphingolipides and gangliosides include sugar residues. More precisely, glycosphingolipides contains one ore more sugar residues while gangliosides has at least three of them and one of which must be sialic acid. Therefore, we assume that the height difference of the circled area comparing with the rest of sturcture is due to sugar residues.

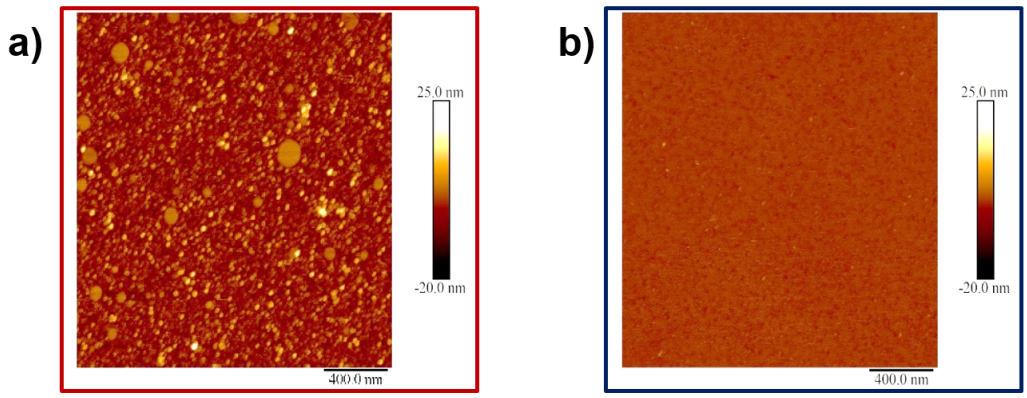

Fig. 3.18: AFM images of MβCD treated (a) and thereafter MNV infected RAW DRMs. Scale bars are 400 nm.

The AFM image of methyl-beta-cyclodextrin treated RAW DRMs is given in Fig.3.18.(a).

The area of detergent resistant membrane domains decreased from 9500 ± 550 nm^2 to 872 ± 100 nm^2 due to the methyl-beta-cyclodextrin treatment. Furthermore, MNV incubation was performed on RAW cells prior detergent treatment (Fig.3.18.(b)). The AFM image presents absence of structures on the mica surface including both detergent resistant membrane domains and murine noroviruses. This result indicates that murine norovirus binding on detergent resistant membrane domains is precluded by the MβCD treatment.

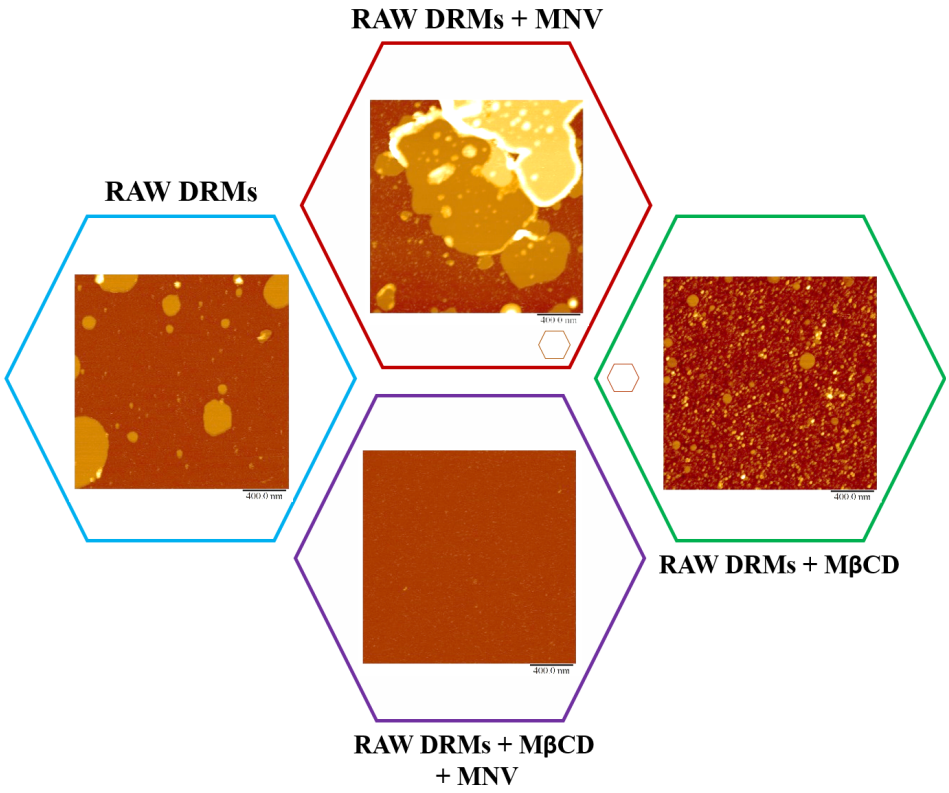

Fig. 3.19: AFM images of RAW DRM samples.

We have summerized the AFM study of RAW-MNV interactions in Fig.3.19. RAW DRMs are flat structures and found at $\sim$ 7 nm height and $\sim$ 100 nm diameter. Incubation of RAW cells with murine noroviruses prior to DRM extraction provokes aggreagation DRMs on mica surface. Concequenlty, the diameter of stuctures can reach to several micrometers.

In order to validate that the aggregations are caused by RAW DRMs – MNV interactions, we have analyzed MβCD treated cells. AFM results indicates that following of MβCD treatment the MNV binding is absent. Since MβCD treatment incapsulates cholesterol, we conclude that MNV binding is cholesterol dependent.

3.3.7 Detection of murine norovirus binding on RAW cells by SERS analysis

Concerning previously presented RT-PCR and AFM results, the murine norovirus binding is closely associated to the presence of detergent resistant membranes of RAW macrophage cells and it has found cholesterol dependent. Therefore, we applied surface enhanced Raman scattering experiments in order to obtain the chemical information about MNV infection. For that, SERS analyzes are performed on the gold GDC nanoparticle substrate via excitation at 785 nm laser light. The spectra are collected from each sample with 10 s acquisition time and presented in Figure 3.20.

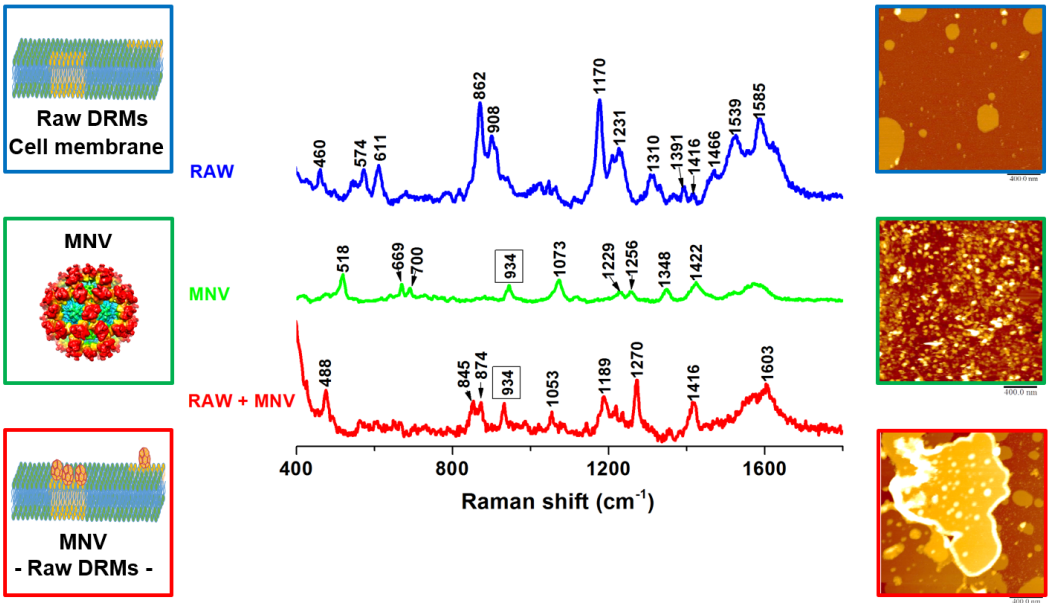

Fig. 3.20: SERS spectra of detergent resistant membrane domains (DRMs) of RAW cells, MNV and MNV infected RAW DRMs. *Graphic image of MNV is obtained from reference* [162] *with permission of authors.*

Here, we investigate the chemical evidence of the murine norovirus binding on detergent resistant membrane domains of RAW cells. SERS spectra of murine norovirus inoculum and detergent resistant domains were first acquired separately (Fig.3.20). SERS spectrum of RAW DRMs consist of signals from lipids, cholesterol and proteins which are the main components of lipid rafts. The Raman bands at 574 cm^{-1}, 862 cm^{-1} and 1539 cm^{-1} were attributed to phosphatidylinositol [167], phospholipid [168] and lipids [169], respectively. The peak at 1310 cm^{-1} was found as associated to CH_2 deformations in lipids/adenine/cytosine[168] and ring stretching/twisting of CH_2, CH_3 in proteins [170]. Spectral feature of cholesterol ester was found at 611 cm^{-1} [167]. The presence of proteins in RAW DRM was confirmed with the peaks at 1231 cm^{-1} [170], 1391, 1416 and 1585 cm^{-1} [171]. The Raman band at 1170 cm^{-1} was linked to presence of fatty acids [167] or proteins [169, 171]. In addition, the peaks at 460 cm^{-1}, 908 cm^{-1} and 1466 cm^{-1} were observed at SERS spectrum of RAW DRMs but they are undefined due to leak of data in literature.

Spectral features of partially purified murine norovirus inoculum from infected cell lysate are shown in Fig.3.20. It has already known that SERS spectrum of viruses contains Raman bands associated to nucleic acids, proteins, lipids and carbohydrate [172]. However, MNV is a non-enveloped virus where the lipid bilayer envelope is absent, therefore it doesn't contain any lipids. We have observed a peak at 934 cm^{-1} that has defined as characteristic Raman band of MNV-4 [173]. MNV-1 and MNV-4 shares many sequences, thus we assume that it indicates the presence of MNV-1. The Raman bands acquired at 1229 cm^{-1} and 1256 cm^{-1} are linked to spectral features of proteins [171, 174]. The peak at 1348 cm^{-1} corresponds to Raman band of carbohydrate while the band at 1422 cm^{-1} is associated with adenine/guanine [171] that indicates the presence of RNA.

The SERS spectrum of the murine norovirus infected detergent resistant membrane domains of RAW cells is displayed in Fig.3.20. The presence of lipids is verified with two peaks at the spectrum. The Raman band at 874 cm^{-1} is attributed to phosphatidylcholine/sphingomyelin [167] while the peak at 1053 cm^{-1} is linked to lipids [168].

Spectral feature of unsaturated fatty acids [167] is observed via the peak at 1270 cm^{-1}. The murine norovirus binding on RAW DRMs is confirmed with the band at 934 cm^{-1} which is a specific Raman band of MNV [173] and previously observed at the SERS spectrum of MNV. In addition, the peak at 1189 cm^{-1} corresponds to nucleoids: base RNA [171]. Two Raman bands, at 1270 cm^{-1} and 1416 cm^{-1}, correspond to proteins [168, 171]. The peak at 1270 cm^{-1} can be originated from the capsid proteins of MNV or the membrane proteins. However, 1416 cm^{-1} is associated the membrane proteins since it has been observed also at the SERS spectrum of RAW DRMs. The Raman band at 845 cm^{-1}can be attributed to saccharide [167] that indicates a remaining residue after sucrose fraction.

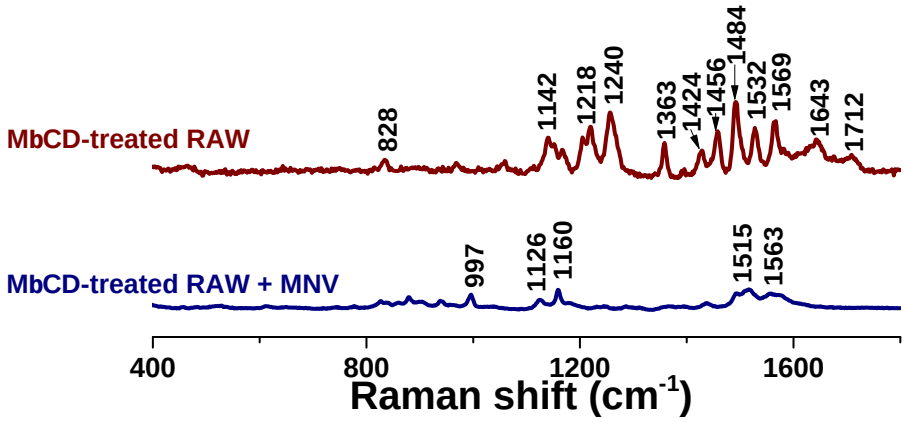

Fig. 3.21: SERS spectrum of MβCD-treated RAW DRMs and MβCD-treated and MNV incubated RAW DRMs.

In order to verify the previous results yielded from the specific interaction between detergent resistant membranes of macrophage cells and MNV, the methyl-beta-cyclodextrin (MβCD) treatment was implemented to cells before to the detergent treatment. The SERS spectrum of the samples are displayed in Fig.3.21. A remarkable spectral change is observed for the SERS spectrum of MβCD-treated RAW DRMs compared with DRMs alone (Fig.3.20).

The Raman bands at the spectral range of 400 – 1100 cm^{-1} are disappeared including the cholesterol ester assignment at 611 cm^{-1}. The spectrum contains the peaks at 1142 cm^{-1} (ribose-phosphate DNA [171]), 1218 cm^{-1} (protein [175]), 1240 cm^{-1} (amide III [176]), 1363 cm^{-1} (hemoglobin protein [171] or saturated lipid [[170]]), 1456 cm^{-1} (phospholipid [177]) and 1643 cm^{-1} (lipid [168] or protein [171]). On the other hand, the spectra of MβCD-treated and MNV incubated RAW DRMs contains a few peaks at low Raman signal intensity. The decrease of Raman signal correlates to AFM results since the intensity of Raman signal is influenced by the quantity of analyte. The spectrum contains spectral features of protein by the peaks at 997 cm^{-1} [168, 171], 1160 cm^{-1} [174] and 1566 cm^{-1} [171]. The Raman band at 1126 cm^{-1} is associated to fatty acids [167]. However, both MβCD-treated samples own a band at 828 cm^{-1} that associated to tyr protein [171].

Bands (cm^{-1})	Assignments				
	RAW	RAW+MNV	RAW+MβCD	RAW+ MβCD+MNV	MNV
574	Phosphatidylinositol				
611	Cholesterol ester				
828			Tyr protein		
845		Saccharide			
862	Phospholipid				
874		Phosphatidylcholine or sphingomyelin			
934		**MNV4**			**MNV4**
993				Protein or protein amide III	
1053		Lipid			
1142			Ribose-phosphate DNA		
1170	Fatty acid or protein				
1189		Nucleoids: base RNA			
1218			Protein amide III		
1231	Protein amide III				
1270		Unsaturated fatty acid			
1310	Lipid or protein				
1363			Saccharide		
1391	Protein				
1416	Protein				
1456			Hemoglobin protein or saturated lipids		
1539	Lipid				
1603		Protein			
1643			Lipid or protein amide I		

Fig. 3.22: Enhanced Raman bands of RAW DRMs obtained from SERS spectra shown in Fig.3.20 and 3.21.

Consequently, we could identified the characteristic Raman peaks of detergent resistant membrane domains of RAW macrophage cell line and observed the chemical modification caused by murine norovirus and methyl-beta-cyclodextrin. After methyl-beta-cyclodextrin treatment, absence of cholesterol is observed. We have observed that the murine norovirus infection occurs only in the presence of the detergent resistant membranes of RAW macrophage cell line and it is cholesterol dependent.

3.3.8 Human intestinal cells

Human intestinal cells are the target for noroviruses to contract gastroenteritis disease. Here, we have investigated the interactions between *Virus Like Particles (VLP)* and *human colon carcinoma cells (Caco–2)* to reveal gastroenteritis disease at human hosts. This study is a continuation of the previous work and carried out in collaboration with INSERM Research Centre UMR866.

Caco–2 cells are cultivable and can differentiate into specialized cells once they reach to confluence. These cells are studied for drug delivery and intestinal infections.

The apical side of Caco–2 cells, they harbor *Microvillus*. Microvili are membrane protrusions that increase the membrane surface without arising the volume. They have many functions as absorbtion, secretion and adhesion. The size of microvilli depends the incubation time of cell cultivation. Microvilli, whatever their size, include organelles. Generally, microvili consist of actin filaments that is the core of structure. Inside of microvilli, 20 to 30 actin filaments can be found bundled. Additionally, some proteins as fimbrin, villin and espin attach to actin filament bundle. The glycocalyx surrounds whole external surface of the microvilli, consisting of peripheral glycoproteins. This layer aid to bind the substances and act as protection.

In first, Caco–2 cells were analyzed alone by atomic force microscopy to obtain their topography. Prior to AFM analyses, cells were cultivated during 3 weeks in DMEM medium with 4.5 g/l of glucose, glutamine, non-essential amino acids and 10 % foetal calf serum. First, the cells were implanted on glan disk cell plates.

Once the cells reached to confluence, they were maintained in the culture over three weeks to obtain a complete differentiation into enterocyte of the cell monolayer. The monolayer was then rinsed of with PBS prior to fixation with 4 % paraformaldehyde (PFA). The cell plates were stored at 4℃ until AFM analyses.

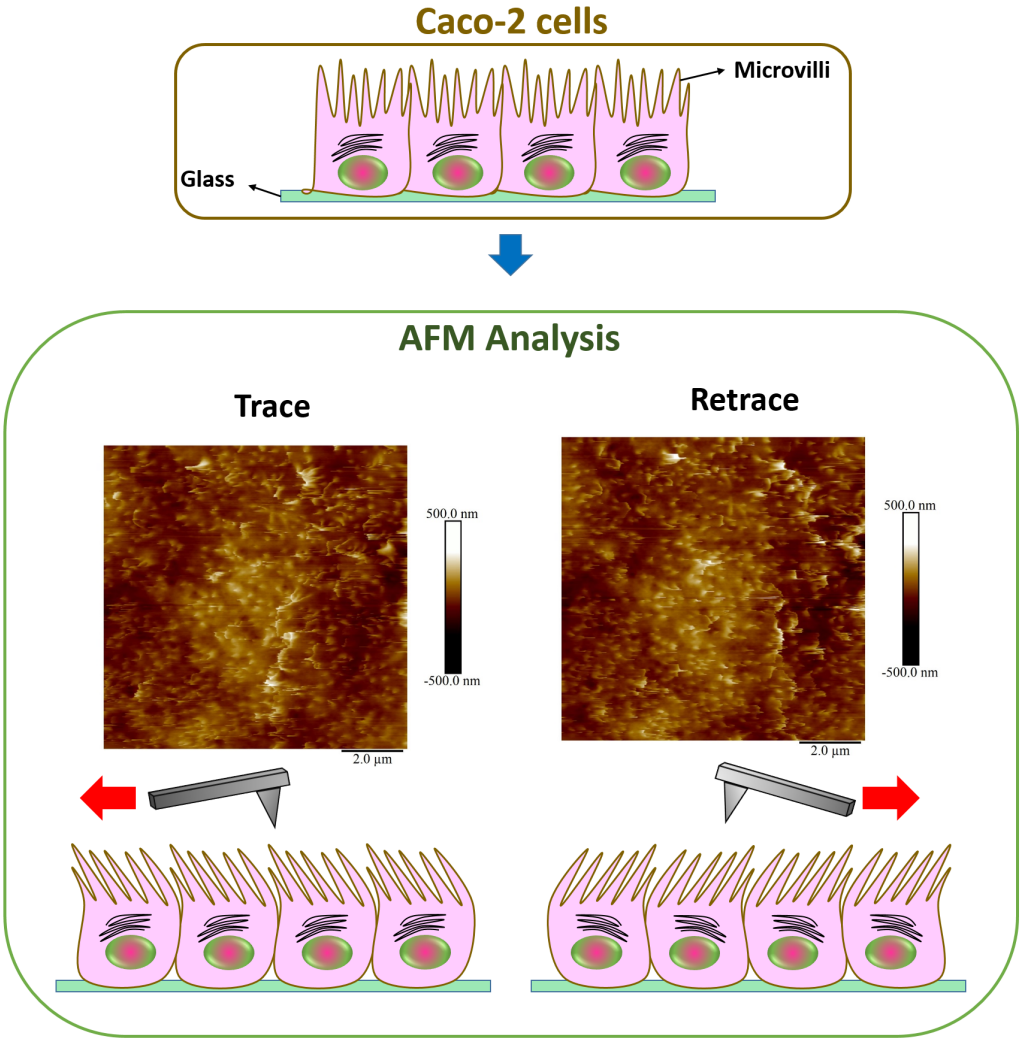

Fig. 3.23: Schematic drawings of Caco–2 cells on a glass surface. AFM images of Caco–2 cells are presented. Scale bars are 2 μm. The dragging effect due to scanning is shown at the bottom part.

AFM experiments were carried out on Multimode 8 microscope in PBS medium. No results have archieved by using neither oscillating contact nor Peak Force QNM modes. We obtained the topography of cells only by contact mode.

Figure 3.23 presents a schematic presentation of Caco–2 cells with typical topography images in both scanning directions. AFM images were obtained with 0.5 Hz of scan rate and 15.3 mV of deflection setpoint.

The trace and retrace images of Caco–2 cells are not identical, as seen from Fig. 3.23. Some structures on the cell surface –we assume that they are microvilli– are oriented in the same direction with scanning. However, it is not possible to avoid this dragging effect caused by AFM tip even for very low applied force values (a few pN).

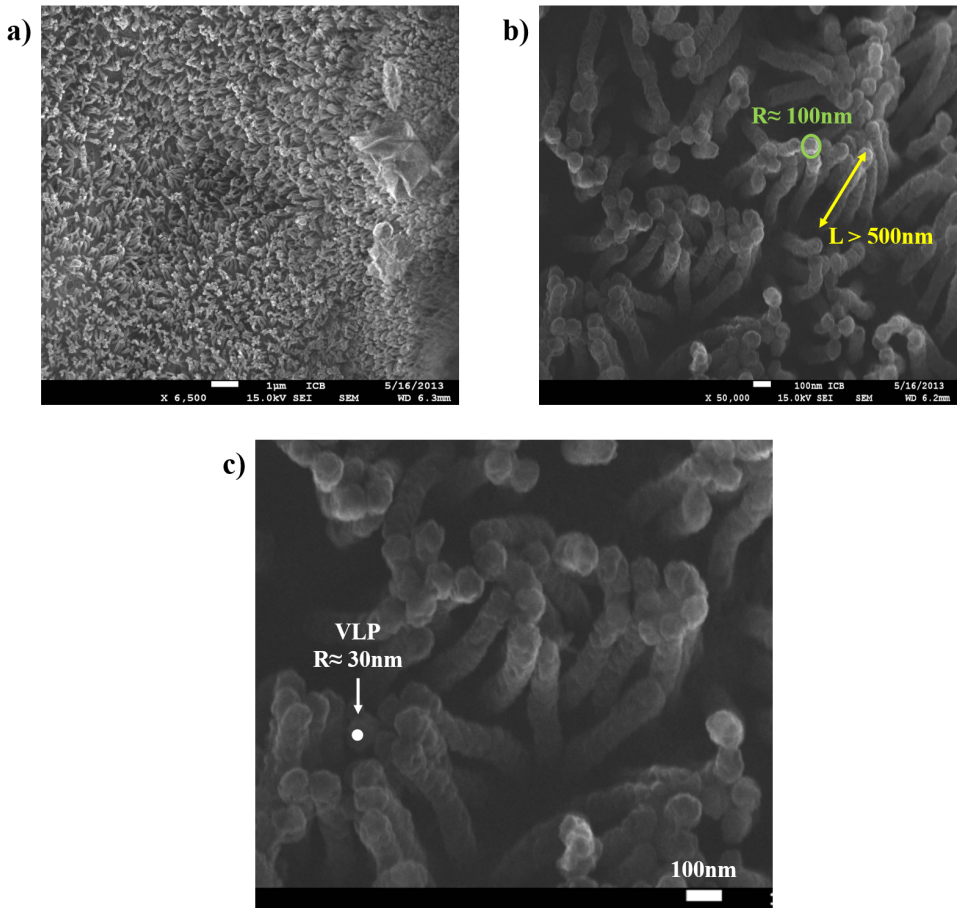

Fig. 3.24: Scanning electron microscopy images of Caco–2 cell surface. (a) Magnitude: × 6500, scale: 1 μm and (b,c) magnitude: × 50000, scale: 100 nm.

In order to observe the cell surface without any dragging effect, Caco–2 cells were imaged by scanning electron microscopy. Figure 3.24 presents SEM images of the cell surface in two different magnification levels.

SEM results indicate that the entire Caco–2 cell surface was covered by microvilli. Their diameter and length are around 100 nm and 500 nm, respectively. These structures obstruct AFM imaging process since they are pushed and dragged by tip during scanning. Another important issue is their size that is very large compared with VLP. Figure 3.24.(c) is a focus on microvilli, which highlights the size difference between VLP and microvilli. VLP has drastically small size compared with these membrane protrusions that complicates observing them on the cell surface by AFM technique. Therefore, we have implemented several approaches including $CuSO_4$ treatment that transforms the actin filaments (F-actin) to globular actin (G-actin). However, the cell surface still remains enough roughness that obstructs to observe VLP. Consequently, our investigations were hampered by the presence of microvilli and we claim that one successful approach can be use of fluorescent labelling for this work.

3.4 Conclusion

In this chapter, we have carried out three studies in order to evaluate the compability of atomic force microscopy and surface enhanced Raman spectroscopy. Likewise, we aimed to observe efficacy of our nanoparticle substrates for complex biological systems. Our studies can be classified under three categories:

- **Detection of a complex biomolecule :**

A membrane-bound hemoprotein derived from human microsomal cytochrome b5 was investigated by SERS measurements. The reference samples for SERS analysis have generally small and simple molecules that yield large Raman signal intensity and well-defined spectral features. However, native biological samples consist of several components and they generally yield small amount of Raman signal. Therefore, we have firstly implemented our nanoparticle substrates to a complex biomolecule analysis in order to evaluate the sensitivity and efficacy of substrates. The chemical signature of the protein was achieved in nanomolar concentration and the peak positions at the Raman spectra were confirmed with the literature.

• **Observation of conformational changes of a protein :**

Our aim was to observe the conformational changes of a protein with SERS and HS-AFM techniques afterwards correlate both topographic and chemical data. For this purpose, we have analyzed Leuconostoc oenos (Lo 18) protein that involved a popular regional topic: the quality and stability of wine. Lo 18 is a small heat shock protein that can form large oligomers, in other words it can change its conformation in the function of pH level. We have investigated Lo 18 protein at three pH levels and we determined experimentally the number of its sub-units and the velocity of dimers by HS-AFM analysis. In parallel, related chemical features were investigated by SERS measurements on the nanoparticle substrates with 1 s acquisition time to have comparable dynamics with HS-AFM results. Varying the concentration of protein solutions, we have distinguished the spectral features of dimers from higher oligomeric conformations.

• **Detection of chemical variations due to interactions :**

At the last part of this chapter, we have focused on the detection of chemical variations originated from virus–membrane interactions. Again, gastroenteritis is a regional topic and we have studied a model system that can help to understand the infection mechanism of disease. We have investigated the topographic features of murine noroviruses, host cells, the detergent resistant membrane domains of host cells and their interactions between each other by HS-AFM. Our preliminary studies with RT-PCR technique suggest that the virus binding involves lipid raft derived structures and the binding is cholesterol dependent. To ensure these data by chemical evidences, SERS experiments were carried out on the each sample before to analyze them in interaction. Afterwards, the spectral features were correlated with the topographic data obtained from HS-AFM analyses.

This chapter of the thesis points out the importance and utility of supporting topographic information with chemical data, thereby exceed the limitation of AFM, the lack of sample identification, by correlating it with Raman analysis.

4

Coupling of Atomic Force Microscopy with Raman Spectroscopy

High–speed atomic force microscopy (HS-AFM) and surface enhanced Raman spectroscopy (SERS) were implemented to address three distinct studies previously. In the first part, we have evaluated the performance of our nanoparticle substrates on the detection of a complex human related protein. Next, we have investigated the chemical and topographic features of a small heat shock protein Lo 18 in function of its conformations. Our final study was consist of the murine norovirus binding on detergent resistant membrane domains of mouse leukaemic monocyte cells.

After spontaneous use of SERS and HS-AFM microscopes for biomolecule analyses, we focus on the coupling of these techniques in this chapter. Firstly, we have studied molybdenum disulfide (MoS_2) by a commercial Raman – AFM microscope. In the second part of chapter, we present in detail our setup which combines Toshio Ando's HS-AFM and SERS technique.

4.1 Tip–Enhanced Raman Spectroscopy

Tip–enhanced Raman spectroscopy (TERS) is relatively a new field that belongs to Raman spectroscopy related characterization techniques. TERS combines atomic force microscopy and Raman spectroscopy offers both topographical and chemical features of samples. TERS employs a sharp metal tip where the excitation light is focused on it, through an aperture with a smaller diameter than the excitation wavelength. The metal sharp tip results a signal enhancement likewise in surface enhanced Raman spectroscopy. The spatial resolution of TERS is well below the diffraction limit and it is a nondestructive technique as AFM.

The concept of TERS appears the first time with Wessel's work, when he has used a submicrometer-sized metal particle in scanning tunneling microscopy [178]. Nine years later, Todd and Morris have introduced a version of TERS which is very similar to today's one by using microelectrode with a tip diameter of 1–3 μm [179]. TERS officially becomes more common technique in the early 2000s. The impact of metal tip on the signal exaltation is investigated with analysis of brilliant cresyl blue using a silver coated AFM probe [180]. Micic et al. have simulated the field distribution on the probe using finite element method [181]. Additionally, the single molecule analysis has carried out on TERS and the spectral fluctuations were investigated. Herewith, TERS became a versatile tool for analysis of biological and biomedical samples [182].

4.1.1 TERS study

In collaboration with NanoScience Technology Center, University of Colorado, under the direction of Dr. L. Tetard, we have investigated molybdenum disulfide by our TERS probes. In this work, our aim is to investigate the spectral and topographic features of molybdenum disulfide (MOS_2) and the impact of the metal tip on the Raman signal intensity.

The experiments were carried out on a commercial Raman – AFM microscope, WITeC alpha 300 AR. This microscope offers a scan range of 200 μm × 200 μm × 20 μm including mapping of elastic properties of the sample surface. The Raman excitation light at 532 nm is brought into the microscope via an optical fiber. The incident and scattered beam pass through the same aperture. This aperture is also used for visualizing the sample surface. After collection, the scattered light is directed toward the spectrograph and CCD for spectral analyses. The image and beam path of microscope are given in Fig.4.1.

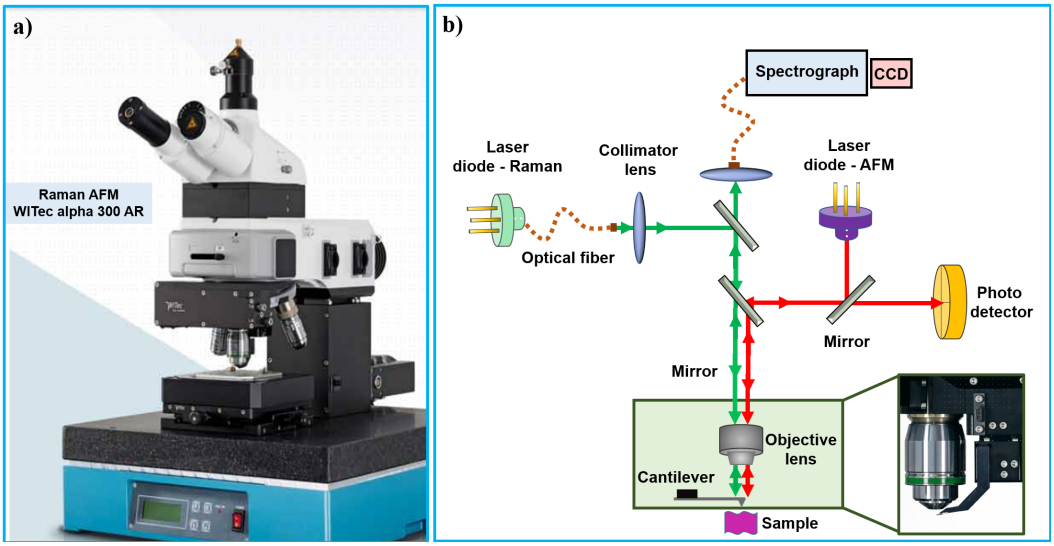

Fig. 4.1: Raman AFM microscopy setup. (a) Cutaway view and (b) schematic representation of microscope.

We have used a top-illumination scheme for tip–enhanced Raman spectroscopy (TERS). A gap-mode configuration with illumination and detection in a straightforward fashion perpendicular to the sample surface has been used. The illumination focuses the light tightly around the tip end, which diminishes contributions of far-field background during TERS measurements. The setup maintains the entire functionality of both scanning probe microscopy and optical microscopy.

TERS images are obtained by using an integrated system which consist of an upright microscope with an 30× long working distance objective (Zeiss EC Epiplan NeoFluar - N.A.= 0.4, W.D.= 3.1 mm) and an integrated AFM head (WITEC).

A Raman spectrometer using a grating of 600 lines centered at 500 nm for lower resolution. To achieve higher resolution, a grating of 1800 lines centered at 500 nm but it provides narrower spectral range. A Nd:YAG laser (λ=532 nm) and a CCD camera (1024 $\times$ 400 pixels, Andor detector) was connected to the microscope/AFM system. A schematic drawing of the TERS setup is shown in Fig.4.2. The location of the laser spot can be precisely controlled by a mirror with a piezomotor such as the laser spot can be aligned to the AFM tip. The sample is placed on an XYZ piezo stage (200 $\times$ 200 $\times$ 20 μm).

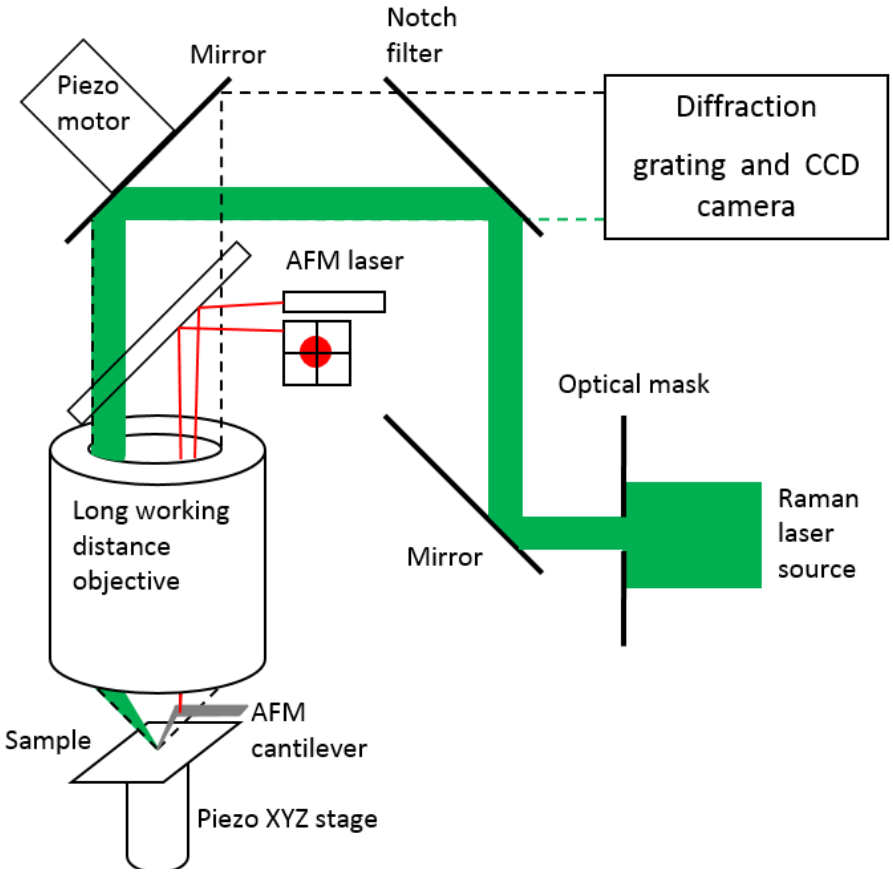

Fig. 4.2: A schematic diagram showing the arrangement of the TERS system in an upright configuration. The scattered light is shown with the dotted line boundaries.

An optical mask was inserted to minimize the backscattered laser light from the back of the cantilever. We employ a technique that creates a side-illumination with the unmodified upright objective allowing the experiment to be carried out with linear polarized laser light.

It was achieved by masking 20% of the laser beam that enters to the objective which eventually only illuminates the sample from the opposite side of the cantilever.

The angle of incidence of the laser beam was just below 23° based on the fact that the N.A. of the objective was 0.4. While the angle of incidence of the laser light has to be aligned with the axis of the tip exactly, we have checked diffraction pattern of NPs at the tip end on video camera to match with the current setup.

Since the AFM tip and the laser beam approach the sample from the same side and the cantilever employed was not transparent, the back of the cantilever will be shadowing that part of the objective. The introduced mask, in this case, also has the advantage of reducing the scattered light from the top surface of the cantilever. While the 20% of the laser beam is masked, the scattered light collected by the same objective is only shadowed by the cantilever which is blocking less than a half of the objective.

The tip protrudes out from the end of cantilever, in such geometry the shadowing effect of the cantilever on the excitation laser spot is minimized. The tip contacts the sample at an angle of ∼20° from the normal to the surface of sample. To maximize the tip enhancement effect, the polarization of the laser light should be parallel to the tip axis. In upright configuration, this can be achieved by using a radially polarized light [183, 184].

The microscope involves an automatic system that allows to focus the laser spot on the sample and the apex of gold nanoparticle coated AFM tips. It was achieved by scanning the surface with the laser beam, moving the mirror, across the approaching tip. Whenever the laser spot entered at the tip area, the appearance of small increase at fluorescent background was noticed (see Fig.4.3). The area with the strongest background signal was regarded as the “hot spot”. The sample was scanned by moving the XYZ piezo stage. The topography image and the tip–enhanced Raman image were collected simultaneously. One second integration time was used to collect the Raman signal at each point of the image.

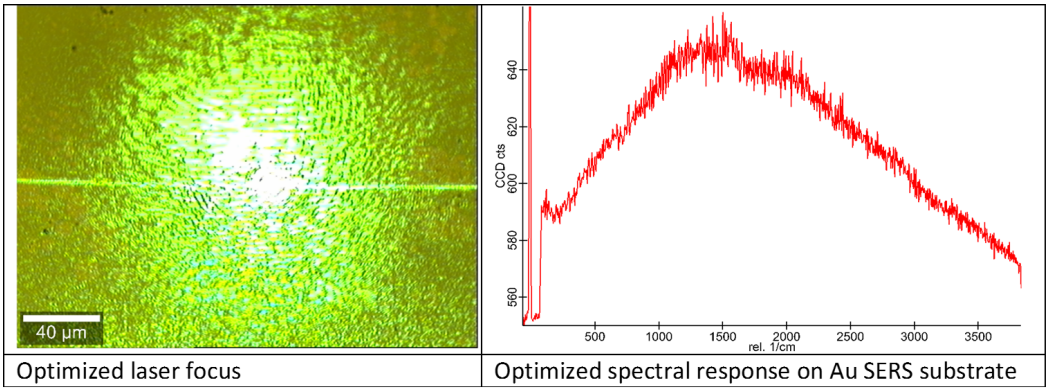

Fig. 4.3: Optimization of TERS configuration using spectrum and diffraction pattern.

A typical Raman spectrum of silicon was obtained from the sample substrate. Likewise, a spectrum of gold nanoparticle can be achieved by focusing on the cantilever. When the laser spot focus correctly at the probe apex, the spectra presents both spectral features of substrate and the gold nanoparticle.

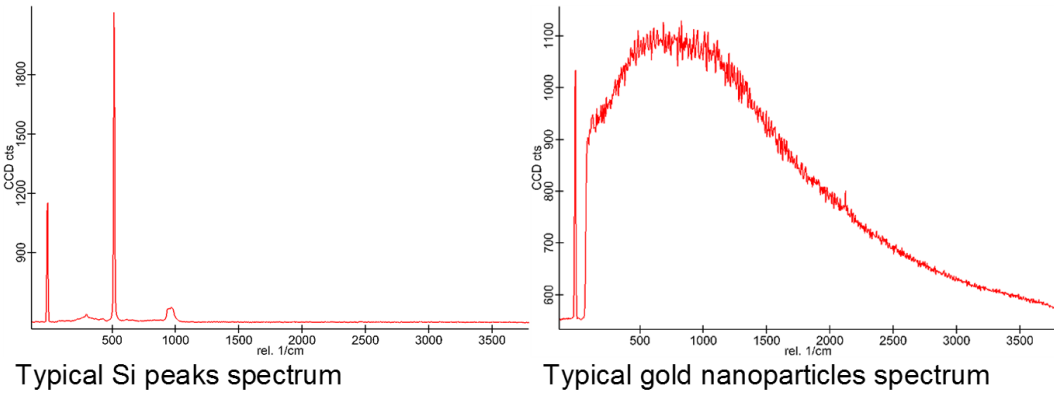

Fig. 4.4: Typical spectrum obtained on silicon substrate and Au nanoparticle TERS cantilever.

When the microscope is operated in contact or even in oscillating contact mode, the tip reaches to close proximity of the sample. A false enhancement of Raman signal could be resulted from the small amount of material transferred to the tip during the approach. Therefore, it is important to verify if the apparent enhancement is sensitive to the location of the tip onto the sample.

This is automatically achieved during the scanning. When an image is obtained by scanning the tip across the sample, only a TERS active tip provides a distribution map with a spatial resolution which is better than what can achieved with a conventional confocal microscope.

We have used high-resolution TERS imaging (100 × 100 up to 256 × 256 pixels) with full spectral information at each pixel, which is necessary for the chemical identification of sample constituents. The main limitation of this technique was the duration time of the imaging. For achieving an image with 100 × 100 pixels resolution requires 25 minutes while it takes more than 90 minutes for an image with 256 × 256 pixels resolution.

With the commercial setup presented in this work, TERS effect was only observed when the system was operated in the contact mode.

4.1.2 Fabrication of TERS probes

TERS probes has a crucial role on Raman signal exaltation and the silver coated AFM tips are the most popular one. However, we have used triangular pyramid-shaped silicon AFM probes (ACCESS-C, APPNANO with the following specifications: h_{tip} = 14–16 μm, radius of curvature of tip = 6 nm, cantilever length = 450 μm, width = 49.5 μm, thickness = 2.5 μm, f=16 kHz and k=0.3 N/m).

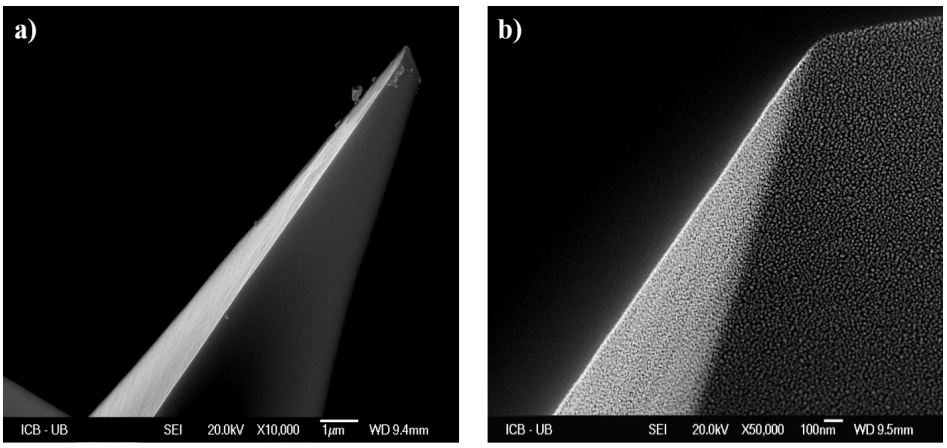

Fig. 4.5: SEM images of the nanoparticle deposited TERS tip. (a) Magnitude: × 10.000, scale: 1 μm and (b) Magnitude: × 50.000, scale: 100 nm.

The GDC protocol (detailed in subsection 2.1.2.1) was applied on AFM probes to cover the tip ofcantilever with crystalline gold nanoparticles. The presence of metallic particles, thereby localized surface plasmons, enhances Raman signal. The diameter of nanoparticles is around 20 nm and they are separated from each other with 1–3 nm of distance. SEM images of these TERS probes are presented in Fig.4.5.

4.1.3 Effect of laser power on AFM imaging

The soft piezo approach technique was adapted to avoid damage of the gold nanoparticle on the extremity of tip. We have used the lowest contact pressure settings to minimize the impact between the tip and sample. We have adapted the laser Raman power in order to detect any effect on AFM imaging (Fig.4.6). We have observed any melting of gold nanoparticles on the surface of substrate neither on TERS probe even after 4 hours of exposition at a power of 1 mW.

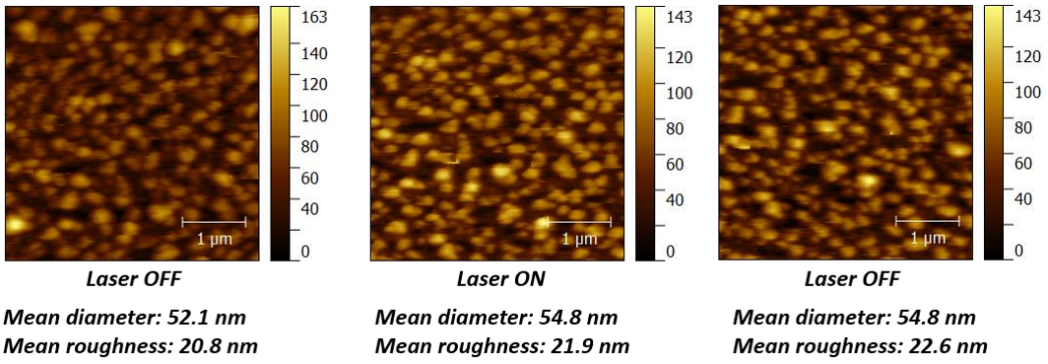

Fig. 4.6: Interaction of Raman laser excitation on gold SERS nanoparticles substrate.

4.1.4 Analysis of molybdenum disulfide by TERS

Molybdenum disulfide (MoS_2) is a semiconducting metal that has various applications in optoelectronics field such as fabrication of field-effect transistors (FETs), photovoltaics and photocatalyst. The Raman signature of MoS_2 is well-known. Prevous studies show that there are four characteristic Raman bands at 32 cm^{-1}, 286 cm^{-1}, 383 cm^{-1} and 408 cm^{-1} [185].

We have compared far–field Raman imaging on Raman-AFM Witec setup with near–field Raman imaging using our TERS probes on a reference sample: MoS_2. We present only the reproducible results obtained on MoS_2 flasks deposited on a silicon substrate.

Figure 4.7 presents Raman spectra of the semiconductor material (a) with its topography (b) and Raman intensity maps. The Raman spectra are achieved with 1 s, 0.5 s and 0.2 s of integration times. All Raman spectra, regardless TERS mode, present Raman bands at 376 cm^{-1}, 407 cm^{-1} and 517 cm^{-1}. The peaks at 376 cm^{-1} and 407 cm^{-1} are associated to two first-order Raman active modes (E^1_{2g} and A_{1g}) of MoS_2 [185]. The E^1_{2g} ($\sim$ 376 cm^{-1}) is the in-plane mode originated from the opposite vibrations of two S atoms against to Mo atom. The A_{1g} ($\sim$ 407 cm^{-1}) is a the out-of-plane vibrations of S atoms in opposite direction to E^1_{2g} one [186]. These two modes depend on the film thickness and their intensity, width and frequency can be influenced [187]. Additionally, Li et al. have reported that the frequency of the E^1_{2g} and A_{1g} modes can be varied monotonously with the layer number of film [185]. The third peak at the spectra corresponds to silicon substrate [188] where the MoS_2 is flask deposited. The highest Raman signal intensity and a higher image resolution are observed for the data obtained with 1s integration time.

The corresponding Raman intensity maps were obtained from the same surface area and given in Fig.4.7.(c), (d) and (e), respectively. By selecting three filters for each peak: Filter 1 (MoS_2): Position = 371.8 cm^{-1} – Width = 37.8 cm^{-1}; Filter 2 (MoS_2): Position = 414.5 cm^{-1} – Width = 45.8 cm^{-1}; Filter 3 (Si): Position = 517.0 cm^{-1} – Width = 61.4 cm^{-1}, we could detect chemically Si and MoS_2, and obtain image of MoS_2 flake and Si substrate. We have noticed a light amplification of Raman intensities using the gold nanoparticles coated probe.
The main result is an increase of the lateral resolution at TERS configuration compared with spontaneous Raman imaging. Raman maps and full spectral information have been obtained. It was shown that only the Raman frequencies of E^1_{2g} (383 cm^{-1}) and A_{1g} (408 cm^{-1}) peaks vary monotonously with the layer number of ultrathin MoS_2 flakes, while intensities or widths of the peaks vary arbitrarily.

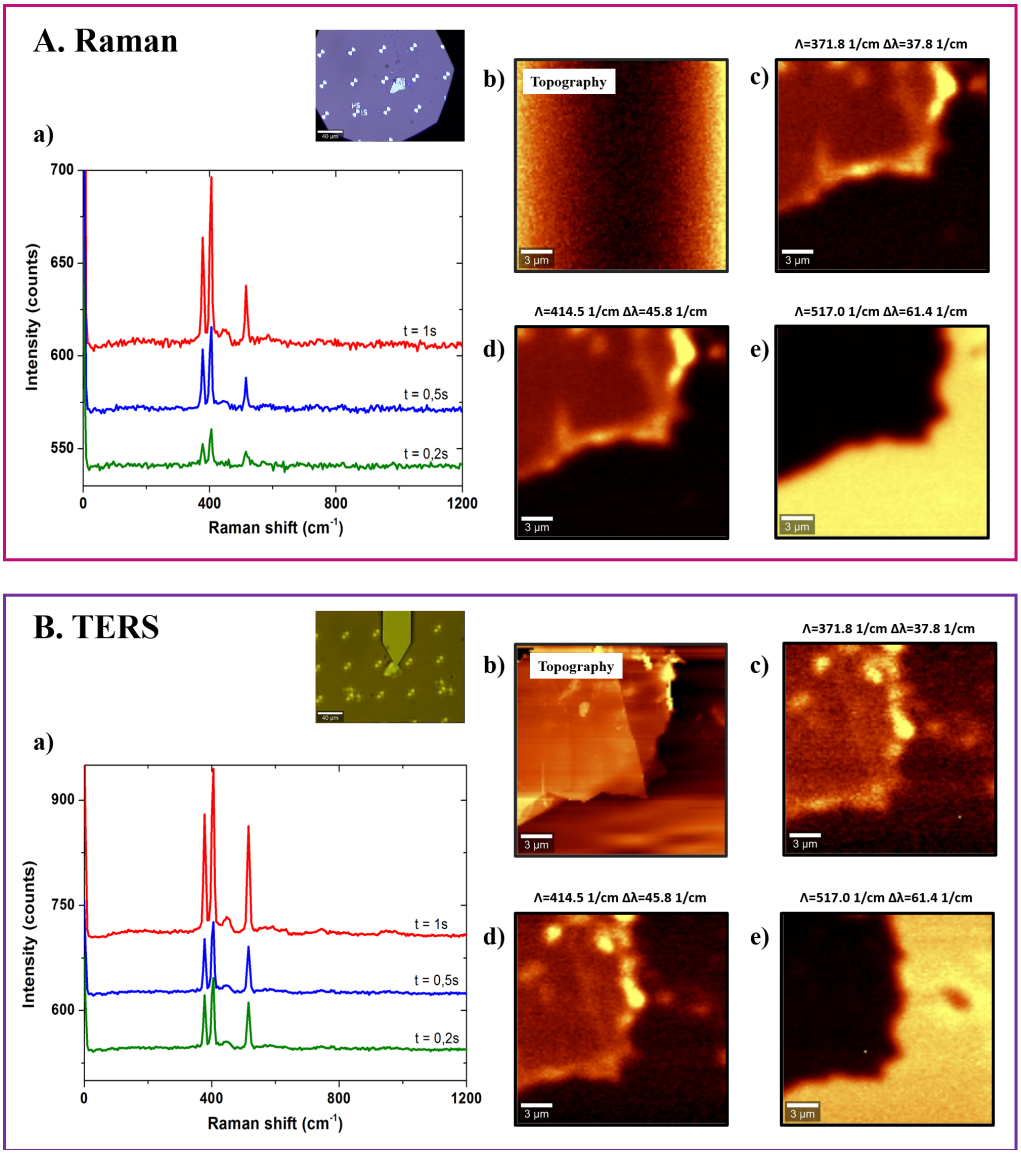

Fig. 4.7: Comparison between spontaneous Raman and TERS imaging. (a) Raman spectra of MoS_2 with 0.2 s, 0.5 s and 1 s acquisition times. Inset: Optical image of the probe–sample configuration. (b) Topography of the sample surface. Raman intensity maps obtained with different filters. For detection of MoS_2 (c) mode E^1_{2g} (376 cm^{-1}), (d) mode A_{1g} (407 cm^{-1}) and (e) detection of Si (517 cm^{-1}).

The same procedure has been performed on rhodamine 6G ($C_{28}H_{31}N_2O_3Cl$) deposited on our gold nanoparticles substrate (GDC). Photobleaching has limited our observations. The results are not presented.

On commercial Raman – AFM microscope, we have used the contact mode. In this case, the sample is always in contact with the gold nanoparticle coated TERS tip and it is exposed to the intense enhancement zone of the tip apex. Concerning HS-AFM/SERS configuration, to achieve the maximum enhancement in oscillating contact mode, a setting that would give a small oscillation at an amplitude of 3-5 nm was adapted. Previous studies [189] have shown that the tip enhancement effect diminishes within 5–15 nm between the sample and tip. It was not possible to obtain any TERS signal from the gold nanoparticles coated TERS tips when operating in oscillating contact mode even when the amplitude of the oscillation was reduced to ∼2 nm. Schultz et al. [190] suggested that when TERS experiment is carried out with linear or azimuthally polarized laser beams, the enhancement zone at the tip is along the X and Y directions rather than at the Z axis along the tip. Furthermore, the polarization of the laser light was not aligned exactly to the tip axis, hence, the enhancement effect is diminished even when the tip is just a few nanometers away from the surface.

4.2 Coupling of HS-AFM with SERS

Conventional atomic force microscopy (AFM) is limited by scanning rate and the absence of sample identification. For attaining to the fast imaging generally a decrease of image resolution is necessary (1 s/frame for 128 × 128 pixels typically), which complicates to observe detailed topography of elaborated samples. Investigating multiple samples on a surface, herewith their interactions between each other, is very interesting topic for biomedical and biological investigations. However, in such case AFM results rely on the outcome of all samples on the surface and attribution of the information to a simple entity remains as an assumption. Confocal microcopy is the most used tool to characterize the supramolecular organization of complex biological samples. Fluorescent dyes are employed as marker to tag a specific component of the sample. Information about the organization of sample can be obtained but the labeling procedure may restrict the mobility of biomolecules and may affect their organization. On the other hand, a force spectroscopy has been developed for the recognition of biomolecules. This technique needs the functionalization of AFM tip with a specific antibody to obtain a particular recognition. However, this method requires knowledge of the sample components and furthermore it is time consuming. AFM has an important limitation that is not being able to characterize the chemical nature of the sample under study.

The final objective was the coupling of surface enhanced Raman spectroscopy (SERS) with HS-AFM. We were expecting the ability to measure molecular binding events in real time, without labeling. We have shown in the previous chapter that the great advantage of SERS is being able to obtain the spectral fingerprints of each molecule or individual molecular structures under the laser spot area with high sensibility. The benefit of combining the high resolution imaging with SERS is achieving the topographic information with subnanometer resolution and the chemical characterization with a sensibility lower than 10^{-12} mole per 300 nm^2 area of sample surface. The challenge was to use Ando's HS-AFM setup for chemical analysis with restrictions concerning the optical pathway and microscope objective.

4.2.1 Properties of SERS coupled HS-AFM setup

SERS coupled HS-AFM setup was designed to procure the physical properties and the chemical composition of the samples under investigation. Our aim was to produce a multifunctional and flexible instrument that offers SERS, TERS, fluorescence and HS-AFM analysis. In order to achieve this goal, several optical elements are incorporated into Toshio's HS-AFM setup (detailed in subsection 1.1.4). All optical detection system of HS-AFM and the electronics were kept as original. In our design, we used Ultra-Wide type high-speed scanner (35 μm $\times$ 35 μm $\times$ 3 μm) to enable the cell analyses. However, the other high speed scanners are adaptable to the microscope (see subsection 1.1.5).

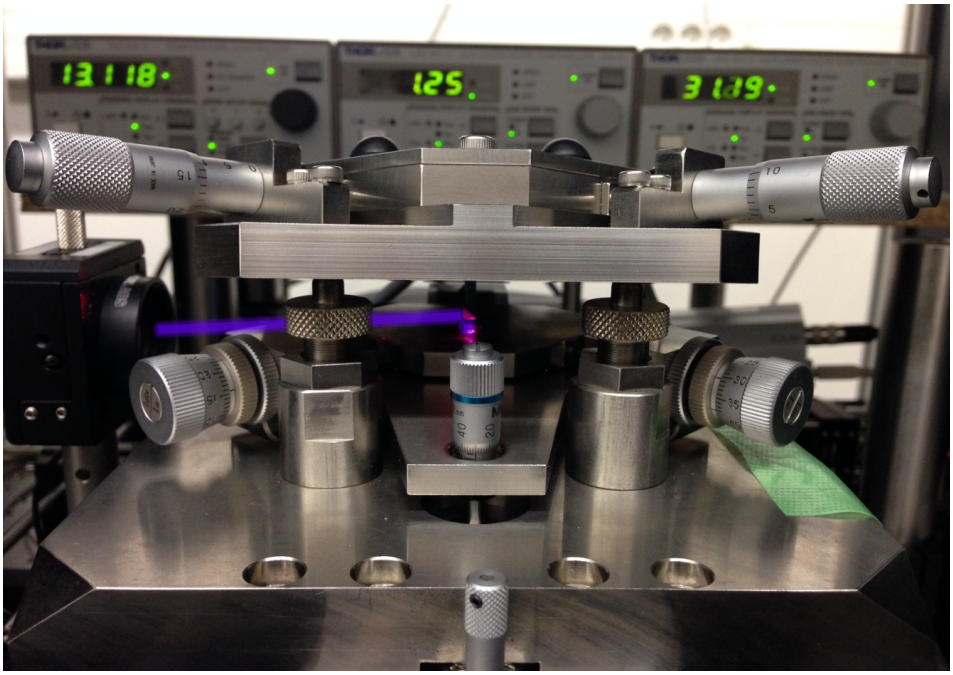

Fig. 4.8: A prism is mounted on HS-AFM microscope head to direct the excitation laser towerd the sample.

HS-AFM & SERS setup provides fluorescence, Raman, Rayleigh and AFM analysis. For imaging, we have used a laser beam at $\lambda = 670$ nm which is focused on the cantilever via a collimator and an objective lens. The reflected light from the cantilever is collected back by the objective lens (Nikon, CFI S Plan Fluor ELWD 40 $\times$, W.D. 8 mm, N.A. 0.45).

The Raman or Fluorescence excitation laser light is also focused through the same objective. We integrated a prism (Edmund, 2 mm size) on the high speed scanner to direct the Raman/Fluorescence excitation light toward the sample. A photography of HS-AFM head with the prism is given in Fig.4.8.

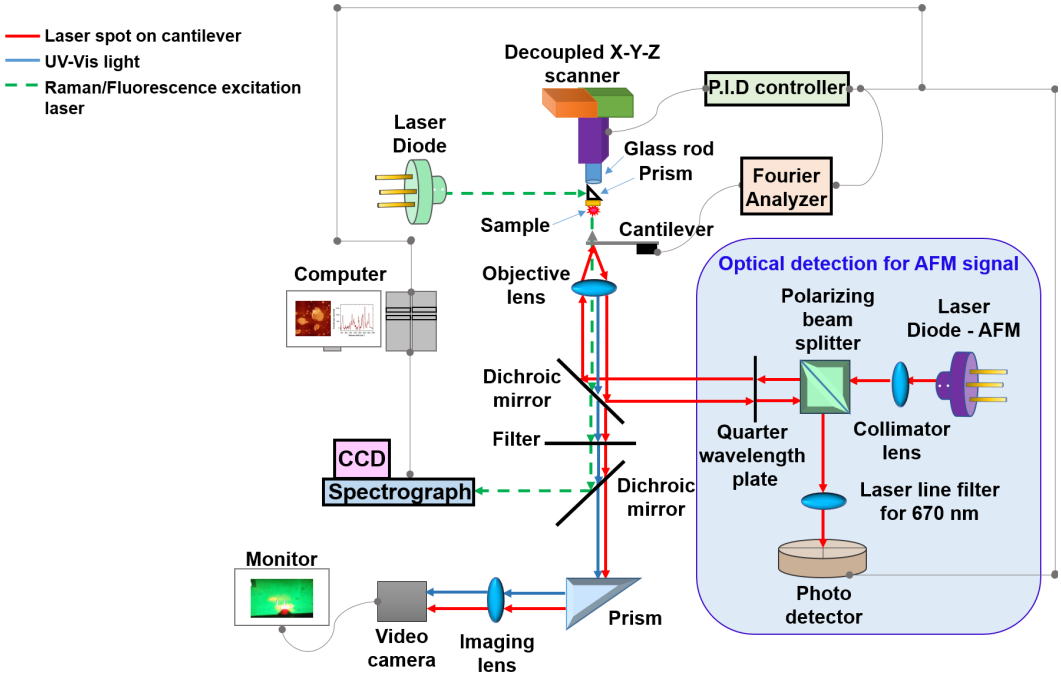

Fig. 4.9: Schematic drawing of SERS combined HS-AFM setup.

The schematic presentation of home-built HS-AFM & SERS setup is given Fig.4.9. We integrated a spectrograph (Shamrock 163, Andor Technology) and CCD camera (iDus 401, Andor Technology).

In the TERS configuration, the sample is directly deposited on the prism while SERS experiments are performed with a nanoparticle covered surface which is fixed on the prism. All experiments were carried out with EBD tip deposited probes except TERS analyses where a specical protocol applied on the EBD tip deposited probes to cover the apex of the tip with the nanoparticles.

For SERS configuration, the sample solution is directly deposited on the gold nanoparticle substrate which is fixed on the prism. The scattered light from sample is collected by an objective.

The scattered Raman light is filtered (Semrock) prior to guide the light toward spectrograph (Shamrock 163, Andor Technology) and CCD camera (iDus 401, Andor Technology). Both Raman and Rayleigh scatterings are blocked at the entrance of video camera for easiness of the calibration of the laser spot on the cantilever. Non-metallic tips are used since metallic tips cause TERS effect.

Figure 4.10 presents the optical path of Raman/fluorescence excitation light and the scattered light.

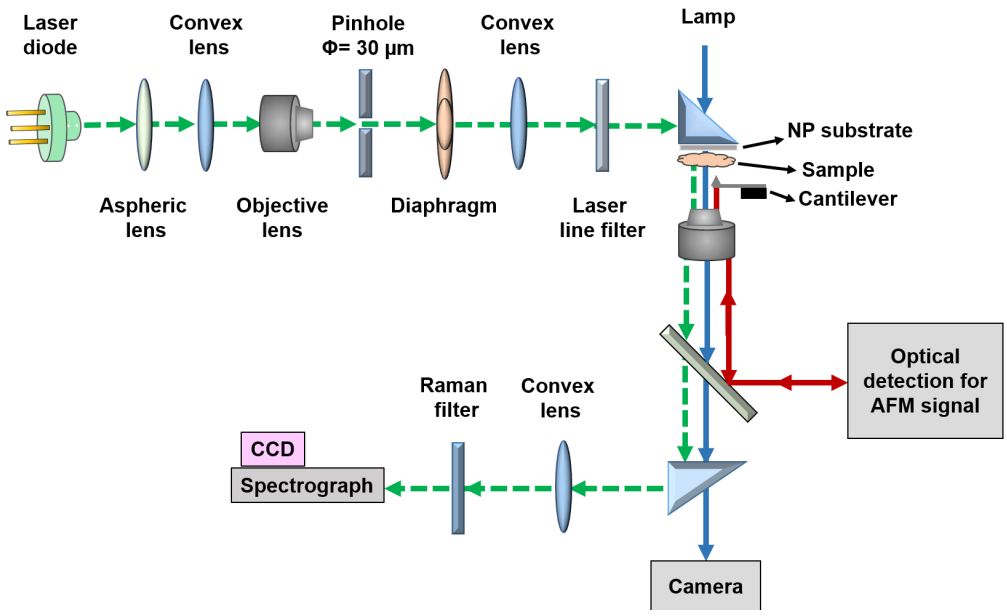

Fig. 4.10: Schematic drawing of SERS combined HS-AFM setup.

4.3 Limits and prospects

We have analyzed methylene blue and protein Lo 18 on our combined microscope setup. Comparing with the results presented in the previous chapter, we could not obtain the same SERS efficiency. No proofs were given for the dynamic analysis of biomolecules. Different configurations were tested to avoid the noise and interference intrinsic to SERS analysis.

We were able to obtain SERS spectra of the samples, however only a few dominant peaks could be assigned to the vibrational modes of the protein or methylene blue.

The focus plane of the sample and the reflected laser spot were separated from few micron (3–5 μm) by using EBD tip deposited HS-AFM probes. In our configuration, the focused Raman laser spot has diameter of $\sim$ 10 μm. We have observed an impact of the size and intensity of the Raman laser spot on the results.

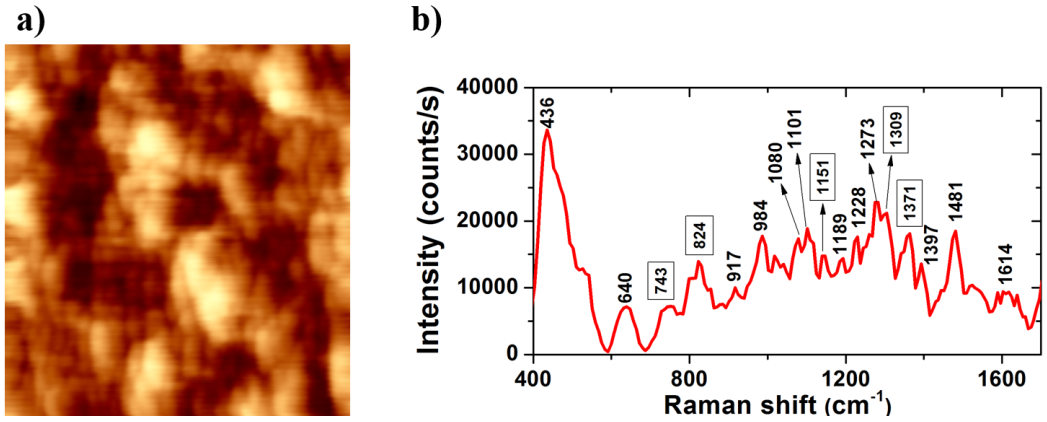

Fig. 4.11: (a) HS-AFM image and (b) SERS spectrum of methylene blue (10^{-6} M) on the nanoparticle substrate obtained from the HS-AFM/SERS configuration. Acquisition time is 10 s for both analysis.

A typical SERS spectra of metlylene blue at 10^{-6} M concentration is given in Fig.2.11. The experiments were carried out by using GDC gold nanoparticle substrates. We have observed five peaks matches with the previous results (see Tab.2.6) while the other peaks are shifted less than 10 cm^{-1} compared with our conventional SERS results. The matched peaks are presented by frames on the spectrum.

We have observed limitations due to the gold nanoparticle substrates. The coverage of gold nanoparticles on the 2 $\times$ 2 mm square glass coverslip was not homogeneous on the borders. We had imaging artefacts due to hydrodynamic interactions at the center of sample. Therefore, it was necessary to combine the presence of molecules and the homogeneous coverage of gold nanoparticles at the border of substrate to attain effective analysis. However, the distribution of molecules on the substrate was irregular and this leads to loss of the reproducibility for the yielded spectra across different mapping points.

For spectral reproducibility measurements, we have analyzed porphyrins. The sample was directly deposited on the gold surface and left to dry to ensure an adsorption. We have used 532 nm and 785 nm excitation wavelengths and adapted accordingly the filters and gratings. The 532 nm provided the best SERS signal. We have compared the spectral reproducibility and SERS effectiveness of different samples.

We have observed the presence of hot spots mostly at the border of substrate (not as seen from previous analysis in chapter 3). The hot spots are sparsely distributed along the border of substrate. Thus, reproducibility of a given spectral map was influenced mainly by the presence of random "hot spots". The number of hot-spots represented 2–5% of SERS-active sites of the substrate for our HS-AFM configuration. Also, the performance of these methods strongly depends on the time of gold substrate storage. This may leads to a reduction in SERS effectiveness due to suffered oxidation damage or distortion of the surface nanostructures. Gold is wrongly considered chemically inactive and stable, more suitable for incorporation inside biosensor platforms. We tried to use the gold substrates immediately just after their fabrications. Even with all these precaution and different settings, we were not able to find the previous results. Some anomalous bands of surface contaminants were also observed. Our SERS spectra had low signal-to-noise ratio.

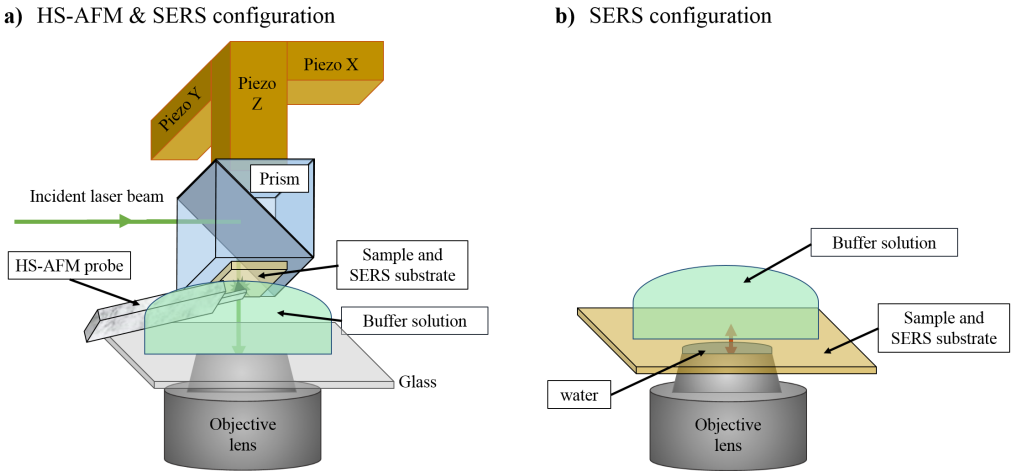

Fig. 4.12: Schematic drawing of the sample position at the HS-AFM/SERS and SERS configurations.

The Raman signal loss at the HS-AFM/SERS configuration is basically resulted from the optical path. The excitation laser light is reflected from the prism and directed to the SERS substrate and sample. The scattered Raman light is dispersed in the liquid medium and pass through the glass of liquid cell. After couple millimeters in air, the scattered light reaches to the objective lens. All these changes of optical mediums, thereby the refractive index, lead a loss at Raman signal. On the other hand, the SERS configuration that we have used for previous experiments involves less "sophisticated" design where the scattered light is directly collected by a water immersion objective.

The interaction area is over few μm^2 at HS-AFM/SERS configuration as seen from Fig.4.13.

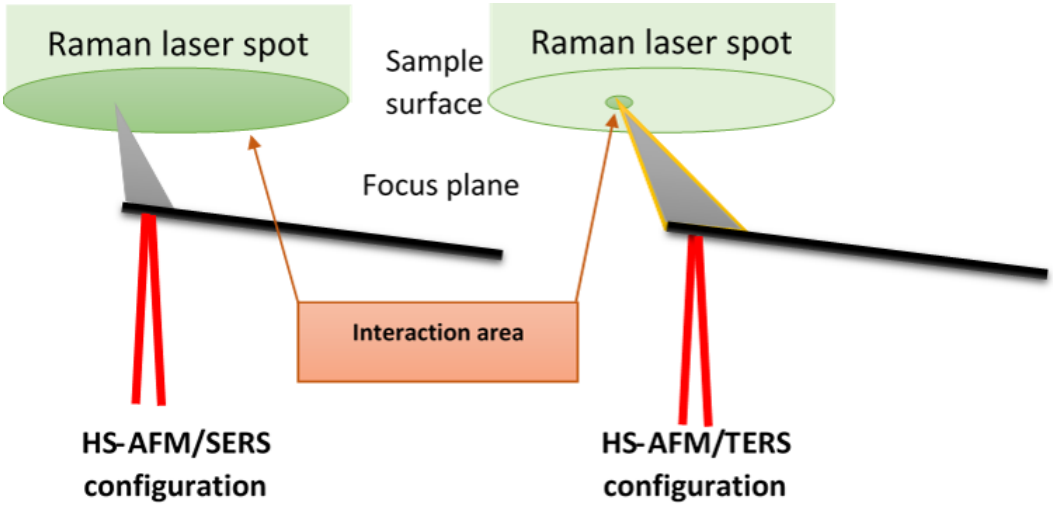

Fig. 4.13: Schematic drawing of Raman laser spot on the HS-AFM/SERS and HS-AFM/TERS configurations.

Whereas at HS-AFM/TERS configuration, we obtain local information but the nanoparticles did not stay long time on the tip apex in oscillating contact mode even using low oscillation amplitude. In air, we obtain reproducible results on a simple specimen MoS_2. For biomolecules, the laser power could not be reduced (in regard of signal noise ratio) sufficiently to avoid perturbation on biomolecules.

General Conclusion and Perspectives

This thesis presents the development of crystalline metal nanoparticles substrates essential for Raman spectroscopy, the coupling of high-speed atomic force microscopy (HS-AFM) with surface-enhanced Raman spectroscopy (SERS). We have shown that different crystalline nanoparticles substrate could be generate such as bi-metallic (Au-Ag). The developed process was extended to the fabrication of tip-enhanced Raman spectroscopy (TERS) probes. The probe are relevant for scanning. In addition to the designing issues, we have discussed the limitations of SERS/dynamic analysis as well as proposing improvements using TERS probe.

We have shown that high-speed AFM remains a very powerful tool that provides to analyze the dynamics of biomolecules in nanometric scale. The observing interactions of biological samples, herewith the change of their topography and dynamics is very interesting and promising topic for applications in the field of biology and medicine. However, to locate a specific entity in the presence of multiple samples furthermore follow its dynamic behavior is absent. The current thesis focuses on investigating multiple samples by HS-AFM microscope and locate each components, moreover procure their chemical features. To achieve this goal, we have aimed to combine HS-AFM microscopy with Raman detections. The whole processes is challenging and requires several intermediate steps and they have been addressed one by one at the chapters of this thesis.

A general problematic of Raman spectroscopy is low signal intensity and it is known that it can be overcame by use of metallic rough substrates. Therefore, our first aim was to develop a fabrication procedure of nanoparticle substrates that allows to attain reproducibility, efficacy and adaptability to different type of metals and substrates. We have evaluated the crystallinity, homogeneity, shape and distribution of nanoparticles on our plasmonic substrates. The performance of substrates on surface enhanced Raman spectroscopy measurements were examined with reference samples by confocal Raman maps and analyses in function of concentration.

After verifying the quality and performance of the nanoparticle substrates, we have addressed three biological problematics by HS-AFM and SERS. We have started from a human derived protein to more complex and large biological structures. We have observed the conformational changes of small heat shock Leuconostoc oenos protein. We have determined the spectral features of specific conformations. Afterwards, we approached to gastroenteritis disease by studying a model system. The chemical and topographic variations due to the virus infection have been determined on the detergent resistant membrane domains of the host cells. We emphasize the importance of scanning a large quantity of pure elements in spite of the challenges. Data bank of spectra is need by the research community. Engineering and experimental practice on all proteins would always favor simplicity, efficiency, and effectiveness in chemical identification. Actually, the Raman spectroscopy suffers of this lack of data.

The three distinct studies indicated us to compatibility of both characterization techniques. However, the separate analyses enable to correlate only general outcome of each technique, the attribution of data to a specific entity is still absent. Moreover, SERS results are based on the collective response of the molecules under the laser spot area: 300 nm diameter spot size under optical configuration, 4–5 μm diameter spot size under HS-AFM configuration. Therefore, we have focused on tip–enhanced Raman spectra and combined microscope at the last chapter of this thesis. Firstly, we have adapted our nanoparticle fabrication procedure to procure TERS tips. The efficacy of our TERS tips was evaluated by

analyzing a well-known sample by a commercial Raman–AFM microscope. Lastly, we have integrated an optical setup to Ando's HS-AFM microscope to adapt fluorescence, TERS and SERS measurements. The functionality of the setup has been tested by individual analysis of each techniques. The cooperation of techniques to attain the spontaneous HS-AFM and Raman analyses is remains as continuation of this work. On the other hand, currently identified challenges, weaknesses, as well as limitations are not yet sufficient in drawing conclusion on the usefulness of Raman spectroscopy AFM imaging coupling. The field is still young and involves various disciplines such as signal processing (adaptation of scanning rate and spectrometer acquisition time), chemical engineering (functionalization of metallic nanoparticles), biological analytical analysis (produce a complete Raman spectra data bank). Paradigms on TERS and underlying theories are either just being set. Therefore, objective and multi-disciplinary approaches would continue to be necessities for studying various biological specimens.

As for the future research, it would be fruitful to undertake a general investigation of the main components of biological membranes by combining mass-spectrometry, infra-red spectroscopy, enhanced Raman spectroscopy, and how to make use of this combination to complement the weaknesses or limitations of each one individually. This study would lead to a basis for designing a combined platform for infra-red and Raman spectroscopies, fluorescence and atomic force microscopies. Along with this pursuit, research need to be performed towards the integration of high-speed atomic force microscope module integrated a stand-alone version for current optical microscopy platforms.

List of Figures

List of Tables

Bibliography

[1] G. Binnig, H. Rohrer, Ch. Gerber, and E. Weibel. Surface Studies by Scanning Tunneling Microscopy. *Phys. Rev. Lett.*, 49:57–61, 1982.

[2] G. Binnig, C. F. Quate, and Ch. Gerber. Atomic Force Microscope. *Phys. Rev. Lett.*, 56:930–3, 1986.

[3] O. Marti, B. Drake, and P. K. Hasma. Atomic force microscopy of liquid-covered surfaces: atomic resolution images. *Appl. Phys. Lett.*, 51:484–6, 1987.

[4] S. Gould, O. Marti, B. Drake, L. Hellemans, C. E. Bracker, P. K. Hansma, N. L. Keder, M. M. Eddy, and G. D. Stucky. Molecular resolution images of amino acid crystals with the atomic force microscope. *Nature*, 332:332–4, 1988.

[5] O. Marti, V. Elings, M. Haugan, C. E. Bracker, J. Schneir, B. Drake, S. A. Gould, J. Gurley, L. Hellemans, K. Shaw, A. L. Weisenhorn, J. Zasadzinski, and P. K. Hansma. Scanning probe microscopy of biological samples and other surfaces. *J. Microsc.*, 152:803–9, 1988.

[6] G. Friedbacher, P. K. Hansma, E. Ramli, and G. D. Stucky. Imaging powders with the atomic force microscope: from biominerals to commercial materials. *Science*, 253:1261–3, 1991.

[7] Q. Zhong, D. Inniss, K. Kjoller, and V.B. Elings. Fractured polymer/silica fiber surface studied by tapping mode atomic force microscopy. *Surf. Sci. Lett.*, 290:L688–92, 1993.

[8] M. Bezanilla, B. Drake, E. Nudler, M. Kashle, P. K. Hansma, and H. G. Hansma. Motion and enzymatic degradation of DNA in the atomic force microscope. *Biophys J.*, 67:2454–9, 1994.

[9] C. Moller, M. Allen, V. Elings, A. Engel, and D. J. Mueller. Tapping-mode Atomic Force Microscopy produces faithful high-resolution images of protein surfaces. *Biophys. J.*, 77:1150–8, 1999.

[10] B. Derjaguin and L. Landau. Theory of the stability of strongly charged lyophobic sols and of the adhesion of strongly charged particles in solutions of electrolytes. *Acta Physico Chemica URSS*, 14:633–, 1941.

[11] E.J.W. Verwey and J.Th.G. Overbeek. Theory of the stability of lyophobic colloids : the interaction of sol particles having an electric double layer. *Elsevier*, page 205, 1948.

[12] W. B. Russel, D. A. Saville, and W. R. Schowalter. Colloidal Dispersions. *New York: Cambridge University Press*, 1989.

[13] B. Drake, C.B. Prater, A.L. Weisenhorn, S.A. Gould, T.R. Albrecht, C.F. Quate, D.S. Cannell, H.G. Hansma, and P.K. Hansma. Imaging crystals, polymers, and processes in water with the atmicroscope microscope. *Science*, 243:1586–9, 1989.

[14] W. Haberle, J.K.H. Hober, F. Ohnesorge, D.P.E. Smith, and G. Binnig. In situ investigations of single living cells infected by viruses. *Ultramicroscopy*, 42-44 Part B:1161–7, 1992.

[15] F. Ohnesorge, W.M. Heckl, W. Haberle, D. Pum, M. Sara, H. Schindler, K. Schilcher, A. Kiener, D.P.E. Smith, U.B. Sleytr, and G. Binnin. Scanning force microscopy studies of the S-layers from Bacillus coagulans E38-66, Bacillus sphaericus CCM2177 and of an antibody binding process. *Ultramicroscopy*, 42-44 Part B:1236–42, 1992.

[16] H.-J. Butt, P. Siedle, K. Seifert, K. Fendler, T. Seeger, E. Bamberg, A.L. Weisenhorn, K. Goldie, and A. Engel. Scan speed limit in Atomic Force Microscopy. *J. Microsc.*, 169:75–84, 1993.

[17] S.C. Minne, S.R. Manalis, and C.F. Quate. Parallel Atomic Force Microscopy using cantilevers with integrated piezoresistive sensors and integrated piezoelectric actuators. *Appl. Phys. Lett.*, 67:3918–20, 1995.

[18] S.R. Manalis, S.C. Minne, and C.F. Quate. Atomic force microscopy for high speed imaging using cantilevers with an integrated actuator and sensor. *Appl. Phys. Lett.*, 68:871–3, 1996.

[19] D.A. Walters, J.P. Cleveland, N.H. Thomson, P.K. Hansma, M.A. Wendman, G. Gurley, and V. Elings. Short cantilevers for Atomic Force Microscopy. *Rev. Sci. Instrum.*, 67:3583–90, 1996.

[20] T. E. Schaffer, J. P. Cleveland, F. Ohnesorge, D. A. Walters, and P. K. Hansma. Studies of vibrating Atomic Force Microscope cantilevers in liquid. *J. Appl. Phys.*, 80:3622–7, 1996.

[21] S. Kasas, N. H. Thomson, B. L. Smith, H. G. Hansma, X. Zhu, M. Guthold, C. Bustamante, E. T. Kool, M. Kashlev, and P. K. Hansma. Escherichia coli RNA polymerase activity observed using atomic force microscopy. *Biochemistry*, 36:461–8, 1997.

[22] M. B. Viani, T. E. Schaffer, G. T. Paloczi, L. I. Pietrasanta, B. L. Smith, J. B. Thompson, M. Richter, M. Rief, H. E. Gaub, K. W. Plaxco, A. N. Cleland, H. G. Hansma, and P. K. Hansma. Fast imaging and fast force spectroscopy of single biopolymers with a new Atomic Force Microscope designed for small cantilevers. *Rev. Sci. Instrum.*, 70:4300–3, 1999.

[23] T. Ando, N. Kodera, E. Takai, D. Maruyama, K. Saito, and A. Toda. A High-Speed Atomic Force Microscope for studying biological macromolecules. *Proc. Natl. Acad. Sci. USA*, 98:12468–72, 2001.

[24] T. Ando, N. Kodera, D. Maruyama, E. Takai, K. Saito, and A. Toda. A High-Speed Atomic Force Microscope for Studying Biological Macromolecules in Action. *Jpn. J. Appl. Phys.*, 41:4851, 2002.

[25] S. Fukuda, T. Uchihashi, R. Iino, Y. Okazaki, M. Yoshida, K. Igarashi, and

Toshio Ando. High-speed Atomic Force Microscope combined with single-molecule fluorescence microscope. *Rev. Sci. Instrum.*, 84:073706, 2013.

[26] N. Kodera, M. Sakashita, and T. Ando. Dynamic proportional-integral-differential controller for high-speed atomic force microscopy. *Rev. Sci. Instrum.*, 77:083704, 2006.

[27] T. Ando, T. Uchihashi, and T. Fukuma. High-speed Atomic Force Microscopy for nano-visualization of dynamic biomolecular processes. *Prog. Surf. Sci.*, 83:337–437, 2008.

[28] J. H. Kindt, G. E. Fantner, J. B. Thompson, and P. K. Hansma. Automated wafer-scale fabrication of electron beam deposited tips for atomic force microscopes using pattern recognition. *Nanotechnology*, 15:1131–4, 2004.

[29] T. Ando, T. Uchihashi, N. Kodera, A. Miyagi, R. Nakakita, H. Yamashita, and K. Matada. High-speed Atomic Force Microscopy for capturing the dynamic behavior of protein molecules at work. *e-J. Surf. Sci. Nanotech.*, 3:384–92, 2005.

[30] H. Yamashita, N. Kodera, A. Miyagi, T. Uchihashi, D. Yamamoto, and T. Ando. Tip-sample distance control using photothermal actuation of a small cantilever for high-speed atomic force microscopy. *Rev. Sci. Instrum.*, 78:083702, 2007.

[31] T. Ando, T. Uchihashi, and N. Kodera. High-Speed AFM and Applications to Biomolecular Systems. *Annu. Rev. Biophys.*, 42:393–414, 2013.

[32] T. Ando and T. Uchihashi. *Nanoscale Liquid Interfaces*, volume Chapter 19 - High Speed AFM and imaging of Biomolecular Processes. Pan Stanford Publishing Pte. Ltd., 2013.

[33] J. H. Hafner, C. L. Cheung, and C. M. Lieber. Direct Growth of Single-Walled Carbon Nanotube Scanning Probe Microscopy Tips. *J. Am. Chem. Soc.*, 121:9750–1, 1999.

[34] F. Zenhausern, M. Adrian, B. Tenheggelerbordier, F. Ardizzoni, and P. Descouts. Enhanced imaging of biomolecules with electron-beam deposited tips for scanning force microscopy. *J. Appl. Phys.*, 73:7232–7, 1993.

[35] J. D. Beard and S. N. Gordeev. Large flexibility of high aspect ratio carbon nanostructures fabricated by electron-beam-induced deposition. *Nanotechnology*, 21:475702, 2010.

[36] C. Chicanne, S. Emonin, N. Richard, T. David, E. Bourillot, J. P. Goudonnet, and Y. Lacroute. Characterization of optogeometric parameters of optical fibers by near-field scanning probe microscopies. *J. Opt. Soc. Am. B*, 47:1473–82, 2000.

[37] W. L. Barnes, A. Dereux, and T. W. Ebbesen. Surface plasmon subwavelength optics. *Nature*, 424:824–30, 2003.

[38] C.V. Raman and K. S. Krishnan. A new type of secondary radiation. *Nature*, 121:501–2, 1928.

[39] M. Fleischmann, P. J. Hendra, and A. J. McQuillan. Raman spectra of pyridine adsorbed at silver electrode. *Chem. Phys. Lett.*, 26:163–6, 1974.

[40] M. G. Albrecht and J. A. Creighton. Anomalously Intense Raman Spectra of Pyridine at a Silver Electrode. *J. Am. Chem. Soc.*, 99:5215–7, 1977.

[41] D. L. Jeanmaire and R. P. Van Duyne. Surface Raman spectroelectrochemistry: Part I. Heterocyclic, aromatic, and aliphatic amines adsorbed on the anodized silver electrode. *J. Electroanal. Chem. Interfacial Electrochem.*, 84:1–20, 1977.

[42] R. L. Aggarwal, L. W. Farrar, E. D. Diebold, and D. L. Polla. Measurement of the absolute Raman scattering cross section of the 1584-cm-1 band of benzenethiol and the surface-enhanced Raman scattering cross section enhancement factor for femtosecond laser-nanostructured substrates. *J. Raman Spectrosc.*, 40:1331–3, 2009.

[43] L. Brus. Noble Metal Nanocrystals: Plasmon Electron Transfer Photochemistry and Single-Molecule Raman Spectroscopy. *Acc. Chem. Res.*, 41:1742–9, 2008.

[44] A. Campion and P. Kambhampati. Surface-enhanced Raman scattering. *Chem. Soc. Rev.*, 27:241–50, 1998.

[45] W. E. Doering and S. Nie. Single-Molecule and Single-Nanoparticle SERS: Examining the Roles of Surface Active Sites and Chemical Enhancement. *J. Phys. Chem. B*, 106:311–7, 2002.

[46] H. Xu, J. Aizpurua, M. Kall, and P. Apell. Electromagnetic contributions to single-molecule sensitivity in surface-enhanced Raman scattering. *Phys. Rev. E*, 62:4318–24, 2000.

[47] T. Liebermann and W. Knoll. Surface-plasmon field-enhanced fluorescence spectroscopy. *Colloids and Surfaces A: Physicochemical and Engineering Aspects*, 171:115–30, 2000.

[48] Y. Hong, Y. M. Huh, D. S. Yoon, and J. Yang. Nanobiosensors based on localized surface plasmon resonance for biomarker detection. *Journal of Nanomaterials*, 2012, 2012.

[49] E. C. Le Ru, J. Grand, I. Sow, W. R. C. Somerville, P. G. Etchegoin, M. Treguer-Delapierre, G. Charron, N. Felidj, G. Levi, and J. Aubard. A scheme for detecting every single target molecule with Surface-Enhanced Raman Spectroscopy. *Nano Lett.*, 11:5013–9, 2011.

[50] C. Fernandez-Lopez, C. Mateo-Mateo, R. A. Alvarez-Puebla, J. Perez-Juste, I. Pastoriza-Santos, and L. M. Liz-Marzan. Highly controlled silica coating of PEG-Capped metal nanoparticles and preparation of SERS-Encoded particles. *Langmuir*, 25:13894–9, 2009.

[51] J. Margueritat, H. Gehan, J. Grand, G. Levi, J. Aubard, N. Felidj, A. Bouhelier, G. Colas-Des-Francs, L. Markey, C. Marco De Lucas, A. Dereux, and E. Finot. Influence of the number of nanoparticles on the enhancement

properties of Surface-Enhanced Raman Scattering active area: sensitivity versus repeatability. *ACS Nano*, 5:1630–8, 2011.

[52] T. Brule, H. Yockell-Lelievre, A. Bouhelier, J. Margueritat, L. Markey, A. Lerayand A. Dereux, and E. Finot. Sorting of Enhanced Reference Raman Spectra of a Single Amino Acid Molecule. *J. Phys. Chem. C*, 118:17975–82, 2014.

[53] A. J. Haes, S. Zou, G. C. Schatz, and R. P. Van Duyne. A nanoscale optical biosensor: the long range distance dependence of the localized surface plasmon resonance of noble metal nanoparticles. *J. Phys. Chem. B*, 108:109–16, 2004.

[54] Y. Songa and H. E. Elsayed-Alib. Aqueous phase Ag nanoparticles with controlled shapes fabricated by a modified nanosphere lithography and their optical properties. *Appl. Surf. Sci.*, 256:5961–7, 2010.

[55] X. Zhang, J. Zhao, A. V. Whitney, J. W. Elam, and R. P. Van Duyne. Ultrastable substrates for Surface-Enhanced Raman Spectroscopy: Al2O3 overlayers fabricated by atomic layer deposition yield improved anthrax biomarker detection. *J. Am. Chem. Soc.*, 128:10304–9, 2006.

[56] G. Barbillon, J.-L. Bijeon, J. Plain, M. Lamy de la Chapelle, P.-M. Adam, and P. Royer. Electron beam lithography designed chemical nanosensors based on localized surface plasmon resonance. *Surf. Sci.*, 601:5057–61, 2007.

[57] L. Billot, M. Lamy de la Chapelle, A.-S. Grimault, A. Vial, D. Barchiesi, J.-L. Bijeon, P.-M. Adam, and P. Royer. Surface enhanced Raman scattering on gold nanowire arrays: Evidence of strong multipolar surface plasmon resonance enhancement. *Chem. Phys. Lett.*, 422:303–7, 2006.

[58] T. D. Corrigan, S.-H. Guo, H. Szmacinski, and R. J. Phaneuf. Systematic study of the size and spacing dependence of Ag nanoparticle enhanced fluorescence using electron-beam lithography. *Appl. Phys. Lett.*, 88:101112, 2006.

[59] A. L. Koh, A. I. Fernandez-Dominguez, D. W. McComb, S. A. Maier, and J. K. W. Yang. High-Resolution mapping of Electron-Beam-Excited plasmon

modes in lithographically defined gold nanostructures. *Nano Lett.*, 11:1323–30, 2011.

[60] C. Huang, A. Bouhelier, G. Colas des Francs, A. Bruyant, A. Guenot, E. Finot, J.-C. Weeber, and A. Dereux. Gain, detuning, and radiation patterns of nanoparticle optical antennas. *Phys. Rev. B*, 78:155407, 2008.

[61] A. M. Kern and O. J. F. Martin. Excitation and reemission of molecules near realistic plasmonic nanostructures. *Nano Lett.*, 11:482–7, 2011.

[62] M. Pelton, J. Aizpurua, and G. Bryant. Metal-nanoparticle plasmonics. *Laser Photonics Rev.*, 2:136–59, 2008.

[63] E. Hutter, S. Cha, J. F. Liu, J. Park, J. Yi, J. H. Fendler, and D. Roy. Role of Substrate Metal in Gold Nanoparticle Enhanced Surface Plasmon Resonance Imaging. *The Journal of Physical Chemistry B*, 105:8–12, 2001.

[64] A. D. McFarland and R. P. Van Duyne. Single Silver Nanoparticles as Real-Time Optical Sensors with Zeptomole Sensitivity. *Nano Lett.*, 3:1057–62, 2003.

[65] C. L. Haynes, C. R. Yonzon, X. Zhang, and R. P. Van Duyne. Surface-enhanced Raman sensors: early history and the development of sensors for quantitative biowarfare agent and glucose detection. *J. Raman Spectrosc.*, 36:471–84, 2005.

[66] A. B. Dahlin, J. O. Tegenfeldt, and F. Hook. Improving the instrumental resolution of sensors based on localized surface plasmon resonance. *Anal. Chem.*, 78:4416–23, 2006.

[67] D. Erickson, S. Mandal, A. H. J. Yang, and B. Cordovez. Nanobiosensors: optofluidic, electrical and mechanical approaches to biomolecular detection at the nanoscale. *Microfluid. Nanofluid.*, 4:33–52, 2008.

[68] I. Ament, J. Prasad, A. Henkel, S. Schmachtel, and C. Sonnichsen. Single Unlabeled Protein Detection on Individual Plasmonic Nanoparticles. *Nano Lett.*, 12:1092–5, 2012.

[69] S. Byahut and T. E. Furtak. Direct comparison of the chemical properties of single crystal Ag(111) and electrochemically roughened Ag as substrates for surface Raman scattering. *Langmuir*, 7:508–13, 1991.

[70] J. P. Goudonnet, J. L. Bijeon, R. J. Warmack, and T. L. Ferrell. Substrate effects on the surface-enhanced Raman spectrum of benzoic acid adsorbed on silver oblate microparticles. *Phys. Rev. B*, 43:4605–12, 1991.

[71] K. Kneipp, H. Kneipp, and J. Kneipp. Surface-Enhanced Raman Scattering in Local Optical Fields of Silver and Gold NanoaggregatesFrom Single-Molecule Raman Spectroscopy to Ultrasensitive Probing in Live Cells. *Acc. Chem. Res.*, 39:443–50, 2006.

[72] J. Zhao, J. A. Dieringer, X. Zhang, G. C. Schatz, and R. P. Van Duyne. Wavelength-Scanned Surface-Enhanced Resonance Raman Excitation Spectroscopy. *The Journal of Physical Chemistry C*, 112:19302–10, 2008.

[73] C. L. Haynes and R. P. Van Duyne. Plasmon-Sampled Surface-Enhanced Raman Excitation Spectroscopy. *The Journal of Physical Chemistry B*, 107:7426–33, 2003.

[74] K. A. Willets and R. P. Van Duyne. Localized surface plasmon resonance spectroscopy and sensing. *Annu. Rev. Phys. Chem.*, 58:267–97, 2007.

[75] P. K. Jain, K. S. Lee, I. H El-Sayed, and M. A. El-Sayed. Calculated Absorption and Scattering Properties of Gold Nanoparticles of Different Size, Shape, and Composition: Applications in Biological Imaging and Biomedicine. *The Journal of Physical Chemistry B*, 110:7238–48, 2006.

[76] K. Akaishi, K. Ezaki, O. Motojima, and M. Nakasuga. Production of ultrahigh vacuum by helium glow discharge cleaning in an unbaked vacuum chamber. *Vacuum*, 48:767–70, 1997.

[77] K. Akaishi, K. Ezaki, Y. Kubota, and O. Motojima. Reduction of water outgassing and UHV production in an unbaked vacuum chamber by neon gas discharge. *Vacuum*, 53:285–9, 1999.

[78] E. N. Aybeke, Y. Lacroute, C. Elie-Caille, A. Bouhelier, E. Bourillot, and E. Lesniewska. Homogeneous large-scale crystalline nanoparticle-covered substrate with high SERS performance. *Nanotechnology*, 26:245302, 2015.

[79] N. Otsu. A Threshold Selection Method from Gray-Level Histograms. *IEEE Trans. Sys., Man., Cyber.*, 9:62–6, 1979.

[80] W. Yang, J. Hulteen, G. C. Schatz, and R. P. Van Duyne. A surface-enhanced hyper-Raman and surface-enhanced Raman scattering study of trans-1,2-bis(4-pyridyl)ethylene adsorbed onto silver film over nanosphere electrodes. Vibrational assignments: Experiment and Theory. *J. Chem. Phys.*, 104:4313–23, 1996.

[81] R. G. Freeman, R. M. Bright, M. B. Hommer, and M. J. Natan. Size selection of colloidal gold aggregates by filtration: effect on surface-enhanced Raman scattering intensities. *J. Raman Spectrosc.*, 30:733–8, 1999.

[82] P. M. Tessier, O. D. Velev, A. T. Kalambur, J. F. Rabolt, A. M. Lenhoff, and E. W. Kaler. Assembly of Gold Nanostructured Films Templated by Colloidal Crystals and Use in Surface-Enhanced Raman Spectroscopy. *J. Am. Chem. Soc*, 122:9554–5, 2000.

[83] S. B. Chaney, S. Shanmukh, R. A. Dluhy, and Y. P. Zhao. Aligned silver nanorod arrays produce high sensitivity surface-enhanced Raman spectroscopy substrates. *Appl. Phys. Lett.*, 87:031908, 2005.

[84] Y. Yang, L. Xiong, J. Shi, and M. Nogami. Aligned silver nanorod arrays for surface-enhanced Raman scattering. *Nanotechnology*, 17:2670, 2006.

[85] N. Felidj, J. Aubard, G. Levi, J. R. Krenn, M. Salerno, G. Schider, B. Lamprecht, A. Leitner, and F. R. Aussenegg. Controlling the optical response of regular arrays of gold particles for surface-enhanced Raman scattering. *Phys. Rev. B*, 65:075419, 2002.

[86] J. Grand, S. Kostcheev, J. L. Bijeon, M. Lamy de la Chapelle, P. M. Adam, A. Rumyantseva, G. Lerondel, and P. Royer. Optimization of SERS-active substrates for near-field Raman spectroscopy. *Synth. Met.*, 139:621–4, 2003.

[87] N. Felidj, A. L. Truong, J. Aubard, G. Levi, J. R. Krenn, A. Hohenau, A. Leitner, and F. R. Aussenegg. Gold particle interaction in regular arrays probed by surface enhanced Raman scattering. *The Journal of Chemical Physics*, 120:7141–6, 2004.

[88] G. Laurent, N. Felidj, J. Grand, J. Aubard, G. Levi, A. Hohenau, F. R. Aussenegg, and J. R. Krenn. Raman scattering images and spectra of gold ring arrays. *Phys. Rev. B*, 73:245417, 2006.

[89] A. Merlen, V. Gadenne, J. Romann, V. Chevallier, L. Patrone, and J. C. Valmalette. Surface enhanced Raman spectroscopy of organic molecules deposited on gold sputtered substrates. *Nanotechnology*, 20:215705, 2009.

[90] Gui-Na Xiao and Shi-Qing Man. Surface-enhanced Raman scattering of methylene blue adsorbed on cap-shaped silver nanoparticles. *Chem. Phys. Lett.*, 447:305–9, 2007.

[91] X. Dong, H. Gu, J. Kang, X. Yuan, and J. Wu. Effects of the surface modification of silver nanoparticles on the surface-enhanced Raman spectroscopy of methylene blue for borohydride-reduced silver colloid. *Journal of Molecular Structure*, 984:396–401, 2010.

[92] N. Nuntawong, M. Horprathum, P. Eiamchai, K. Wong-ek, V. Patthanasettakul, and P. Chindaudom. Surface-enhanced Raman scattering substrate of silver nanoparticles depositing on AAO template fabricated by magnetron sputtering. *Vacuum*, 84:1415–8, 2010.

[93] K. Wong-ek, P. Eiamchai, M. Horprathum, V. Patthanasettakul, P. Limnonthakul, P. Chindaudom, and N. Nuntawong. Silver nanoparticles deposited on anodic aluminum oxide template using magnetron sputtering for surface-enhanced Raman scattering substrate. *Thin Solid Films*, 518:7128–32, 2010.

[94] S. H. A. Nicolai and J. C. Rubim. Surface-Enhanced Resonance Raman (SERR) Spectra of Methylene Blue adsorbed on a silver electrode. *Langmuir*, 19:4291–4, 2003.

[95] N. Zaghbani, A. Hafiane, and M. Dhahbi. Separation of methylene blue from aqueous solution by micellar enhanced ultrafiltration. *Separation and Purification Technology*, 55:117–24, 2007.

[96] K. Jia, J. L. Bijeon, P. M. Adam, and R. E. Ionescu. Large scale fabrication of gold nano-structured substrates via high temperature annealing and their direct use for the LSPR detection of atrazine. *Plasmonics*, 8:143–51, 2012.

[97] B. Sepulveda, P. C. Angelome, L. M. Lechuga, and L. M. Liz-Marzan. LSPR-based nanobiosensors. *Nano Today*, 4:244–51, 2009.

[98] S. Khan, F. Alam, A. Azam, and A. U. Khan. Gold nanoparticles enhance methylene blue-induced photodynamic therapy: a novel therapeutic approach to inhibit Candida albicans biofilm. *Int J Nanomedicine.*, 7:3245–57, 2012.

[99] S. Habuchi, M. Cotlet, R. Gronheid, G. Dirix, J. Michiels, J. Vanderleyden, F. C. De Schryver, and J. Hofkens. Single-Molecule Surface Enhanced Resonance Raman Spectroscopy of the Enhanced Green Fluorescent Protein. *J. Am. Chem. Soc.*, 125:8446–7, 2003.

[100] X. M. Qian and S. M. Nie. Single-molecule and single-nanoparticle SERS: from fundamental mechanisms to biomedical applications. *Chem. Soc. Rev.*, 37:912–20, 2008.

[101] S. M. Stranahan and K. A. Willets. Super-resolution Optical Imaging of Single-Molecule SERS Hot Spots. *Nano Lett.*, 10:3777–84, 2010.

[102] Y. Fang, N. H.Seong, and D. D. Dlott. Measurement of the Distribution of Site Enhancements in Surface-Enhanced Raman Scattering. *Science*, 321:388–92, 2008.

[103] A. Weiss and G. Haran. Time-Dependent Single-Molecule Raman Scattering as a Probe of Surface Dynamics. *J. Phys. Chem. B*, 105:12348–54, 2001.

[104] A. J. Meixner, T. Vosgrone, and M. Sackrow. Nanoscale surface-enhanced resonance Raman scattering spectroscopy of single molecules on isolated silver clusters. *J. Lumin.*, 94-95:147–52, 2001.

[105] J. Margueritat, A. Bouhelier, L. Markey, G. Colas des Francs, A. Dereux, S. Lau-Truong, J. Grand, G. Levi, N. Felidj, J. Aubard, and E. Finot. Discerning the Origins of the Amplitude Fluctuations in Dynamic Raman Nanospectroscopy. *J. Phys. Chem. C*, 116:26919–23, 2012.

[106] K. Kneipp, Y. Wang, R. R. Dasari, and M. S. Feld. Approach to Single-Molecule Detection Using Surface-Enhanced Resonance Raman-Scattering (Serrs) - a Study Using Rhodamine 6g on Colloidal Silver. *Appl. Spectrosc.*, 49:780–4, 1995.

[107] K. Kneipp, H. Kneipp, I. Itzkan, R. R. Dasari, and M. S. Feld. Ultrasensitive Chemical Analysis by Raman Spectroscopy. *Chem. Rev.*, 99:2957–75, 1999.

[108] M. Kakita, V. Kaliaperumal, and H. o. Hamaguchi. Resonance Raman quantification of the redox state of cytochromes b and c in-vivo and in-vitro. *J. Biophotonics*, 5:20–4, 2012.

[109] J. B. Schenkman and I. Jansson. The many roles of cytochrome b5. *Pharmacology & Therapeutics*, 97:139–52, 2003.

[110] W. Boireau. *Caracterisation electrochimique du cytochrome b5 libre ou reconstitue dans des structures lipidiques supportees.* PhD thesis, Universite de technologie de Compiegne, 1999.

[111] W. Boireau, A. C. Duncan, and D. Pompon. Bioengineering and Characterization of DNA-Protein Assemblies Floating on Supported Membranes. In Tuan Vo-Dinh, editor, *Protein Nanotechnology*, volume 300 of *Methods in Molecular Biology*, pages 349–368. Humana Press, 2005.

[112] S. Aoyagi, A.Rouleau, and W. Boireau. TOF-SIMS structural characterization of self-assembly monolayer of cytochrome b5 onto gold substrate. *App. Surf. Sci.*, 255:1071–4, 2008.

[113] C. Elie-Caille, J. Y. Rauch, A. Rouleau, and W. Boireau. Preparation of flat gold terraces for protein chip developments. *Micro & Nano Letters*, 4:88–94, 2009.

[114] F. Adar and M. Erecinska. Resonance Raman spectra of the b- And c-type cytochromes of succinate-cytochrome c reductase. *Archives of Biochemistry and Biophysics*, 165:570–80, 1974.

[115] F. Adar. Resonance Raman spectra of cytochrome b5 and its mesoheme and deuteroheme modifications. *Archives of Biochemistry and Biophysics*, 170:644–50, 1975.

[116] N. M. Sijtsema, C. Otto, G. M. J. Segers-Nolten, A. J. Verhoeven, and J. Greve. Resonance Raman Microspectroscopy of Myeloperoxidase and Cytochrome b558 in Human Neutrophilic Granulocytes. *Biophys. J.*, 74:3250–5, 1998.

[117] M. Ehrnsperger, H. Lilie, M. Gaestel, and J. Buchner. The dynamics of Hsp25 quaternary structure. Structure and function of different oligomeric species. *J. Biol. Chem.*, 274:14867–74, 1999.

[118] K. L. Friedrich, K. C. Giese, N. R. Buan, and E. Vierling. Interactions between Small Heat Shock Protein Subunits and Substrate in Small Heat Shock Protein-Substrate Complexes. *J. Biol. Chem.*, 279:1080–9, 2004.

[119] M.-P. Jobin, F. Delmas, D. Garmyn, C. Divies, and J. Guzzo. Molecular characterization of the gene encoding an 18-kilodalton small heat shock protein associated with the membrane of Leuconostoc oenos. *Appl. Environ. Microbiol.*, 63:609–14, 1997.

[120] J. Guzzo, F. Delmas, F. Pierre, M.-P. Jobin, B. Samyn, J. Van Beeumen, J.-F. Cavin, and C. Divies. A small heat shock protein from Leuconostoc oenos induced by multiple stresses and during stationary growth phase. *Lett. Appl. Microbiol.*, 24:393–6, 1997.

[121] J. Guzzo, M-P. Jobin, F. Delmas, L-C. Fortier, D. Garmyn, R. Tourdot-Marechal, B. Lee, and C. Divies. Regulation of stress response in Oenococcus oeni as a function of environmental changes and growth phase. *Int. J. Food Microbiol.*, 55:27–31, 2000.

[122] Y. Augagneur, J.-F. Ritt, D. M. Linares, F. Remize, R. Tourdot-Marechal, D. Garmyn, and J. Guzzo. Dual effect of organic acids as a function of external pH in Oenococcus oeni. *Arch. Microbiol.*, 188:147–157, 2007.

[123] H. Nakamoto and L. Vigh. The small heat shock proteins and their clients. *Cell. Mol. Life Sci.*, 64:294–306, 2007.

[124] W. W. de Jong, G. J. Caspers, and J. A.M. Leunissen. Genealogy of the alpha-crystallin-small heat-shock protein superfamily. *Int. J. Biol. Macromol.*, 22:151–62, 1998.

[125] R. A. Lindner, A. Kapur, M. Mariani, S. J.Titmuss, and J. A. Carver. Structural alterations of alpha-crystallin during its chaperone action. *Eur. J. Biochem.*, 258:170–83, 1998.

[126] R. A. Lindner, J. A. Carver, M. Ehrnsperger, J. Buchner, G. Esposito, J. Behlke, G. Lutsch, A. Kotlyarov, and M. Gaestel. Mouse Hsp25, a small heat shock protein. *Eur. J. Biochem.*, 267:1923–32, 2000.

[127] F. Delmas, F. Pierre, F. Coucheney, C. Divies, and J. Guzzo. Biochemical and Physiological Studies of the Small Heat Shock Protein Lo18 from the Lactic Acid Bacterium Oenococcus oeni. *J. Mol. Microbiol. Biotechnol.*, 3:601–10, 2001.

[128] J. Guzzo. Biotechnical applications of small heat shock proteins from bacteria. *International Journal of Biochemistry and Cell Biology*, 44:1698–705, 2012.

[129] M. Maitre, S. Weidmann, A. Rieu, D. Fenel, G. Schoehn, C. Ebel, J. Coves, and J. Guzzo. The oligomer plasticity of the small heat-shock protein Lo18 from Oenococcus oeni influences its role in both membrane stabilization and protein protection. *Biochem. J.*, 444:97–104, 2012.

[130] M. Maitre, S. Weidmann, F. Dubois-Brissonnet, V. David, J. Coves, and J. Guzzo. Adaptation of the Wine Bacterium Oenococcus oeni to Ethanol Stress: Role of the Small Heat Shock Protein Lo18 in Membrane Integrity. *Appl. Environ. Microbiol.*, 80:2973–80, 2014.

[131] Q. Yu and G. Golden. Probing the Protein Orientation on Charged Self-Assembled Monolayers on Gold Nanohole Arrays by SERS. *Langmuir*, 23:8659–62, 2007.

[132] A. J. Hall, M. Rosenthal, N. Gregoricus, S. A. Greene, J. Ferguson, O. L. Henao, J. Vinje, B. A. Lopman, U. D. Parashar, and M.-A. Widdowson. Incidence of Acute Gastroenteritis and Role of Norovirus, Georgia, USA, 2004–2005. *Emerg Infect Dis*, 17:1381–8, 2011.

[133] E. Scallan, P. M. Griffin, F. J. Angulo, R. V. Tauxe, and R. M. Hoekstra. Foodborne Illness Acquired in the United State Unspecified Agents. *Emerg Infect Dis.*, 17:16–22, 2011.

[134] M. M. Patel, A. J. Hall, J. Vinje, and U. D. Parashar. Noroviruses: a comprehensive review. *J. Clin. Virol.*, 44:1–8, 2009.

[135] G. Belliot, A. Lavaux, D. Souihel, D. Agnello, and P. Pothier. Use of murine norovirus as a surrogate to evaluate resistance of human norovirus to disinfectants. *Appl. Environ. Microbiol.*, 74:3315–8, 2008.

[136] D. P. Zheng, T. Ando, R. L. Fankhauser, R. S. Beard, and R. I. Glass. Norovirus classification and proposed strain nomenclature. *Virology*, 346:312–23, 2006.

[137] C. E. Wobus, S. M. Karst, L. B. Thackray, K. Chang, S. V. Sosnovtsev, G. Belliot, A. Krug, J. M. Mackenzie, K. Y. Green, and H. W. Virgin IV. Replication of Norovirus in Cell Culture Reveals a Tropism for Dendritic Cells and Macrophages. *PLoS Biol*, 2:e432, 2004.

[138] C. E. Wobus, L. B. Thackray, and H. W. Virgin 4th. Murine Norovirus: a Model System To Study Norovirus Biology and Pathogenesis. *Journal of Virology*, 80:5104–12, 2006.

[139] A. Girod, C. E. Wobus, Z. Zadori, M. Ried, K. Leike, P. Tijssen, Jurgen A. Kleinschmidt, and M. Hallek. The VP1 capsid protein of adeno-associated virus type 2 is carrying a phospholipase A2 domain required for virus infectivity. *J. Gen. Virology*, 83:973–8, 2002.

[140] B. V. V. Prasad, M. E. Hardy, T. Dokland, J. Bella, M. G. Rossmann, and M. K. Estes. X-ray crystallographic structure of the Norwalk virus capsid. *Nature*, 286:287–90, 1999.

[141] S. Taube, J. R. Rubin, U. Katpally, T. J. Smith, A. Kendall, J. A. Stuckey, and C. E. Wobus. High-Resolution X-Ray structure and functional analysis of the murine norovirus 1 capsid protein protruding domain. *Journal of Virology*, 84:5695–705, 2010.

[142] R. Chen, J. D. Neill, J. S. Noel, A. M. Hutson, R. I. Glass, M. K. Estes, and B. V. V. Prasad. Inter- and intragenus structural variations in Caliciviruses and their functional implications. *Journal of Virology*, 78:6469–79, 2004.

[143] S. M. Karst, C. E. Wobus, M. Lay, J. Davidson, and H. W. Virgin 4th. STAT1-Dependent Innate Immunity to a Norwalk-Like Virus. *Science*, 299:1575–8, 2003.

[144] Z. V. Leonenko, E. Finot, H. Ma, T. E. S. Dahms, and D. T. Cramb. Investigation of temperature-induced phase transitions in DOPC and DPPC phospholipid bilayers using temperature-controlled Scanning Force Microscopy. *Biophys. J.*, 86:3783–93, 2004.

[145] K. Simons and E. Ikonen. Functional rafts in cell membranes. *Nature*, 387:569–72, 1997.

[146] R. E. Brown. Sphingolipid organization in biomembranes: what physical studies of model membranes reveal. *J. Cell. Sci.*, 111:1–9, 1998.

[147] S. Chatterjee and S. Mayor. The GPI-anchor and protein sorting. *Cell. Mol. Life Sci.*, 58:1969–87, 2001.

[148] K. Simons and D. Toomre. Lipid rafts and signal transduction. *Nat Rev Mol Cell Biol*, 1:31–9, 2000.

[149] E. B. Babiychuk, K. Monastyrskaya, F. C. Burkhard, S. Wray, and A. Draeger. Modulating signaling events in smooth muscle: cleavage of annexin 2 avolishes its binding to lipid rafts. *FASEB J.*, 16:1177–84, 2002.

[150] L. Rajendran, M. Masilamani, S. Solomon, R. Tikkanen, C. A. Stuermer, H. Plattner, and H. Illges. Asymmetric organization of flotillins/reggies in preassembled platforms confers inherent polarity to hematopoietic cells. *Proc. Natl. Acad. Sci. USA*, 100:8241–6, 2003.

[151] T. V. Kurzchalia and R. G. Parton. Membrane microdomains and caveaolae. *Curr. Opin. Cell Biol.*, 11:424–31, 1999.

[152] G. Palade. Fine structure of blood capillaries. *J. Appl. Phys.*, 24:1424, 1953.

[153] E. Yamada. The fine structure of the gall bladder epithelium of the mouse. *J. Biophys. Biochem. Cytol.*, 1:445–58, 1955.

[154] A. M. Fra, E. Williamson, K. Simons, and R. G. Parton. De novo formation of caveolae in lymphocytes by expression of VIP21-caveolin. *Proc. Natl. Acad. Sci. USA*, 92:8655–9, 1995.

[155] S. Sonnino and A. Prinetti. Sphingolipids and membrane environments for caveolin. *FEBS Lett.*, 583:597–606, 2009.

[156] M. C. Giocondi, V. Vie, E. Lesniewska, J. P. Goudonnet, and C. Le Grimellec. In situ imaging of Detergent-Resistant Membranes by Atomic Force Microscopy. *J. Struct. Biol.*, 131:38–43, 2000.

[157] W. Zhang, P. R. Chipman, J. Corver, P. R. Johnson, Y. Zhang, S. Mukhopadhyay, T. S. Baker, J. H. Strauss, M. G. Rossmann, and R. J. Kuhn. Visualization of membrane protein domains by cryo-electron microscopy of dengue virus. *Nature Structural Biology*, 10:907–12, 2003.

[158] J. F. Conway, N. Cheng, A. Zlotnick, P. T. Wingfield, S. J. Stahl, and A. C. Steven. Visualization of a 4-helix bundle in the hepatitis B virus capsid by cryo-electron microscopy. *Nature*, 386:91–4, 1997.

[159] S.N. Pleskova, E.N. Aybeke, E.N. Pudovkina, E. Bourillot, and E. Lesniewska. The study of monocytes and their submembrane structures by atomic force microscopy. *J. Bio. Phys. Chem.*, 12:168–73, 2012.

[160] L. Picas, A. Carretero-Genevrier, M. T. Montero, J.L. Vaquez-Ibar, B. Seantier, P. E. Milhiet, and J. Hernandez-Borrell. Preferential insertion of lactose permease in phospholipid domains: AFM observations. *Biochim. Biophys. Acta*, 1798:1014–9, 2010.

[161] S. Feng, R. Chena, J. Lina, J. Panb, G. Chena, Y. Li, M. Chengd, Z. Huanga, J. Chena, and H. Zeng. Nasopharyngeal cancer detection based on blood plasma surface-enhanced Raman spectroscopy and multivariate analysis. *Biosens. Bioelectron.*, 25:2414–9, 2010.

[162] D. Manno, E. Filippo, R. Fiore, A. Serra, E. Urso, A. Rizzello, and M. Maffia. Monitoring prion protein expression in complex biological samples by SERS for diagnostic applications. *Nanotechnology*, 21:165502, 2010.

[163] T.-T. Liu, Y.-H. Lin, C.-S. Hung, T.-J. Liu, Y. Chen, Y.-C. Huang, T.-H. Tsai, H.-H. Wang, D.-W. Wang, J.-K. Wang, Y.-L. Wang, and C.-H. Lin. A High Speed Detection Platform Based on Surface-Enhanced Raman Scattering for Monitoring Antibiotic-Induced Chemical Changes in Bacteria Cell Wall. *PLoS One*, 4:e5470, 2009.

[164] U. Katpally, N. R. Voss, T. Cavazza, S. Taube, J. R. Rubin, V. L. Young, J. Stuckey, V. K. Ward, H. W. Virgin, C. E. Wobus, and T. J. Smith. High-resolution cryo-electron microscopy structures of MNV-1 and RHDV reveals marked flexibility in the receptor binding domains. *J. Virol.*, 84:5836–41, 2010.

[165] C. Yuan, J. Furlong, P. Burgos, and L. J. Johnston. The size of lipid rafts: an Atomic Force Microscopy study of ganglioside GM1 domains in sphingomyelin/DOPC/cholesterol membranes. *Biophys. J.*, 82:2526–35, 2002.

[166] L. J. Johnston. Nanoscale imaging of domains in supported lipid membranes. *Langmuir*, 23:5886–95, 2007.

[167] C. Krafft, L. Neudert, T. Simat, and R. Salzer. Near infrared Raman spectra of human brain lipids. *Spectrochimica Acta Part A: Molecular and Biomolecular Spectroscopy*, 61:1529–35, 2005.

[168] H. Wu, J. W. Volponi, A. E. Oliver, A. N. Parikh, B. A. Simmons, and S. Singh. In vivo lipidomics using single-cell Raman spectroscopy. *Proc. Natl. Acad. Sci.*, 108:3809–14, 2011.

[169] M. A. Ochsenkuhn, P. R. T Jess, H. Stoquert, K. Dholakia, and C. J. Campbell. Nanoshells for Surface-Enhanced Raman Spectroscopy in Eukaryotic Cells: Cellular Response and Sensor Development. *ACS Nano*, 3:3613–21, 2009.

[170] R. M. Jarvis, N. Law, I. T. Shadi, P. O'Brien, J. R. Lloyd, and R. Goodacre. Surface-Enhanced Raman Scattering from Intracellular and Extracellular Bacterial Locations. *Anal. Chem.*, 80:6741–6, 2008.

[171] K. A. Willets. Surface-enhanced Raman scattering (SERS) for probing internal cellular structure and dynamics. *Anal. Bioanal.Chem.*, 394:85–94, 2009.

[172] H. Chu, Y. Huang, and Y. Zhao. Silver nanorod arrays as a surface-enhanced Raman scattering substrate for foodborne pathogenic bacteria detection. *Appl. Spectrosc.*, 62:922–31, 2008.

[173] C. Fan, Z. Hu, L. K. Riley, G. A. Purdy, A. Mustapha, and M. Lin. Detecting Food- and Waterborne Viruses by Surface-Enhanced Raman Spectroscopy. *J. Food Sci.*, 75:M302–7, 2010.

[174] P. R. T. Jess, D. D. W. Smith, M. Mazilu, K. Dholakia, A. C. Riches, and C. S. Herrington. Early detection of cervical neoplasia by Raman spectroscopy. *International Journal of Cancer*, 121:2723–8, 2007.

[175] H.-W. Tang, X. B. Yang, J. Kirkham, and D. A. Smith. Probing Intrinsic and Extrinsic Components in Single Osteosarcoma Cells by Near-Infrared Surface-Enhanced Raman Scattering. *Anal. Chem.*, 79:3646–53, 2007.

[176] N. Stone, C. Kendall, N. Shepherd, P. Crow, and H. Barr. Near-infrared Raman spectroscopy for the classification of epithelial pre-cancers and cancers. *J. Raman Spectrosc.*, 33:564–73, 2002.

[177] M. D. Hodges, J. G. Kelly, A. J. Bentley, S. Fogarty, I. I. Patel, F. L. Martin, and N. J. Fullwood. Combining Immunolabeling and Surface-Enhanced Raman Spectroscopy on Cell Membranes. *ACS Nano*, 5:9535–41, 2011.

[178] J.Wessel. Surface-enhanced optical microscopy. *J. Opt. Soc. Am. B*, 2:1538–41, 1985.

[179] E. A. Todd and M. D. Morris. Micron Surface-Enhanced Raman Spectroscopy of Intact Biological Organisms and Model Systems. *Appl. Spectrosc.*, 48:545–8, 1994.

[180] R. M. Stockle, Y. D. Suh, V. Deckert, and R. Zenobi. Nanoscale chemical analysis by tip-enhanced Raman spectroscopy. *Chem. Phys. Lett.*, 318:131–6, 2000.

[181] M. Micic, N. Klymyshyn, Y. D. Suh, and H. P. Lu. Finite Element Method Simulation of the Field Distribution for AFM Tip-Enhanced Surface-Enhanced Raman Scanning Microscopy. *J. Phys. Chem. B*, 107:1574–84, 2003.

[182] Dana Cialla, T. Deckert-Gaudig, C. Budich, M. Laue, R. Moller, D. Naumann, V. Deckert, and J. Poppa. Raman to the limit: tip-enhanced Raman spectroscopic investigations of a single tobacco mosaic virus. *J. Raman Spectrosc.*, 40:240–3, 2009.

[183] N. Hayazawa, Y. Saito, and S. Kawata S. Detection and characterization of longitudinal field for tip-enhanced Raman spectroscopy. *Appl. Phys. Lett.*, 85:6239–41, 2004.

[184] S. Quabis, R. Dorn, and G. Leuchs. Generation of a radially polarized doughnut mode of high quality . *Applied Physics B-Lasers and Optics*, 200581:597–600, 2005.

[185] H. Li, Q. Zhang, C. C. R. Yap, B. K. Tay, T. H. T. Edwin, A. Olivier, and D. Baillargeat. From Bulk to Monolayer MoS2: Evolution of Raman Scattering. *Adv. Funct. Mater.*, 22:1385–90, 2012.

[186] P. A. Bertrand. Surface-phonon dispersion of MoS_2. *Phys. Rev. B*, 44:5745–9, 1991.

[187] C. Lee, H. Yan, L. E. Brus, T. F. Heinz., J. Hone, and S. Ryu. Anomalous Lattice Vibrations of Single- and Few-Layer MoS2. *ACS Nano*, 4:2695–2700, 2010.

[188] S. Piscanec, A.C. Ferrari, M. Cantoro, S. Hofmann, J.A. Zapien, Y. Lifshitz, S.T. Lee, and J. Robertson. Raman Spectrum of silicon nanowires. *Mater. Sci. Eng., C*, 23:931–4, 2003.

[189] B. Pettinger, K. F. Domke, D. Zhang, G. Picardi, and R. Schuster. Tip-enhanced Raman scattering: Influence of the tip-surface geometry on optical resonance and enhancement . *Surface Science*, 603:1335–41, 2009.

[190] Z. D. Schultz, S. J. Stranick, and I. W. Levin. Advantages and Artifacts of Higher Order Modes in Nanoparticle-Enhanced Backscattering Raman Imaging . *Analytical Chemistry*, 81:9657–63, 2009.

Publications

Publications

1. E. N. Aybeke, Y. Lacroute, C. Elie-Caille, A. Bouhelier, E. Bourillot and E. Lesniewska. Homogeneous large-scale crystalline nanoparticle-covered substrate with high SERS performance. *Nanotechnology*, 26: 245302, 2015.

2. R. Zeggari, J.-F. Manceau, E. N. Aybeke, R. Yahiaoui, E. Lesniewska and W. Boireau. Design and fabrication of an acoustic micromixer for biological media activation. *Procedia Engineering*, 87:935–8, 2014.

3. S. N. Pleskova, E. N. Aybeke, E. N. Pudovkina, E. Bourillot and E. Lesniewska. The study of monocytes and their submembrane structures by atomic force microscopy. *Journal of Biological Physics and Chemistry*, 12(4):168–173, 2012.

4. E. N. Aybeke, G. Belliot, S. Ewing, M. Estienney, Y. Lacroute, P. Pothier, E. Bourillot and E. Lesniewska. AFM and SERS analysis of Murine Norovirus infection: Implication of lipid rafts. *In preparation.*

Conferences

Oral Presentations

1. E. N. Aybeke, Y. Lacroute, G. Belliot, M. Estienney, S. Ewing-Lemaire, P. Pothier, E. Bourillot and E. Lesniewska. Investigation of gastroenteritis disease on mouse leukaemic monocyte macrophage (RAW) cells by FastScan and SERS. Reims, France, 2014. Bruker user meeting.

2. E. N. Aybeke, G. Belliot, S. Ewing-Lemaire, M. Estienney, P. Pothier, Y. Lacroute, E. Bourillot and E. Lesniewska. AFM and SERS studies of human noroviruses infections. Dijon, France, June 30th - July 3th 2013. 15th International Scanning Probe Microscopy Conference.

3. E. N. Aybeke, Y. Lacroute, E. Bourillot, S. Ewing-Lemaire, M. Estienney, P. Pothier, G. Belliot and E. Lesniewska. Study of noroviruses infection by AFM and SERS. Dijon, France, 2013. Journee de l'ecole doctorale Carnot-Pasteur.

4. E. N. Aybeke G. Belliot, Y. Lacroute, S. Ewing-Lemaire, M. Estienney, Pierre Pothier, E. Bourillot and E. Lesniewska. Investigation of virus and living cell interactions. Lyon, France, 2013. Bruker user meeting.

5. E. N. Aybeke, D. Carriou, M. Malgorzata, R. Filomenko, S. Pleskova, E. Bourillot and E. Lesniewska. Investigation of protein-DNA-surface interaction by High-Speed Atomic Force Microscopy. Paris, France, July 2012. International Conference on Nanoscience + Technology-ICNT.

6. E. N. Aybeke, S. Pleskova, D. Carriou, E. Bourillot and E. Lesniewska. Protein analyses by LSPR, SERS, AFM et HS-AFM. Besancon, France, April 2012. CLIPP Proteomic platform meeting.

Poster Presentation

1. E. N. Aybeke, D. Carriou, Y. Lacroute, E. Bourillot, P. M. Adam, C. Elie-Caille and E. Lesniewska. SERS and HS-AFM: useful tools for biological investigations. Besancon, France, June 2012. Journee de l'ecole doctorale Carnot-Pasteur.

Contributions

1. R. Zeggari, J.-F. Manceau, **E. N. Aybeke**, R. Yahiaoui, E. Lesniewska and W. Boireau. Design and fabrication of acoustic micromixer for biological media activation. Brescia, Italy, September 7th - 10th 2014. Eurosensors 2014.

2. E. Lesniewska, D. Carriou, **E. N. Aybeke**, S. Weidmann, S. J. Guzzo and E. Bourillot. High-Speed Atomic Force Microscopy on proteins. Lyon, France, 2013. Bruker user meeting.

3. G. Belliot, **E. N. Aybeke**, S. Ewing-Lemaire, M. Estienney, E. Noirot, E. Bourillot, E. Lesniewska and P. Pothier. Role of lipid rafts during norovirus attachment. Beijing, China, October 2013. 5th International conferences on Caliciviruses.

4. E. Lesniewska, **E. N. Aybeke**, P. Vitry, E. Bourillot, S. Weidmann and S. J. Guzzo. Investigation of protein-membrane interaction by High-Speed Atomic Force Microscopy. Paris, France, May 2013. J. Sci. INSERM AFM Bio Workshop.

5. S. N. Pleskova, **E. N. Aybeke**, R. Filomenko, T. Salvary, E. Bourillot and E. Lesniewska. The differences in the morphology of the planar rafts and caveolae investigated by atomic force microscopy. Moscow, Russia, 2012. Proceedings of the Sixth International Conference "Recent advances of the bionanoscopy".

6. S. N. Pleskova, E. N. Pudovkina, **E. N. Aybeke** et al. Investigation of the living cells by Atomic Force Microscopy. Tbilisi, Georgia, 2012. ISTC International Scientific Seminar "Neuroplasticity: Nervous substrate for health and disease. New approaches for researches".

7. E. Lesniewska, D. Carriou, **E. N. Aybeke**, S. Weidmann, S. J. Guzzo and E. Bourillot. Protein-membrane interaction investigated by High-Speed Atomic Force Microscopy. Kanazawa, Japan, November 2012. 3rd Kanazawa Bio-AFM Workshop.

8. E. Lesniewska, **E. N. Aybeke**, D. Carriou, M. Malgorzata, R. Filomenko, S. Pleskova and E. Bourillot. Protein-DNA-surface interaction studied by High-Speed Atomic Force Microscopy. Nancy, France, Mars 2012. Nanosciences & Nanotechnologies "Les dernieres avancees en AFM".